EFFECT OF OXYGEN ON CREEP CRACK GROWTH IN NICKEL-BASE SUPERALLOYS

by

Kenneth Rees Bain

B.M.E., General Motors Institute
(1980)

S.M., Massachusetts Institute of Technology
(1982)

SUBMITTED TO THE DEPARTMENT OF
MATERIALS SCIENCE AND ENGINEERING
IN PARTIAL FULFILLMENT OF THE
REQUIREMENTS OF THE
DEGREE OF

DOCTORATE IN PHILOSOPHY

at the

MASSACHUSETTS INSTITUTE OF TECHNOLOGY

September 1983

Signature of Author: ______________________________
Department of Materials Science and Engineering
August 5,1983

Certified by: ______________________________
Regis M. Pelloux
Thesis Supervisor

Accepted by: ______________________________
Bernhardt J. Wuensch
Chairman, Departmental Graduate Committee

EFFECT OF OXYGEN ON CREEP CRACK GROWTH IN NICKEL-BASE SUPERALLOYS

by
KENNETH REES BAIN

Submitted to the Department of Materials Science and Engineering on August 5, 1983 in partial fulfillment of the requirements for the Degree of Doctorate in Philosophy.

ABSTRACT

The creep crack growth rates (CCGR) of four PM/HIP nickel-base superalloys are measured in the range of CCGR from 10^{-9} m/s to 10^{-5} m/s and a range of stress intensity, K, from 10 to 120 MPa$\sqrt{m}$ at 704°C in air and in 99.999% pure argon. The alloys tested are Low Carbon Astroloy, Merl-76, Low Carbon IN-100, and Rene-95 (60 and 120 mesh size powders). Crack length was measured on single edge notched specimens using the D.C. potential drop technique. Crack growth rates were observed to accelerate up to 1000 times in an air environment over the CCGR measured in 99.999% pure argon.

The fracture path was totally intergranular in all the CCG tests. The fracture path in argon follows grain boundaries which coincide with prior powder boundaries (PPB). There was no preference for PPB grain boundary cracking in CCGR tests in air.

The CCGR behavior of the Ni-base alloys tested was shown to correlate with the stress intensity factor, K. The CCGR versus K curves exhibit three stages of behavior which are associated respectively with an initial transient in damage accumulation ahead of the crack, power law dependent CCGR on K and fast fracture at K_{IC}. The measured CCGR for an alloy is shown to be significantly affected by changes in test procedure, specimen design, and initial K.

A comparison of the notched stress rupture results gives a qualitative measure of the CCGR behavior observed for the nickel-base alloys.

Tensile, creep, and creep rupture tests at 704°C for 4 alloys were performed to obtain the constitutive equations. These relationships along with the microstructure were used to model the CCGR behavior of the alloys based on the accumulation of damage ahead of the crack tip. The computer model predicts the effect of microstructure, mechanical properties, and load history on creep crack growth rates.

Thesis Supervisor: Dr. Regis M. Pelloux
Title: Professor of Materials Engineering

TABLE OF CONTENTS

TABLE OF CONTENTS (cont'd)

CHAPTER PAGE

TABLE OF CONTENTS (cont'd)

LIST OF FIGURES

LIST OF TABLES

ACKNOWLEDGEMENTS

The author gratefully acknowledges the support of the following people and institutions. Their encouragement and assistance greatly contributed to the completion of this thesis.

Professor Regis Pelloux, the author's thesis advisor whose guidance, encouragement, and assistance throughout the author's graduate studies were invaluable.

Professor Andre Pineau whose many discussions and critiques on modelling of creep crack growth were very helpful.

Professor F.A. McClintock and Professor R. Ballinger for their reviews and comments of the final thesis.

Mr. Lenny Sudenfield for his help in operating and later teaching the operation of the scanning electron microscope at M.I.T.

The author would like to thank Philippe Bensussan and Bill Moshier, graduate students at M.I.T., for their help and discussions on occasions too numerous to count. The author would also like to acknowledge all the members of the creep and fatique research group for their interesting discussions and assistance throughout the author's graduate career.

My wife, Amy, who typed this document and without whose love and constant support this research would have been impossible.

The author would like to acknowledge the financial support given by the Air Force Office of Scientific Research and the Cabot Corporation in the form of a Cabot Fellowship.

The author would also like to acknowledge the Center for Material Science and Engineering for support from a NSF-MRL grant, and the AT-1, High Temperature Fracture, group for their many interesting discussions.

1. INTRODUCTION

Creep crack growth is a process in which a single crack advances intergranularly in a material under a constant tensile stress at temperatures where at least local creep deformation is possible (T>.4 Tm; melting point). In an inert test environment the micromechanisms of creep crack growth consist of nucleation, growth, and coalescence of grain boundary cavities.

The recent interests in creep crack growth and other forms of high temperature mechanisms for crack advance are the result of the desire to incorporate fracture mechanics concepts into advanced design criteria. The concept of retirement-for-cause as a method for extending the useful life of many high temperature components is but one example of these advanced criteria (1). Creep crack growth is an area of concern in nickel-base superalloys used in modern gas turbines hot section components and stainless steel in nuclear and conventional power plants.

Current design criteria for gas turbine engines are based on bulk creep deformation and crack initiation. The components are removed from service when there is a statistical chance that one part in 1000 has developed a 1/32 inch crack. This conservative life limit results in the retirement of 999 out of 1000 components, many of which may have up to 10 times more useful life. The cost of replacing these components may reach $100 million a year by

1985. The life of these critical components could be extended by periodically inspecting the part for cracks and replacing only those parts in which cracks are found. The spacing of the inspection periods requires both an understanding of the reasonable limits of detection of a flaw and of the rate at which this flaw or crack propagates to final fracture. The accuracy required in the prediction of a creep crack propagation time is critical since failure of a component such as a turbine disk could be costly.

Creep is time-dependent deformation of a material under stress. The mechanisms of creep and creep fracture have been extensively studied (2-4). The notched stress rupture (NSR) test is a simple test designed to measure the time to rupture due to creep processes in the vicinity of a stress concentration site. Extensive NSR and smooth bar test results have indicated that the time to rupture is reduced in the presence of the high stresses at the root of a notch. The creep crack growth test can be thought of as a more severe NSR test in which the time to form the macroscopic crack is eliminated. The test environment has been shown to significantly affect the results of smooth bar and NSR tests (5), and the environment will also have an effect on the creep crack growth rate (CCGR).

Creep crack growth testing can be thought of as a severe form of notched stress rupture testing. The crack tip acts as a severe stress concentration site which produces locally large stresses, which may relax with time due to creep deformation and fracture. The crack front advances as a result of creep damage which is due to the time-dependent crack tip stresses. Crack tip plasticity, and environmental embrittlement ahead of the crack tip play an important role in controlling CCGR.

This thesis includes first a brief review of the current literature on the metallurgy of nickel-base alloys. Then the literature on environmental embrittlement of Ni-base alloys and creep crack growth is reviewed. The literature review is followed by a detailed description of mechanical test procedures, materials, and test results. Finally, a computer model of creep crack growth is presented, and a discussion of the critical results is given.

2. LITERATURE REVIEW

2.1. Metallurgy of Ni-Base Alloys

Nickel-base superalloys are the material used in almost every modern gas turbine disk and blade. This is due to the outstanding tensile properties, creep-rupture strength, low-cycle fatigue strength, and corrosion resistance of these alloys at the high operating temperatures (i.e. > $600^{o}C$) which are common in modern gas turbine engines. Typical modern turbine engines are designed for 5000 to 100,000 hr. lives which therefore require long time alloy stability. Turbine operating conditions are pushed to the maximum capability of the alloy in the interest of minimum weight and maximum operating efficiency. All these requirements are generally fulfilled by Ni-base superalloys. The following sections detail the chemistry, microstructure, strengthening mechanisms and heat treatment of nickel-base superalloys.

2.1.1. Chemistry of Ni-Base Alloys

The chemistry of nickel-base superalloys is complex with at least 12 carefully controlled alloying elements. In general these alloys contain 10-20 percent chromium, up to 8 percent aluminum and titanium, and small amounts of boron, zirconium, and carbon. Other elements are added to enhance specific properties, but usually at the expense of some other properties.

The alloying elements can be divided into three classes which are:

1. Elements which prefer to form the face-centered cubic (FCC) austenite (gamma,γ) matrix (i.e. nickel, iron, chromium, cobalt, molybdenum, tungsten, and vanadium)

2. Elements which form the gamma prime phase (γ ') (i.e., aluminum, titanium, columbium, and tantalum)

3. Elements which segregate to the grain boundary (i.e., magnesium, boron, carbon, zirconium, and undesirable impurities).

Table 2.1. gives chemical compositions for several nickel-base superalloys currently being used in modern gas turbine applications (9).

The most common alloying additions in nickel-base alloys and the area of their greatest influence in the alloy is shown in Figure 2.1. (6).

The microstructure consists mainly of γ ' precipitates and large MC carbides embedded in the austenite matrix (gamma, γ). γ ' precipitates are also found at the grain boundaries along with $M_{23}C_6$ carbides. The matrix consists of a solid solution of nickel with cobalt, chromium, molybdenum, and tungsten. This combination of phases allows the utilization of the alloys at up to .8 T_m (melting point)

TABLE 2.1.

CHEMICAL COMPOSITION OF SELECTED NICKEL-BASE SUPERALLOYS (w/o)

(ref. 9)

	Ni	Cr	Co	Mo	W	Cb	Al	Ti	Fe	C	B	Zr	other
IN 718	52.5	19.0	-	3.0	-	5.1	0.5	0.9	18.5	.040	-	-	
RENE 95	61.0	14.0	8.0	3.5	3.5	3.5	3.5	2.5	-	.150	.010	.05	
MERL 76	54.6	12.3	17.9	3.3	-	1.7	5.0	4.3	-	.025	.018	.06	(H_f .74)
IN 100	60.5	10.0	15.0	3.0	-	-	5.5	4.7	-	.180	.014	.06	(V 1.0)
WASPALOY	58.0	19.5	13.5	4.3	-	-	1.3	3.0	-	.080	.006	.06	
NIMONIC 115	60.0	14.3	13.2	3.3	-	-	4.9	3.7	-	.015	.160	.04	
ASTROLOY	55.0	15.0	17.0	5.3	-	-	4.0	3.5	-	.060	.030	-	
X-750	73.0	15.5	-	-	-	1.0	0.7	2.5	7.0	.040	-	-	

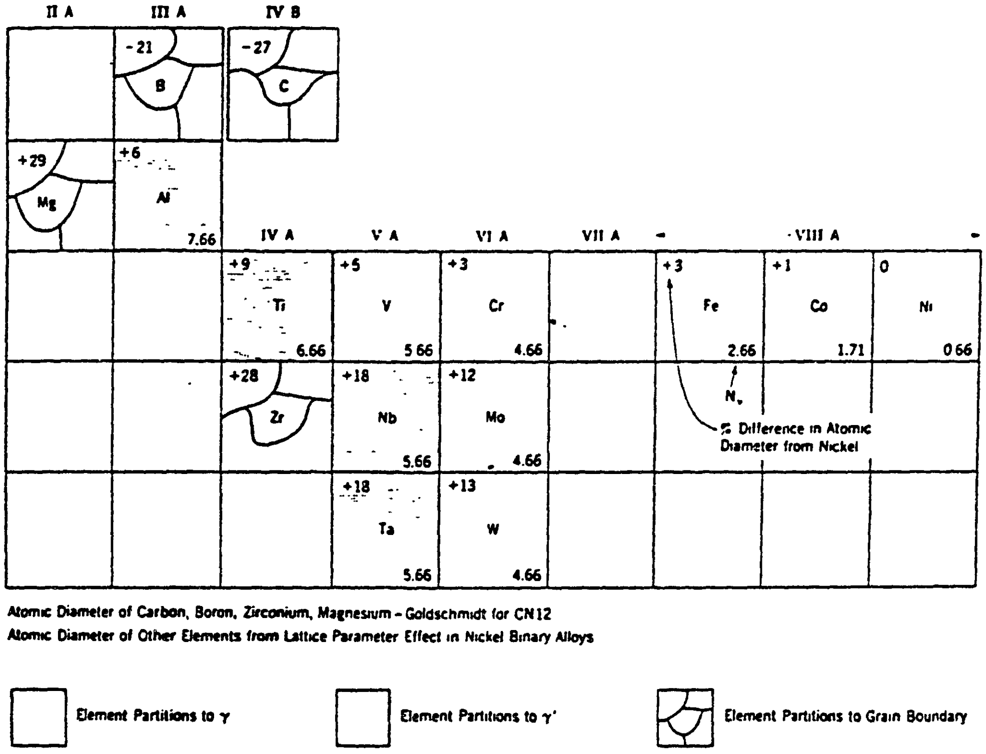

FIGURE 2.1) Periodic table of alloying elements in Nickel-Base Superalloys. (ref. 6)

for times as long as 100,000 hrs (6). Additions of chromium and aluminum form Cr_2O_3 and Al_2O_3 oxides at the surface which inhibit or slow down attack by oxygen, nitrogen, sulfur, and other aggressive atmospheric elements (7).

The main precipitate phase in the gamma matrix (γ) is gamma-prime (γ'). It is a FCC phase with the general formula A_3B, with "A" being either nickel, iron, or cobalt and "B" being either aluminum, titanium, or columbium. These precipitates were initially spherical in early alloys but advanced heat treatments result in a cube shape precipitate which enhances strengthening.

The weight percent γ' is a function of the combined atomic percent of aluminum, columbium, titanium, and tantalum. The result of γ' analyses of 15 nickel-base superalloys are summarized in Figure 2.2(8). It can be seen that additions of aluminum, titanium, columbium and tantalum will increase γ' formation. The presence of Cobalt and Vanadium will also enhances the formation of γ' from the γ matrix.

Carbides are major phases of the grain boundary microstructure in Ni-base alloys. Carbides, located at the grain boundary (usually $M_{23}C_6$) markedly inhibit grain boundary sliding. These grain boundary carbides, however, can and will serve as nucleation sites for creep cavities.

One of the major problems with Ni-base superalloys is the formation of topologically closed-packed phases (TCP). TCP phases usually have body centered tetragonal crystal

P. 21

structure. A Laves phase has the chemical formula A_2B with "A" usually being cobalt and "B" being either Mo or Ta. Sigma phase is generally of the form $(Cr,Mo)_x(Ni,Co)_y$ where x and y can vary from 1 to 7, but usually are both around unity. These phases form as hard flat plates or needles which will reduce alloy ductility (10).

The addition of Fe to the matrix enables the precipitation of γ'', eta, and delta phases which strengthen the alloy. When Columbium is present, such as in alloy IN-718, the primary strengthening phase is γ'', body centered tetragonal phase with the composition Ni_3Cb. γ'' can degenerate into the orthorhombic delta phase.

The third phase enabled by iron is called eta, which is Ni_3Ti and has a hexagonal close packed (HCP) structure. Eta is a primary strengthening phase in alloys such as A-286, IN-901, IN-706, and Pyromet 860. However, the formation of large brittle particles of either eta or delta phase will reduce rupture life and ductility.

2.1.2. Strengthening Mechanisms

Several strengthening mechanisms are usually used in Ni-Base alloys to give high short and long time strength over a wide range of operating temperatures.

Several elements are added to the γ matrix of Ni-base alloys as solid solution strengtheners. These elements harden the alloys as a result of the atomic size mismatch between the solute atoms and the nickel matrix. The most potent solid solution strengtheners are the slow diffusing elements, such as molybdenum and tungsten. For instance, Rene-95 has both Mo and W additions. The effect of solid solution strengtheners is shown in Table 2.2. The effect of 10% additions of Mo, Cr, and W on rupture strength of pure Ni is reported (12).

TABLE 2.2.
Ratio of Rupture Stress,
for a 10 atomic percent Solute Addition
versus rupture stress for pure Nickel

	Rupture Strength			
	650°C		815°C	
	1 hr	100 hr	1 hr	100 hr
σ10% Cr/σNi	3.0	2.6	2.0	2.0
σ10% Mo/σNi	3.1	3.6	2.4	2.4
σ10% W/σNi	3.2	4.6	3.0	2.7

The most important strengthening mechanism for temperatures up to 760°C is precipitation hardening. The most common and effective precipitate is γ', $(Ni,Co)_3(Al,Ti)$. This phase has a face centered cubic structure which is compatible with the FCC γ matrix and has a 0 to 1% latice mismatch. The low mismatch allows homogeneous nucleation of the γ' precipitate and long time stability. Other phases such as γ'', eta, and delta can also precipitate from the matrix and act to strengthen the alloy. The effect of the precipitates on strength depends on the size, shape, and volume fraction of the precipitate. The optimum strength comes from a mixture of coarse and fine, cubic shaped γ' precipitates (7, 13).

The third strengthening mechanism involves the formation of beneficial carbides at grain boundaries which act to inhibit grain boundary migration and hence creep. The formation of blocky MC and $M_{23}C_6$ carbides along grain boundaries lock the grain boundaries and decrease the creep rate at high temperature. The carbides can also form as M_6C, Cr_7C_3, and as a film of $M_{23}C_6$ along the grain boundary, all of which will embrittle the grain boundaries and result in premature fracture.

The above effects (and others) can be summarized in the following guidelines for alloy design and heat treatment to improve the balance struck between creep, ductility, and tensile and creep strength:

1. Solid solution strengthen γ .
2. Increase volume percent γ'.
3. Increase coherence strains for less than 0.6 Tm.
4. Decrease ripening rate for greater than 0.6 Tm.
5. Solid solution strengthen γ'.
6. Minimize formation of TCP embrittling phases such as Ni_3Nb, Laves, and σ phases.
7. Control carbides and grain boundary γ' to enhance rupture strength.
8. Careful control of heat treatment to develope microstructure.

2.1.3. Grain Boundary Morphology

Creep crack growth is a process of intergranular fracture and therefore the control of the composition and microstructure of the grain boundaries is of great interest. Several alloying elements such as boron, zirconium, magnesium,and carbon segregate to the grain boundaries in Ni-base alloys.

Addition of less than .1 weight percent of boron and zirconium have been shown to increase creep-rupture properties.(7) These additions increased lifetime by 13 times, elongation by 7 times, rupture stress by 1.9 times, and they also increased the stress exponent, N_c, for power law creep. (7, 12) Magnesium also is thought to improve the creep properties, but it is not widely used as an alloying element.

While it is known that these B and Zr elements have a beneficial effect, the mechanisms by which B and Zr act are not clearly understood. B and Zr will segregate to the grain boundaries because of their atomic sizes 21 percent undersize and 29 percent oversize, respectively. Boron and zirconium have been shown to retard grain boundary cracking in U-500, and boron alone has been shown to resist oxidation damage along grain boundaries in IN-738 (14).

Boron was observed to reduce the onset of grain boundary crack initiation upon loading in U-500, which indicates that it may be a critical element for inhibiting grain boundary fracture. When the concentration of boron is above 120 ppm, it will form M_3B_2 borides with the "M" being primarily molybdenum and chromium. These g.b. borides act as a source of boron as well as molybdenum and chromium for the grain boundary (7).

It has also been suggested that additions of boron, zirconium and magnesium retard grain-boundary diffusion. Reduced diffusion rates along grain boundaries reduce the tendency to form γ' nodules around $M_{23}C_6$ carbides in U-500. The formation of γ' nodules depletes the grain boundary region of fine γ' which results in a loss of grain boundary strength. The effect of boron and zirconium on the creep-rupture life of Udimet 500 is shown in Table 2.3. (15).

TABLE 2.3.

Creep Rupture of Udimet 500 at 870°C

Alloy	Life at σ =17.6MPa, hrs.	Creep Exponent, N_c
Base Alloy	50	2.4
+.19% Zr	140	4.0
+.009% B	400	7.0
+.009% B + .01% Zr	647	9.0

The boron and zirconium additions reduced the number of γ' nodules observed and the number of microcracks. (15)

The effect of carbon at grain boundaries in Ni-Base alloys is generally better understood. Carbon forms either MC, $M_{23}C_6$, Cr_7C_3 or M_6C carbides. $M_{23}C_6$ carbides have a marked tendency for grain boundaries, as well as M_6C and Cr_7C_3 carbides which are observed as grain boundary films. MC carbides are important for the formation of grain boundary γ' and $M_{23}C_6$ carbides through the following reaction:

$$6\,MC + \gamma = M_{23}C_6 + \gamma'$$

This reaction occurs between 760°C and 980°C.

Carbides have positive and negative effects on creep and creep crack growth. Blocky $M_{23}C_6$ and MC carbides at grain boundaries inhibit grain boundary sliding thus reducing creep rates. They also act as sites for creep cavitation and tend to increase the CCGR as observed by Law and Blackburn (16), Pelloux and Huang (17) and Saegusa et al. (18) in different wrought Ni-base alloys. Grain boundary films of Cr_7C_3 or M_6C both have a strong negative effect of embrittling the grain boundaries and reducing stress rupture strength.

2.1.4. Heat Treatment

Proper heat treatment of nickel-base superalloys is critical for the development of strength and ductility. Wrought alloys, following solutioning of γ', consist of mainly γ matrix and MC carbides. The γ' solvus temperature varies from 1040°C to 1230°C, and aging above this temperature prepares the matrix for precipitation of γ' on subsequent cooling and/or aging.

Following solutioning a series of aging treatments are given to precipitate and develop the major strengthening phases. Rupture and creep resistance is obtained by precipitating γ' in the range of 840°C to 1100°C for a 24-hour period. This is followed by an aging at approximately 760°C to complete the development of fine γ'. Good tensile strength at lower temperatures is developed by precipitating fine γ' by aging slowly at 760°C. This also minimizes the formation of carbides at grain boundaries (7). Several variations of the general heat treatments are used to develop various microstructures.

Alloys which depend on γ'' for strength, such as IN-718, usually require a longer time for precipitation at a lower temperature. The lower temperature (650°C-760°C) age is used to avoid the formation of eta phase which will reduce creep-rupture life. (11)

2.2. Environmental Embrittlement of Ni-Base Alloys

The degradation in properties of metallic materials in various environments has long been observed. Nickel-base alloys operating at temperatures above 500°C in air exhibit a marked decrease in their creep-rupture life (24), and a decrease in notched stress rupture life (16), lower fracture ductility (34), an increase in fatigue crack growth rates (19), and in creep crack growth rates (17). Embrittlement at high temperatures in air has been observed for iron-nickel alloys (21), cobalt alloys (20), and nickel-base alloys (22-24, 26, 27, 30, 33, 34). Embrittlement in air is strongest in the nickel-base alloy systems. Only a slight effect of air is observed on cobalt systems and iron-nickel systems. Air embrittlement is not observed in copper base alloys, and in aluminum alloys (36).

2.2.1. Determination of Embrittling Elements

Chaka and McMahon (33) have demonstrated that air will reduce the creep-rupture life of Udimet 700 at 925°C by a factor of 2 over the creep-rupture life in vacuum. Similar results have been observed by Shahiniam (24) and Prager and Sines (23) on several wrought and cast nickel-base alloys. Hosoi and Abe (26) indicated that small amounts of oxygen can decarburize the surface of IN-617 and reduce the creep rupture time by causing the initiation of surface cracks. All of these studies were performed on Ni-base alloys at temperatures above 750°C. Most Ni-base alloys will have lost most of their strength at these temperatures. It has been shown that a loss in tensile ductility following pre-exposure to air at 1000°C is observed for pure nickel and IN-738 when tested at temperatures between 600°C and 900°C. (30, 34) Exposure to air results in brittle intergranular fracture.

Ni-base alloys are embrittled by a variety of other gaseous elements. Fatigue crack growth rates in IN-718 and Nimonic 115, both Ni-base alloys, are increased in the presence of hydrogen gas at 650°C (35). The presence of carbon dioxide was found to embrittle alloy PE 16 and reduce creep-rupture lives at 700°C (25). Along with the above environments the presence of sulfur containing gases will decrease ductility and rupture times for nickel-base alloys (37).

Recent research on Ni-270 (99.98% Ni) has shown that oxygen is the embrittling species in air at high temperatures (34). Round specimens .10 inches in diameter were pre-exposed to a variety of atmospheres at 1000°C for 200 hours. These environments included vacuum, N_2, H_2, CO_2, H_2O, O_2, and air. The specimens were then failed in a short time tensile test at 800°C and the reduction in area was measured. The results (See Figure 2.3) indicate that oxygen

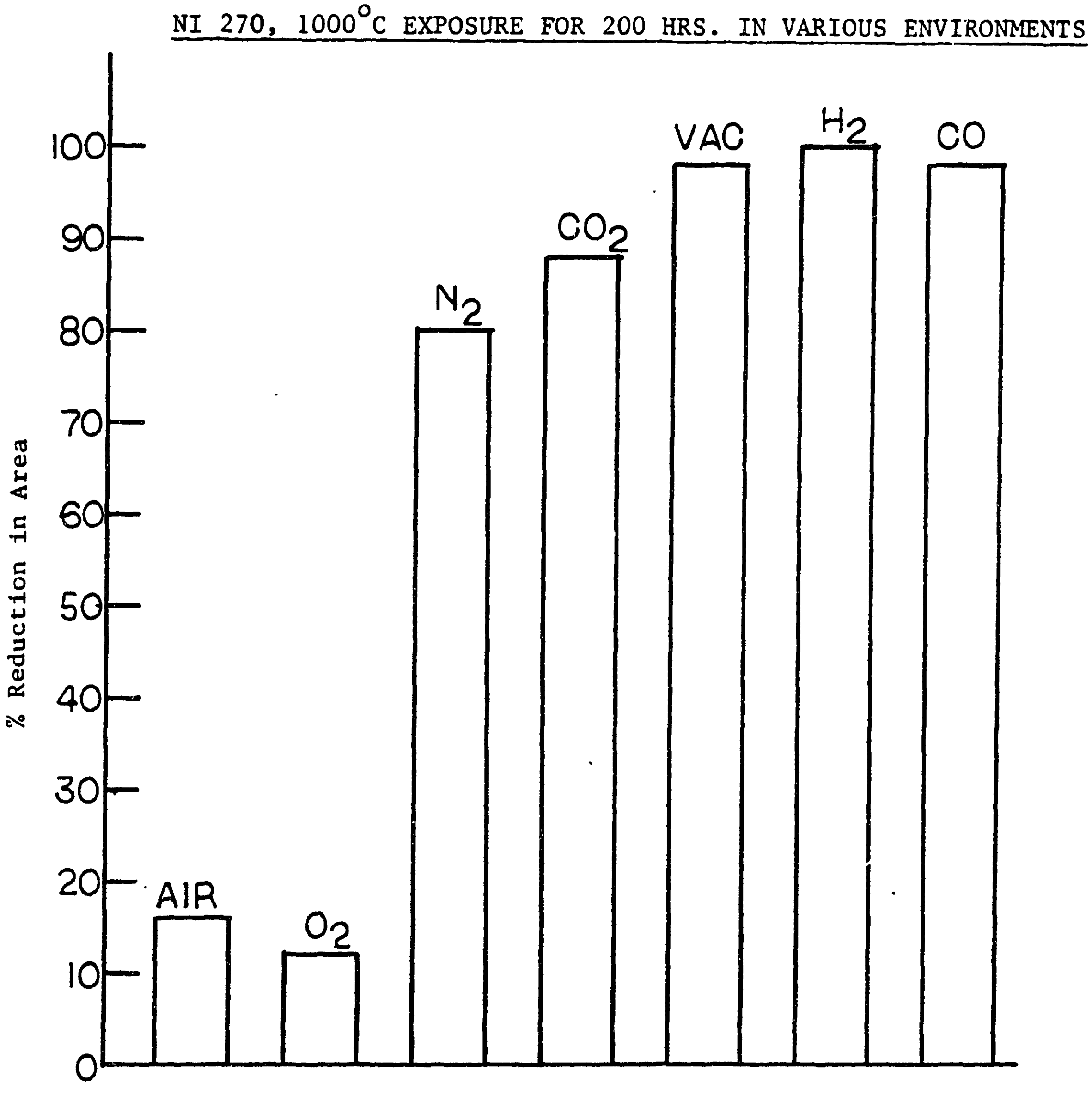

FIGURE 2.3) Percent reduction in area for NI 270 following 200 hr. exposure to various gaseous environments at 1000°C. (ref. 34)

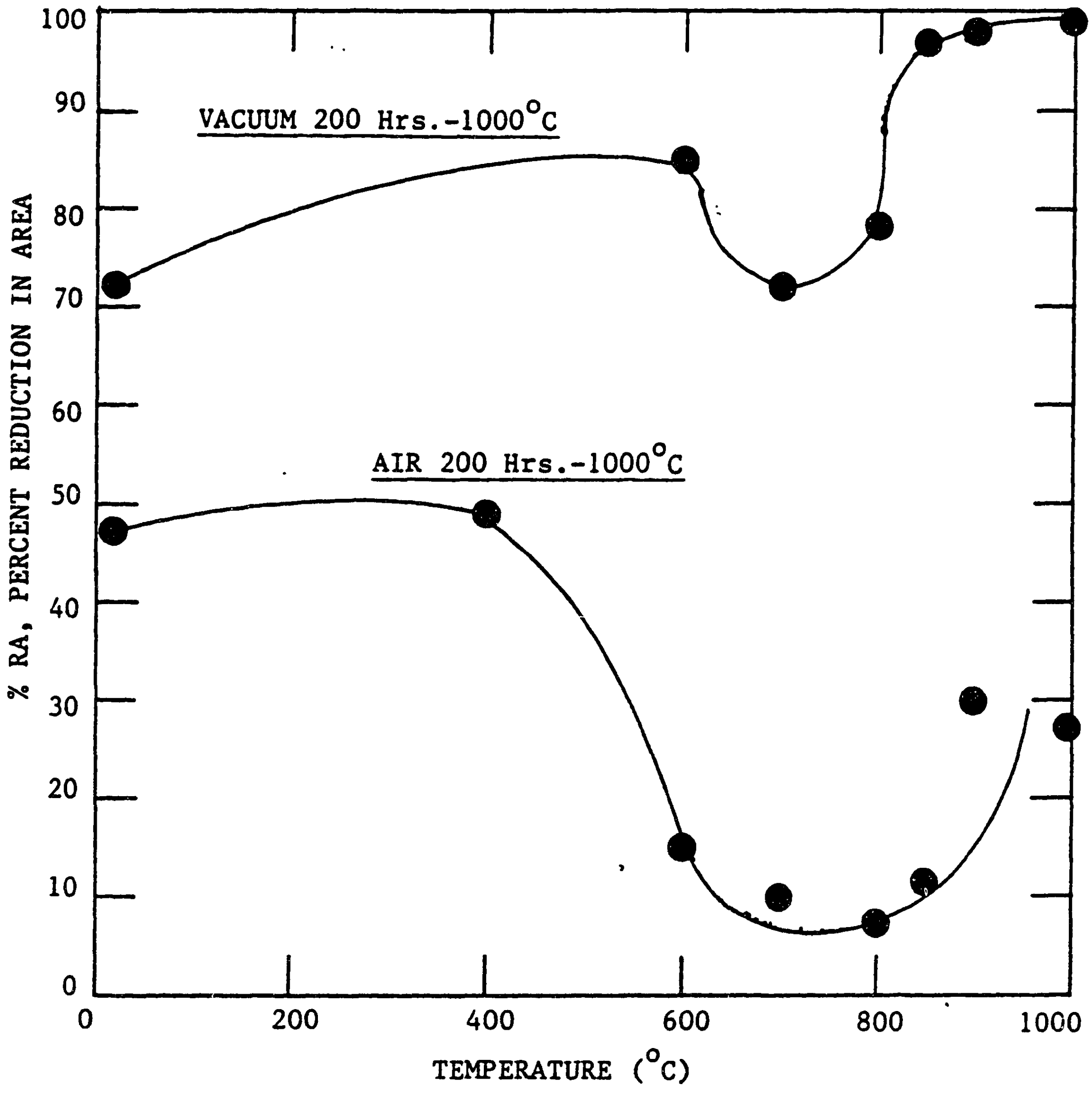

FIGURE 2.4) Reduction in area results for NI 270 versus test temperature following a 1000°C/200 hr. exposure to either air or a vacuum. (ref. 34)

is the embrittling species. Figure 2.4 shows that the embrittling effect of oxygen is only detectible over a narrow range of temperatures from 500°C to 900°C (34).

Oxygen penetration along grain boundaries in pure nickel and nickel-base alloys produces severe grain boundary embrittlement. The depth of grain boundary embrittlement of pure Ni in air from 900°C to 1100°C was measured on fracture surfaces after tensile tests (30). The results were used to generate a plot of the effective diffusivity of oxygen versus temperature^{-1} (°K) of oxygen exposure. The effective diffusivity of oxygen along the grain boundaries was calculated as $D=X^2/t$. (X is the depth of intergranular fracture, and t is the exposure time) (Figure 2.5). The plot of D versus $1/T$ gives an activation energy of 64 Kcal/gm atom and values of diffusivity which range from 10^{-10} cm^2/s to 10^{-9} cm^2/s. Extrapolation of these results to 704°C(977K) indicate an oxygen diffusivity along the grain boundaries of approximately 10^{-14}cm^2/s.

The results reported by many have demonstrated that gaseous oxygen is a severely embrittling element in both pure nickel and nickel-base alloys. This embrittlement is most severe along grain boundaries, which indicates that oxygen embrittlement will be an important factor in creep crack growth at the temperatures of interest in this study.

2.2.2. Theories of Environmental Embrittlement

While the embrittlement of nickel-base alloys by oxygen has been observed, the mechanism by which oxygen causes

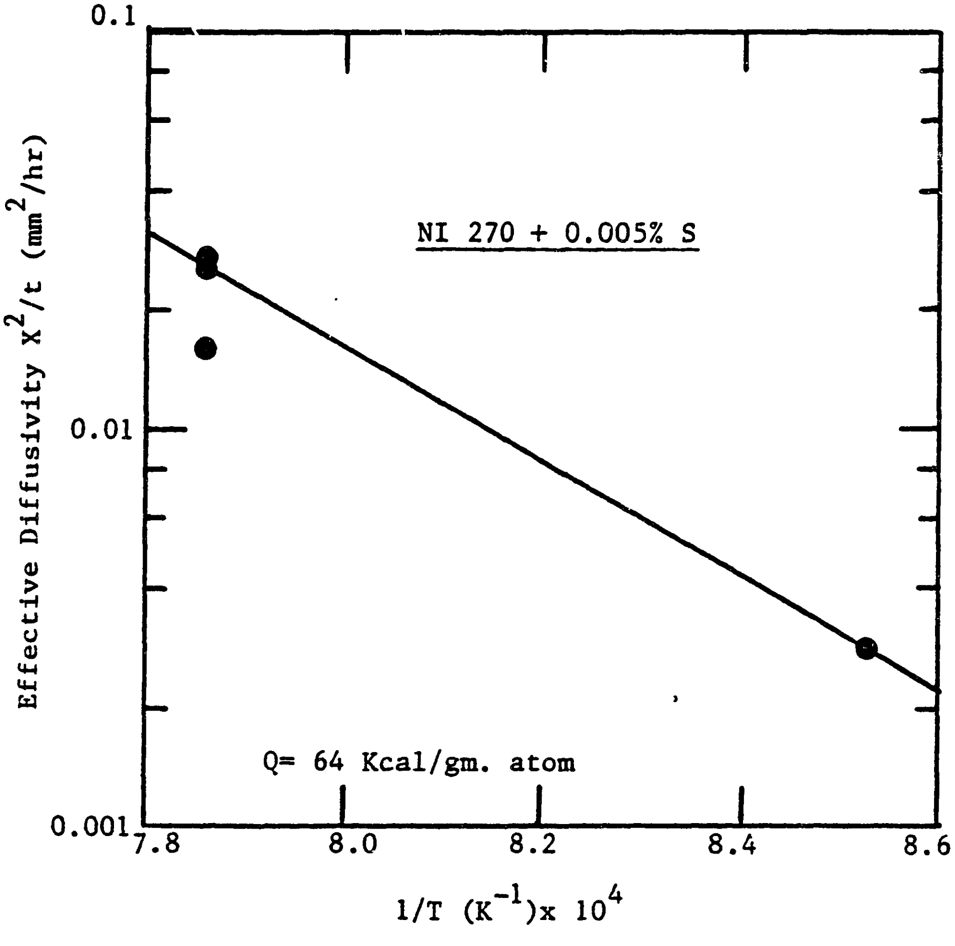

FIGURE 2.5) Depth of penetration of oxygen, X, in NI 270 + 0.005% S as a function of exposure temperature. (ref. 30)

embrittlement remains unknown. Several theories have been put forth to explain oxygen embrittlement. These theories are:

1. Gamma prime-oxygen reaction
2. Reduction of surface energy at $\gamma-\gamma'$ interfaces
3. Complex oxide formation along grain boundaries
4. Carbon dioxide bubble formation
5. Sulfur release due to oxidation of grain boundary sulfides.

The first mechanism is the γ'-oxygen reaction process. It has been proposed that oxygen will diffuse along the grain boundaries ahead of the crack tip and react with the fine γ' precipitates along the grain boundaries to form oxide particles and γ . This reaction is shown below:

$$\gamma' + (O) -- + M_xO_y \qquad \text{(Equ. 2.1)}$$

The removal of fine γ' particles along grain boundaries would reduce the strength of the boundaries and promote brittle intergranular fracture.

Oxygen has been observed to increase the rate of grain boundary cracks at γ' nodules in Udimet 500 (7). A severe grain boundary instability can exist in poorly alloyed or heat treated superalloys when aided by an applied tensile stress. Here large $M_{23}C_6$ carbides nucleate large nodules of γ' around their perimeter which deplete the surrounding grain boundary of its fine γ' particles. It is hypothesized that atomic oxygen diffusing down the grain boundaries reduces the cohesive strength between the γ matrix and the γ' nodules (23). The resulting cracks and the weakened grained boundaries result in a brittle fracture along the grain boundaries.

A third mechanism proposed by Woodford and Bricknell (30, 33) involves the formation of complex oxides along the grain boundaries by the mechanism given in equation 2.1. These complex grain boundary oxides then serve as additional nucleation sites for grain boundary cavities. The formation of numerous creep cavities will greatly accelerate grain boundary cracking and promote brittle fracture.

Another proposed mechanism for oxygen embrittlement of nickel-base alloys involves the formation of CO_2 bubbles at grain boundary carbides. (22) This mechanism is similar to the well known methane bubble formation in Cr-Mo-V steels in the presence of hydrogen at high temperatures. Oxygen diffuses into the material along the high diffusivity paths of the grain boundaries. Once in the alloy, the oxygen reacts with MC and $M_{23}C_6$ carbides to form CO_2 as shown in equation 2.2:

$$12(O) + M_{23}C_6 \rightarrow \gamma + 6CO_2 \qquad \text{(Equ. 2.2)}$$

The thermodynamic feasibility of carbon dioxide bubble formation has been determined by Dyson (31). The partial pressure of CO_2 gas is large (approximately 2000 MPa), and will result in the nucleation of bubbles at carbides and accelerate the early growth of these cavities. These cavities will link and cause a reduction in creep strength through premature grain boundary fracture. This theory suggests that a reduction in carbon content will reduce CO_2 bubble formation and since creep crack growth is an intergranular fracture process it will reduce the CCGR. A reduction in carbon content will detrimentally affect other creep properties and therefore may not be feasible.

Another mechanism involves the release of free sulfur into the grain boundary by a reaction with oxygen. Free sulfur release to the grain boundaries results from the oxidation of MnS particles in the grain boundaries through the following reaction:

$$(O) + MnS \rightarrow MnO + S \qquad \text{(Equ. 2.3)}$$

The presence of free sulfur in nickel alloys in concentrations as low as 10 to 20 ppm has been shown to severly embrittle grain boundaries (38). The oxidation of MnS particles has been observed in IN-738 and Ni-270 with the use of Auger microscopy (28, 29). While the release of free sulfur was observed, it could not be determined if it affected the ductility of these alloys since the formation of CO_2 bubbles was also observed.

All of the above embrittlement mechanisms depend on the diffusion rates of oxygen along grain boundaries. Elements which segregate to grain boundaries and reduce the number of vacancies can be expected to reduce the diffusivity of oxygen along grain boundaries. Alloying additions which increase the cohesive strength of the carbide-g.b. interface will inhibit the nucleation of grain boundary cavities and reduce the amount of embrittlement in the alloy by oxygen.

2.2.3. Effect of Grain Boundary Chemistry on Environmental Embrittlement

Several researchers have investigated the effect of alloying additions on the extent of oxygen embrittlement in nickel base alloys (22, 28, 30, 32).

Woodford (22) varied the composition of IN-738 in order to study the effect of boron, hafnium, and yttrium on the susceptibility of IN-738 to oxygen embrittlement. The time to rupture was measured in air and in vacuum for four heats of IN-738. Rupture lives of smooth bars were severely reduced after pre-exposures to oxygen or air at 1000°C for 200 hours. A slight decrease in rupture life was observed for bars exposed to N_2 gas, while exposure to a vacuum at 1000°C for 200 hours resulted in the longest rupture lives.

The rupture lives were severely reduced after oxygen pre-exposure at 1000°C when tested in a range of temperature from 700°C to 800°C. Oxygen pre-exposure had no detrimental effects on rupture life at 1000°C. The above creep rupture results are shown in Figure 2.6 as stress versus the Larson-Miller parameter. The addition of 1.5% hafnium to IN-738 gave the longest rupture time in air. The addition of only 0.1% boron also increased the rupture time in air, but the addition of 0.5% yttrium reduced the rupture times for IN-738. All of the heats gave approximately the same time to rupture when tested in a vacuum. This indicated that the addition of these elements affected the interaction between the alloy and oxygen.

Floreen and Davidson (32) found that the addition of 0.005% boron and .05% zirconium reduced the minimum creep rate and increased the time to rupture for alloy PE16. The B and Zr additions did not reduce the amount of grain boundary sliding, but did inhibit the formation of surface cracks in both air and helium environments. The creep strain versus time at 650°C measured in air and in helium for PE16 with and without B and Zr additions is shown in Figure 2.7.

The addition of boron to Ni200 (99.54% pure nickel) is observed to eliminate grain boundary embrittlement in air (30). The fact that Ni200 and Ni270 (99.99% pure nickel) do show severe grain boundary embrittlement by oxygen containing environments indicate that oxygen embrittlement

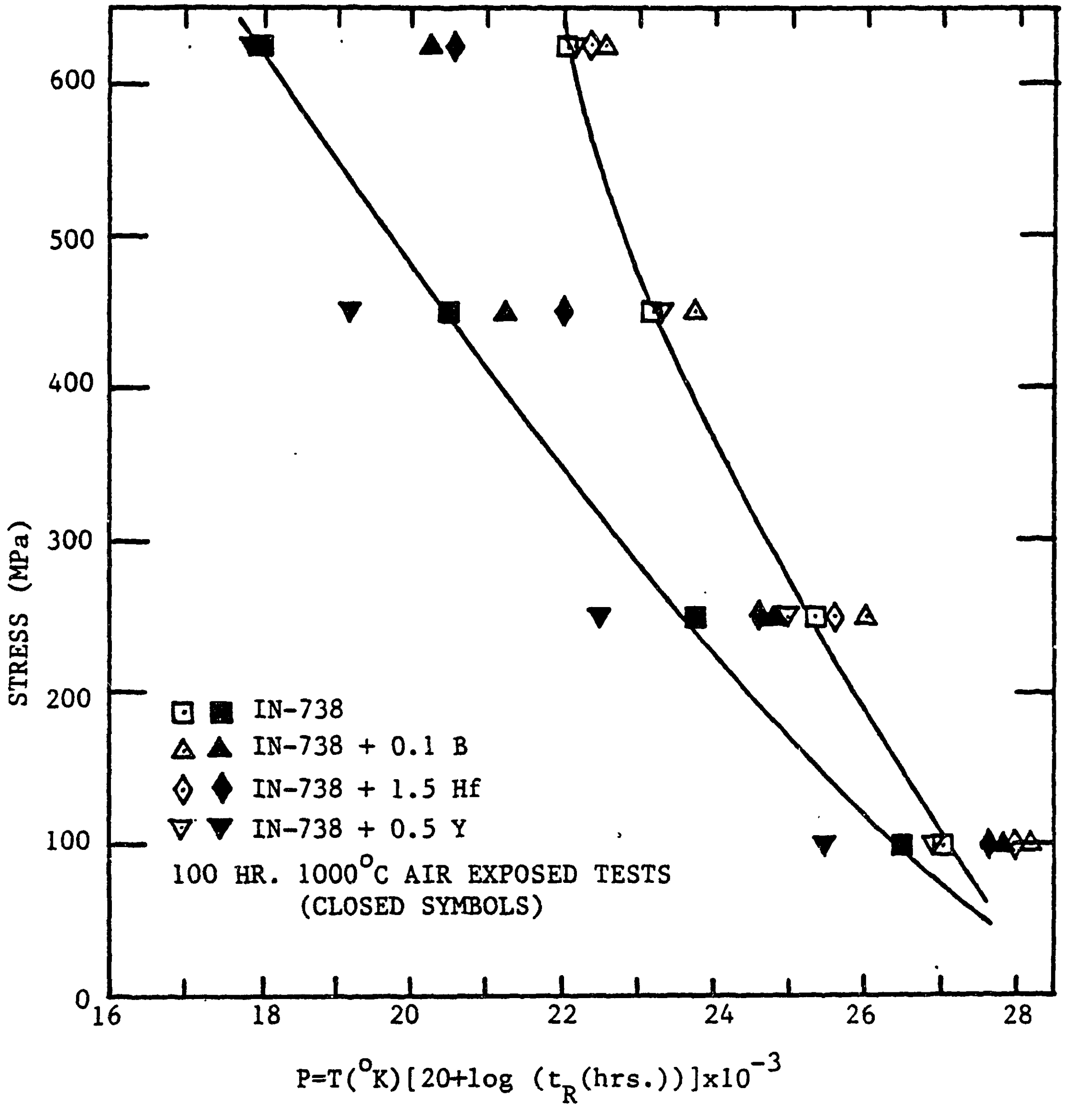

FIGURE 2.6) Comparison of creep-rupture life of IN-738 with four alloy variations with a pre-exposure in air and without a pre-exposure in air. (ref. 22)

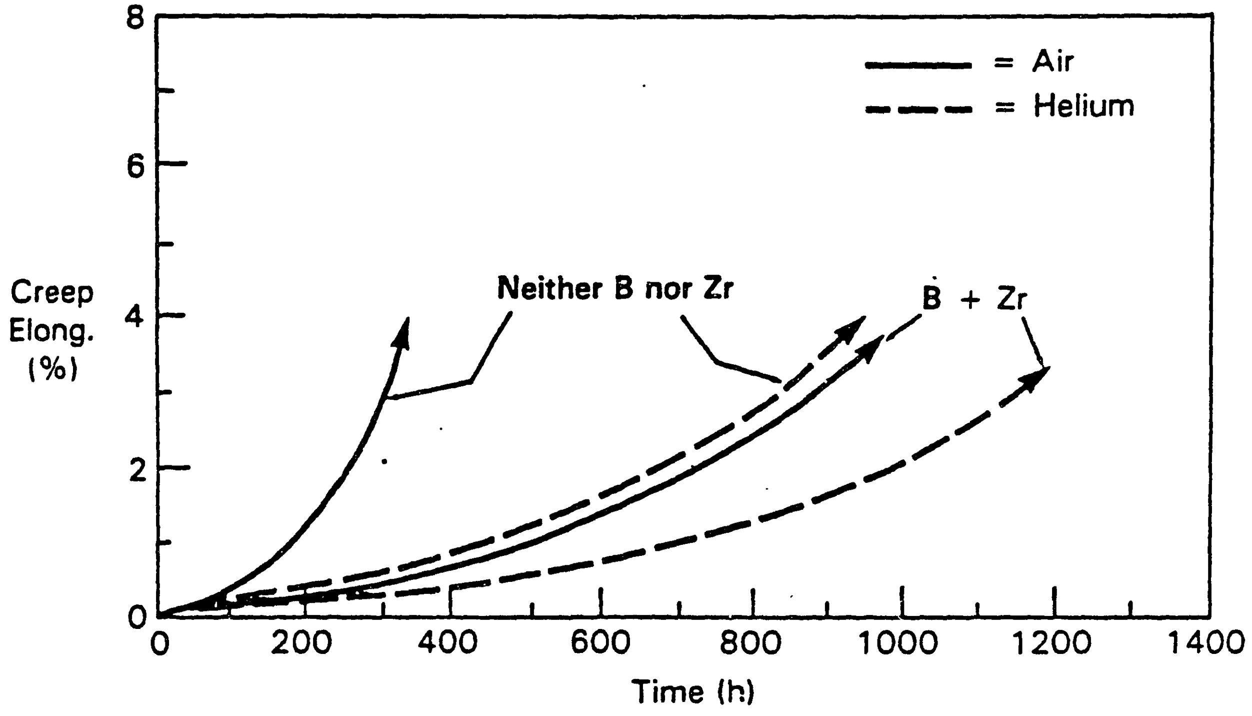

FIGURE 2.7) Comparison of smooth specimen creep tests for the alloy PE16 with both boron and zirconium or with neither boron nor zirconium. Tests performed in either air or helium at 650°C and a stress of 380 MPa. All tests interupted at approximately 4% Elongation. (ref. 32)

is a phenomenon which is inherent in the nickel alloy system. Since boron additions eliminate embrittlement in Ni200, models based on γ' - oxygen reaction, while possible, are not required for embrittlement. Boron appears to be very effective in eliminating the effect of oxygen on a fundamental level.

While the exact role of boron and other alloying additions which segregate to the grain boundaries is not clear, some conclusions can be derived. The effect of boron and zirconium additions on embrittlement of grain boundaries in nickel alloys is pronounced. The mechanisms by which these alloying additions work are very fundamental, since they are effective in very pure nickel. Boron may inhibit the diffusion of oxygen along the grain boundaries by occupying vacancies and slowing grain boundary diffusivity. (30)

2.3 Creep Crack Growth

Creep crack growth rates (CCGR) have recently been measured in several alloy systems: aluminum alloys (39-42), steels (43-48), and nickel base alloys (29, 35, 48-63). A wide variety of alloys, test specimen geometries, and test conditions have been reported. Several review papers have also been written (63, 64, 66). The following section will review the published work to date on creep crack growth rate results and test procedures.

2.3.1. Analysis of CCGR Testing Methods

CCGR tests have been performed using many specimen geometries including center cracked panels (CCP), compact tension specimens (CT), double cantilever beam specimens (DCB), double edge notch specimens (DEN), single edge notch specimens (SEN), and wedge opening load specimens (WOL) (64). Several researchers have added side grooves to the test specimens to promote a plane strain condition at the specimen surfaces, and to eliminate crack tip tunnelling (39, 47, 51, 53, 55, 57, 58, 62, 63). Crack tip tunnelling results from the creep crack growth rate being faster in the specimen center which has greater triaxiality than the specimen sides. Side grooves are often added to increase the triaxiality at the surfaces of the specimen.

All of the above specimens have certain advantages, but the CT specimen and the SEN specimen geometries are the most widely used. The CT specimen affords a low rise in the stress intensity with crack advance and the test procedures and K-calibration are well documented. The SEN specimen allows a complete CCGR versus K plot to be generated from a single test because of a steep dK/da, and the K-calibration is equally well known. Since the lack of side grooves has been observed to result in crack tip tunnelling, accurate measurement of crack length is impossible, and therefore CCGR results obtained from ungrooved specimens are questionable (39, 59).

Crack length is usually determined via the electrical potential difference technique (58, 59). Optical (47) and compliance techniques for crack length measurement are also employed (47). Optical crack length measurement is only accurate for a polished smooth specimen surface. The lack of side grooves will result in crack tip tunnelling and therefore all results obtained by optical techniques will under-estimate the crack length and the CCGR.

Creep crack growth rates have been correlated using the stress intensity factor (K), the crack opening displacment (COD), the J-Integral for plasticity (J), the C*-integral for time dependent plasticity (C), and the net section stress (σ_{net}). Several studies have been published comparing the practical applicability of these correlating parameters (41, 46, 52, 53, 59, 64, 66). The CCGR is best correlated by the C* parameter in creep-ductile materials. There is a possibility, however, that the method used to determine C* yields a value of C* which is a function of crack growth rate. (64,66) The C* parameter is measured from the rate of COD. This depends strongly on the crack growth rate. Correlations of CCGR data with C* when C* is a function of the CCGR results in the situation of correlating CCGR versus CCGR (67). While the correlations with C* appear good, the results cannot be used to predict the CCGR behavior when different initial conditions of load and crack length are used. CCGR tests on IN-718 (52), Udimet 700 (53) and IN-100 (59), all nickel-base alloys, indicate that the stress intensity factor, K, gives the best correlation of CCGR. The definition of creep-brittle and creep-ductile are given in section 2.4.

The creep crack growth rate versus K curves usually exhibit three stages (Figure 2.8) (64). Stage I is a region of quickly increasing CCGR with K. Stage II is similar to the well known Paris Law regime observed for fatigue crack growth. Stage III corresponds to a rapidly increasing CCGR near K . The stage I behavior does not appear to be a unique function of K and tests which are started at high initial values of K may only exhibit Stage I and Stage III behavior. Figure 2.9 shows results for .5% Cr-.5% Mo-.25% V steel at 565 °C by Nikbin et. al. (41) and Neute and Siverns (66), and the effect of initial K on the CCGR behavior of an alloy are obvious. A higher initial K resulted in a lower CCGR versus K and a steeper slope for the CCGR versus K curve. The higher initial K tests did not have a Stage II region of CCG.

In general the test procedures, specimen design, crack length measurement technique, and correlating parameters reported for CCGR testing in the literature result in a complex array of often conflicting and inconsistant data. These differences reflect the lack of a proper understanding of the creep crack growth fracture processes.

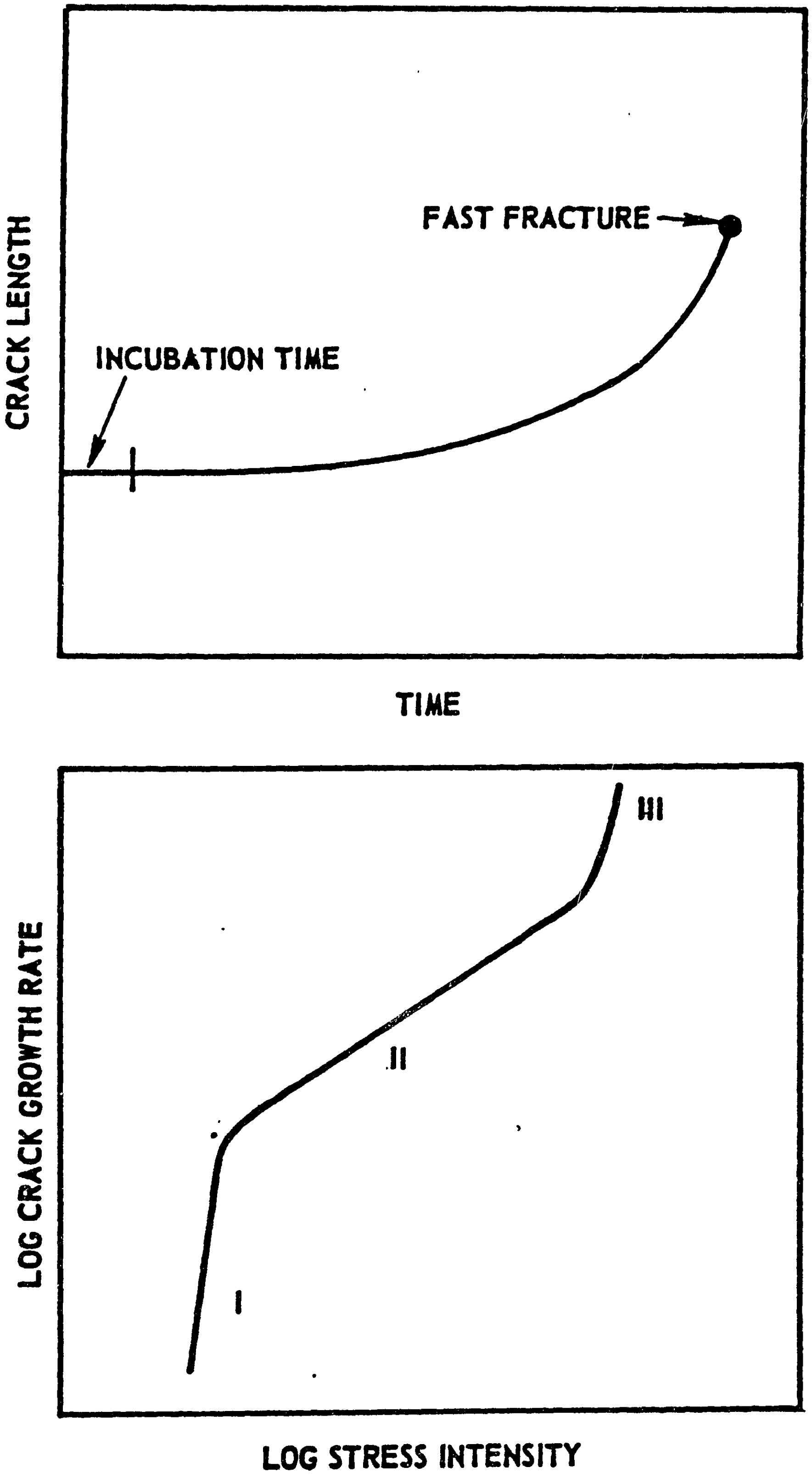

FIGURE 2.8) Schematic illustration of crack growth data. (ref. 64)

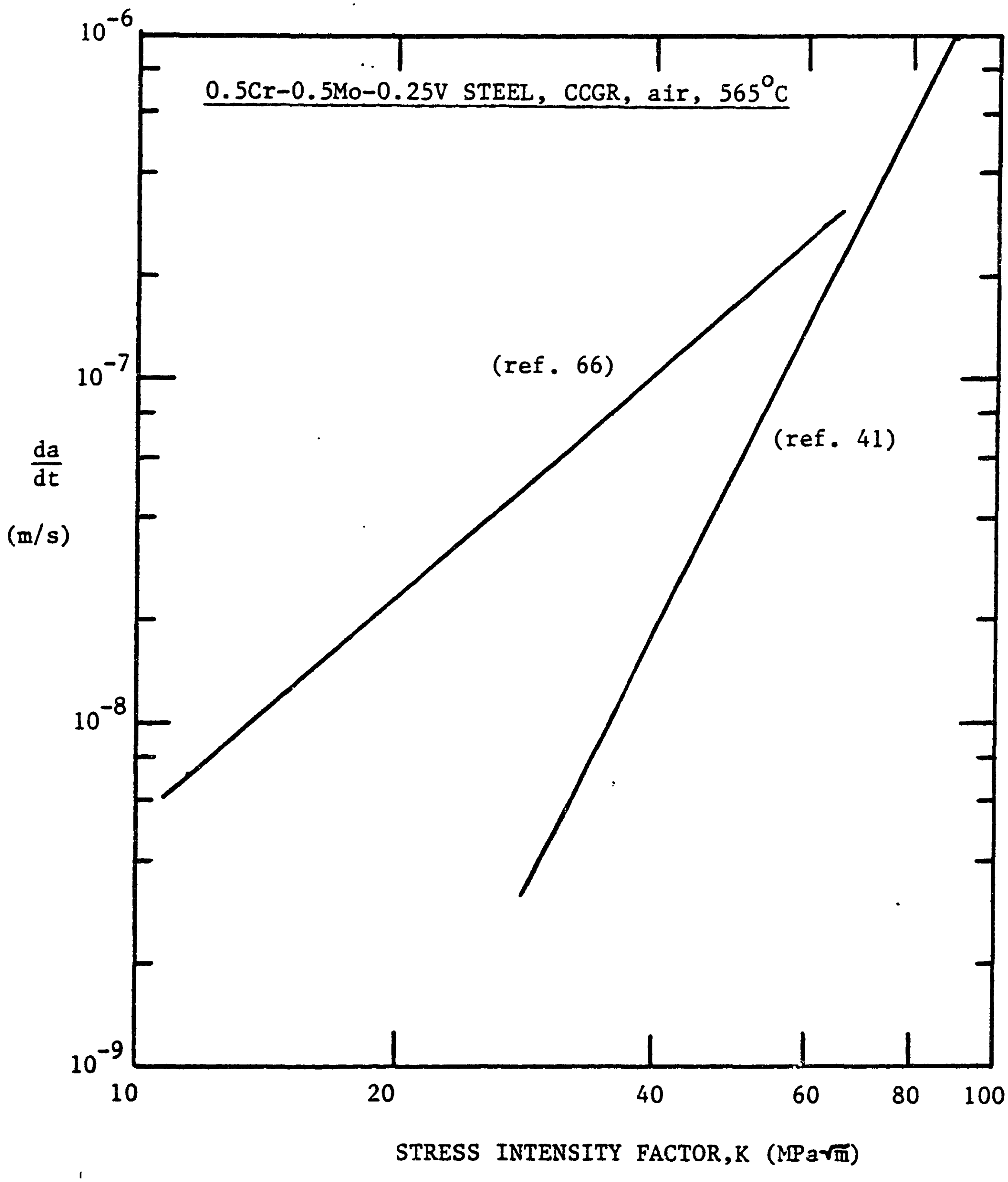

FIGURE 2.9) Comparison of CCGR results for 0.5Cr-0.5Mo-0.25V steel in air at 565°C with different initial K. (ref. 41,66)

2.3.2. CCGR in Various Nickel Base Alloys

CCGRs have been determined for many Ni-base alloys in both air and inert environments from 530°C to 850°C. CCGR results in the literature for Ni-base alloys are listed in Table 2.4. The results in Table 2.4. are for a variety of test conditions, specimen designs, and crack length measurement techniques. In general the stress intensity factor was observed to give the best correlation of the test results. The CCGRs for these alloys at 704°C are shown in Figure 2.10. A wide range of results has been obtained for the Ni-base alloys. Some of the scatter in the results originates from inaccurate tests procedures and initial conditions which result in CCGR versus K data which do not appear to be a unique function of K.

TABLE 2.4.

CCGR Results for Nickel-Base Alloys from Literature

ALLOY	TEMPERATURE (°C)	ENVIRONMENT	REFERENCE
Astroloy	655, 704, 725, 760	Air	51, 63
Astroloy	655, 704, 760	Vacuum	51, 63
Astroloy	704	Air	50
Udimet 700	650, 750, 850	Air	53
Udimet 700	850	Air	48
Udimet 700	850	Vacuum	48
IN-100	732	Air	59
IN-100	650, 700	Air	57
MERL-76	704	Air	61
Rene-95	650, 704, 760	Air	58, 62
Rene-95	650, 760	Argon	58
Rene-95	704	Air	50
X-750	540, 650	Air	48
X-750	540, 650	Vacuum	48
X-750	650	Air	55
X-750	650	Argon	55
IN-718	538, 650, 704, 760	Air	52
IN-718	704	Air	50
IN-718	650	Vacuum	49
IN-718	650	Air	56
IN-718	650	Vacuum	56
IN-718	540, 650	Air	48
IN-718	540, 650	Vacuum	48
NIMONIC 115	704	Air	50
AF 115	704	Air	61
NIMONIC 105	750	Air	54
IN-738 LC	850	Air	54
B6	704	Air	61
Waspaloy	704	Air	50
PE16	650	Air	32
PE16	650	Helium	32

The effect of temperature on CCGR behavior in Ni-Base alloys has been extensivly studied. (48, 51, 52, 58, 62, 63) The results for PM/HIP low Carbon Astroloy by Huang (63) in Figure 2.11 are given as an example of the effect of temperature on CCGR. The results of all reported research

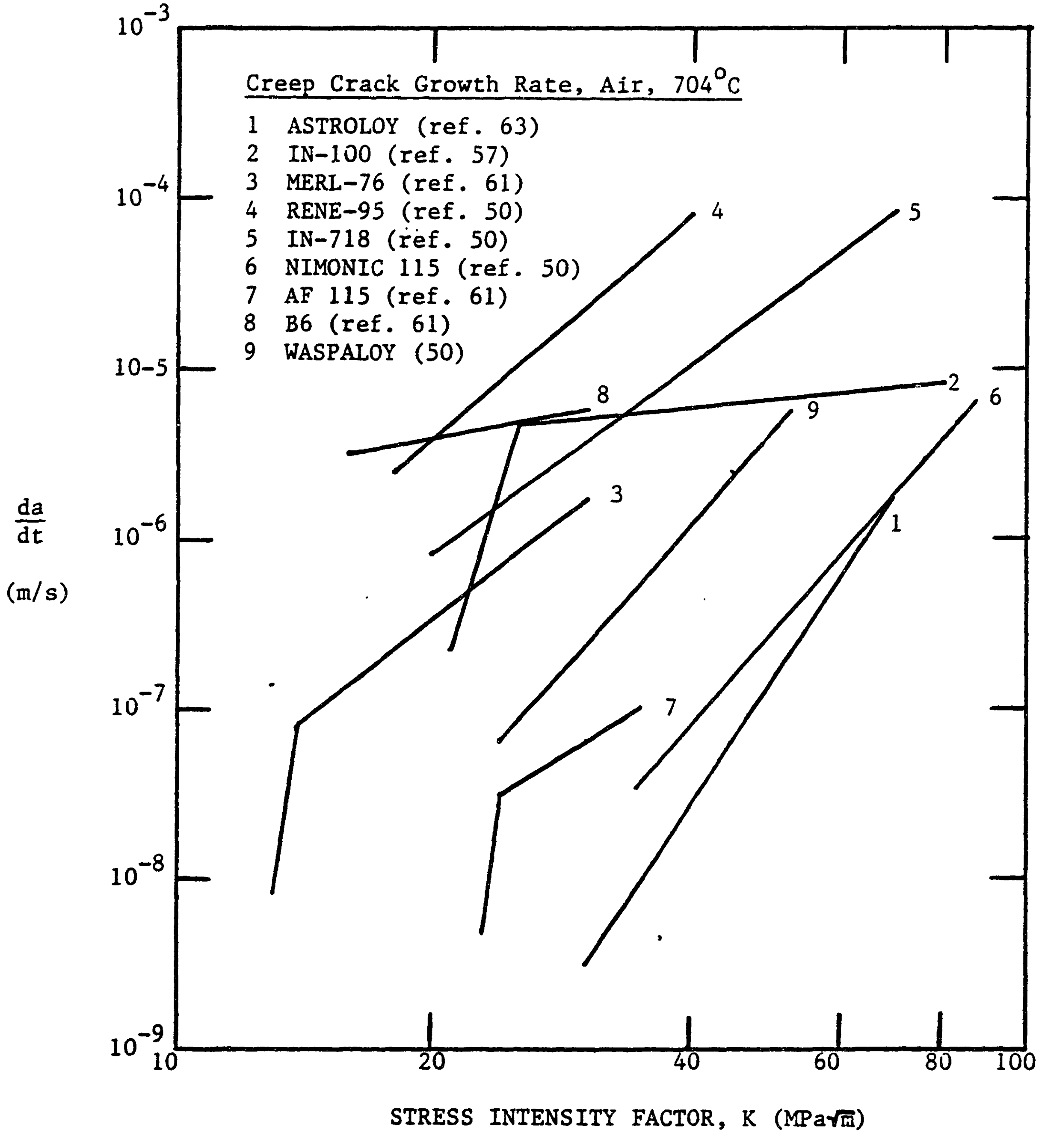

FIGURE 2.10) Typical CCGR data for several Nickel -base alloys in an air environment at 704°C.

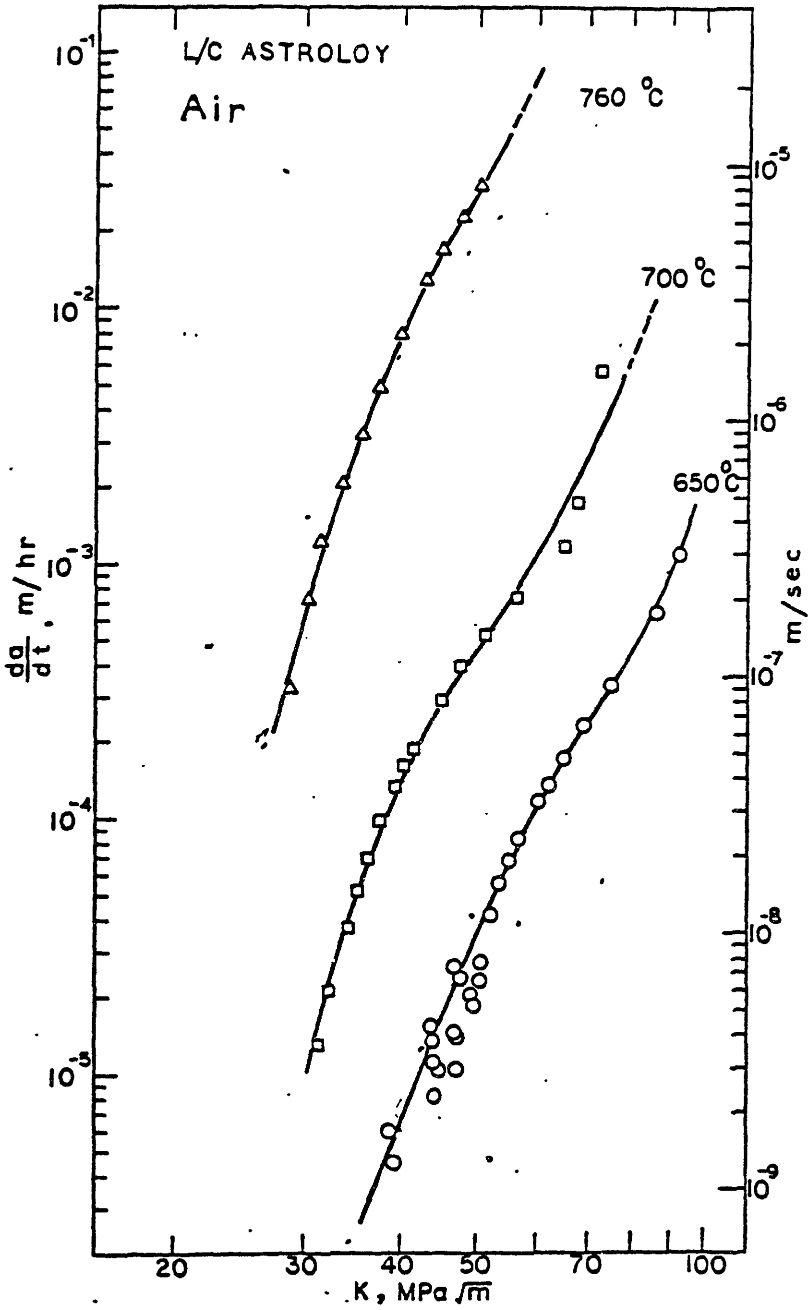

FIGURE 2.11) Comparison of CCGR results for PM/HIP low Carbon Astroloy tested in air at three different test temperatures. (ref. 63)

indicates that in the range of temperatures tested the CCGR increases significantly with increasing temperature.

The fracture surfaces for all the Ni-Base alloy tests was totally intergranular, and the tests in air displayed an extremely brittle fracture mode with very little visible ductility or cavitation.

2.3.3. Air Embrittlement of Ni-base Alloys

The effect of oxygen on the CCGR has been studied by Huang (63) on Astroloy, Sadananda and Shahinian (49, 51) on In-718, X-750, and Udimet 700, Pineau (56) on IN-718, and by Floreen (32) on PE16, and Bain (58) on Rene-95. The effect of oxygen on CCGR ranges from only a slight increase in CCGR for Astroloy to a 1000 times increase in the CCGR for IN-718 and Rene-95.

Figure 2.12 shows the range of air and inert environment results for several Ni-base alloys at 650°C. The CCGR results in an inert environment are in a narrow range of CCGR well below the air results. This is not surprising since all the alloys have essentially similar creep and tensile properties at this temperature. The CCGR in air were much faster than in an inert environment but the amount of increase in the CCGR varies significantly from alloy to alloy. The effect of oxygen on CCGR depends strongly on each alloy's ability to resist oxygen embrittlement. The ability of an alloy to resist CCGR in air are probably linked to the same alloying additions which

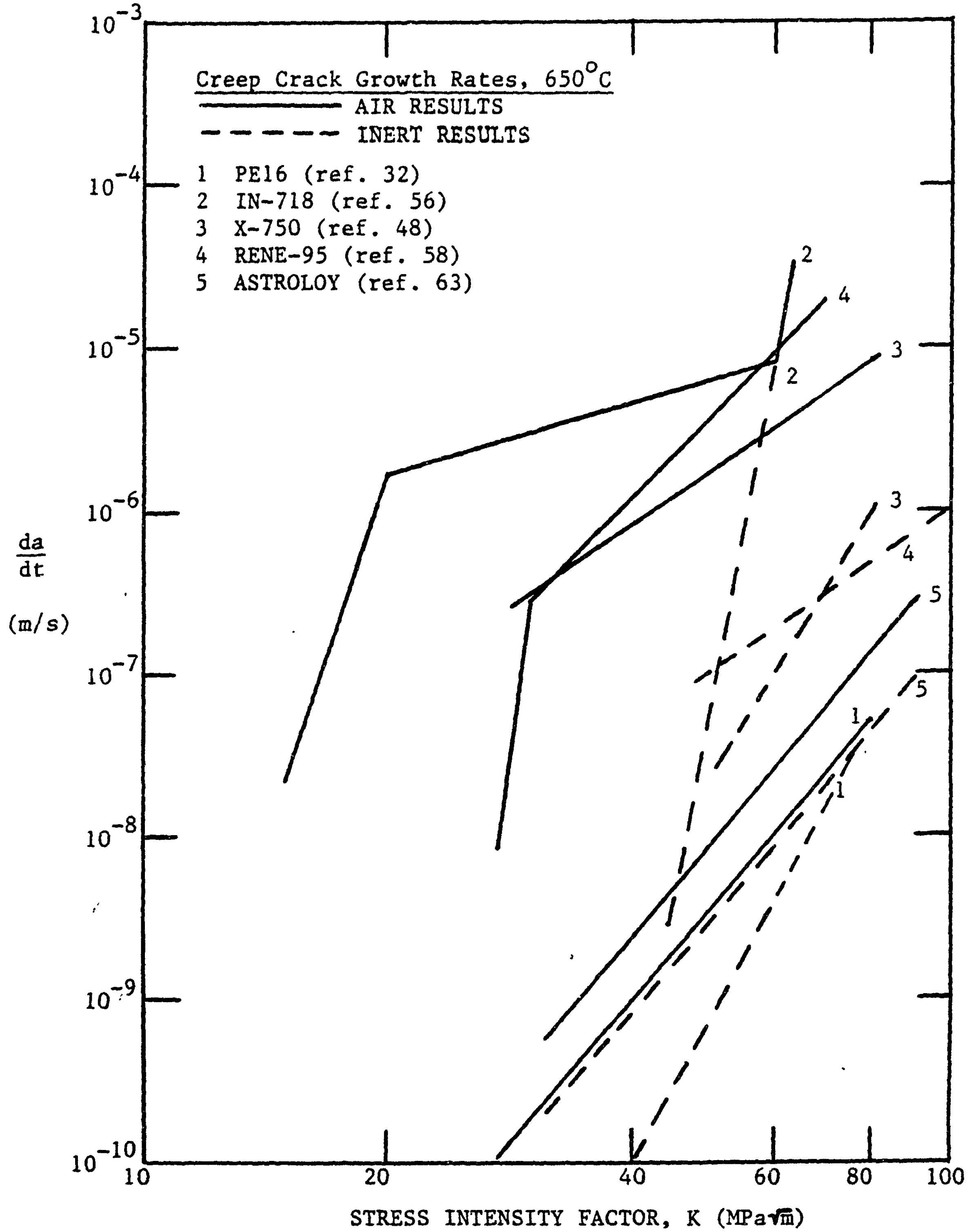

FIGURE 2.12) CCGR results for several Nickel-Base alloys for both air and an inert environment

have been shown to eliminate oxygen embrittlement in Ni-base alloys described in section 2.2.

2.3.4. Effect of Microstructure on CCGR in Ni-Base Alloys

Floreen (35, 68) has studied the effect of grain size on the CCGR of IN-792 in air at 704° C. It was found that increasing the grain size from 8um to 250um results in a decrease in the CCGR. The results for IN-792 are reported in Figure 2.13 as a plot of the initial stress intensity factor versus time to failure for precracked CT specimens. The finer grain size produced a sharp reduction in the time to failure. Similar results were obtained by Pineau (67) on IN-718 at 650°C and by Law and Blackburn (61) on AF 115 at 704°C.

Wu and Pelloux (57) varied the heat treatment of IN-100 and studied its effect on CCGR at 700°C in air. The results are shown in Figure 2.14. The heat treatment which eliminated grain boundary carbides (treatment C and D) showed a reduction in stage II creep crack growth rates. Heat treatment C produced a smaller grain size (3.5 um grain size), than heat treatment D (40 um grain size) which resulted in an increase in the CCGR for treatment C. The results indicate that the CCGR of an alloy are significantly affected by thermal treatment and processing.

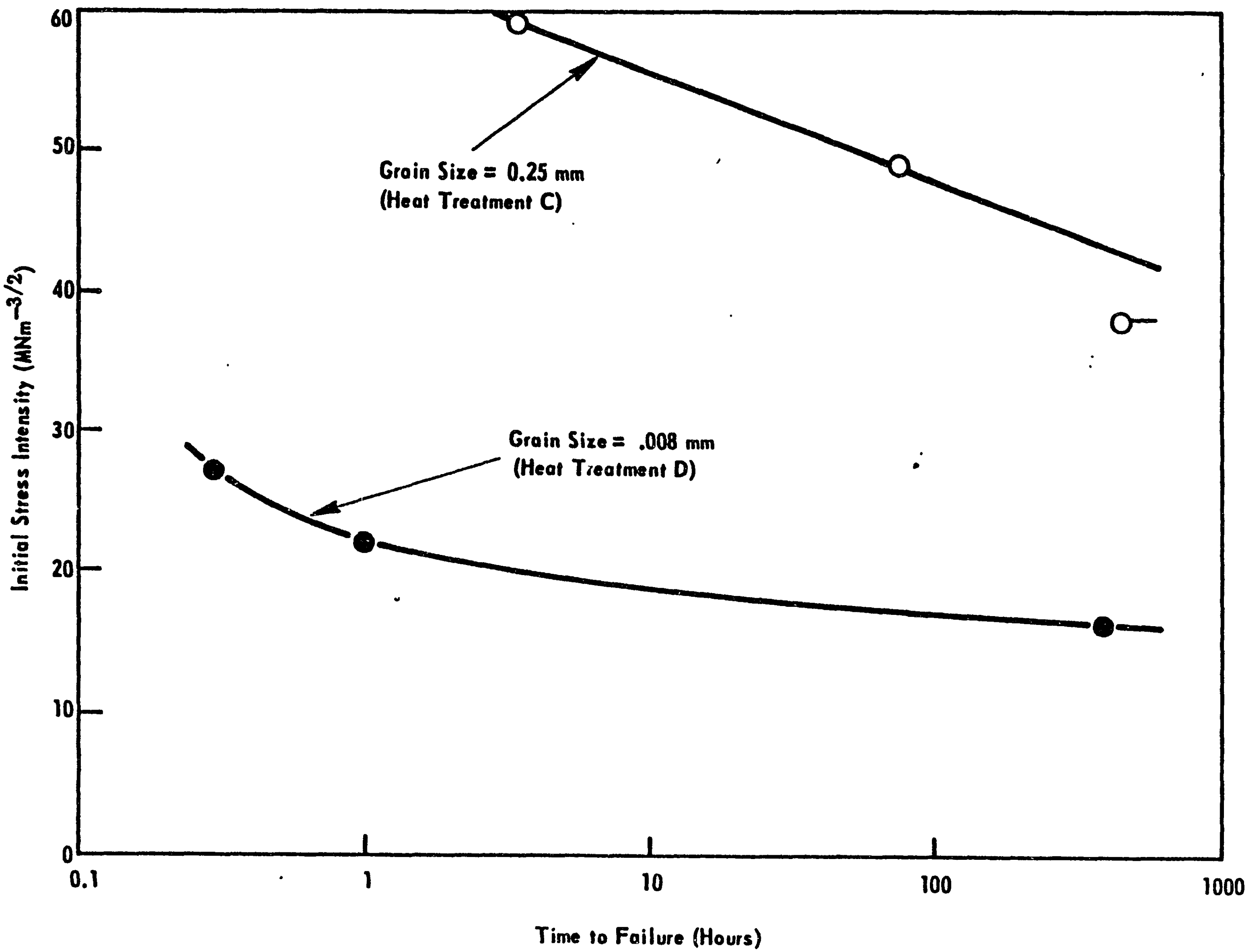

FIGURE 2.13) Effect of grain size on fracture of IN-792 at 704°C. (ref. 35)

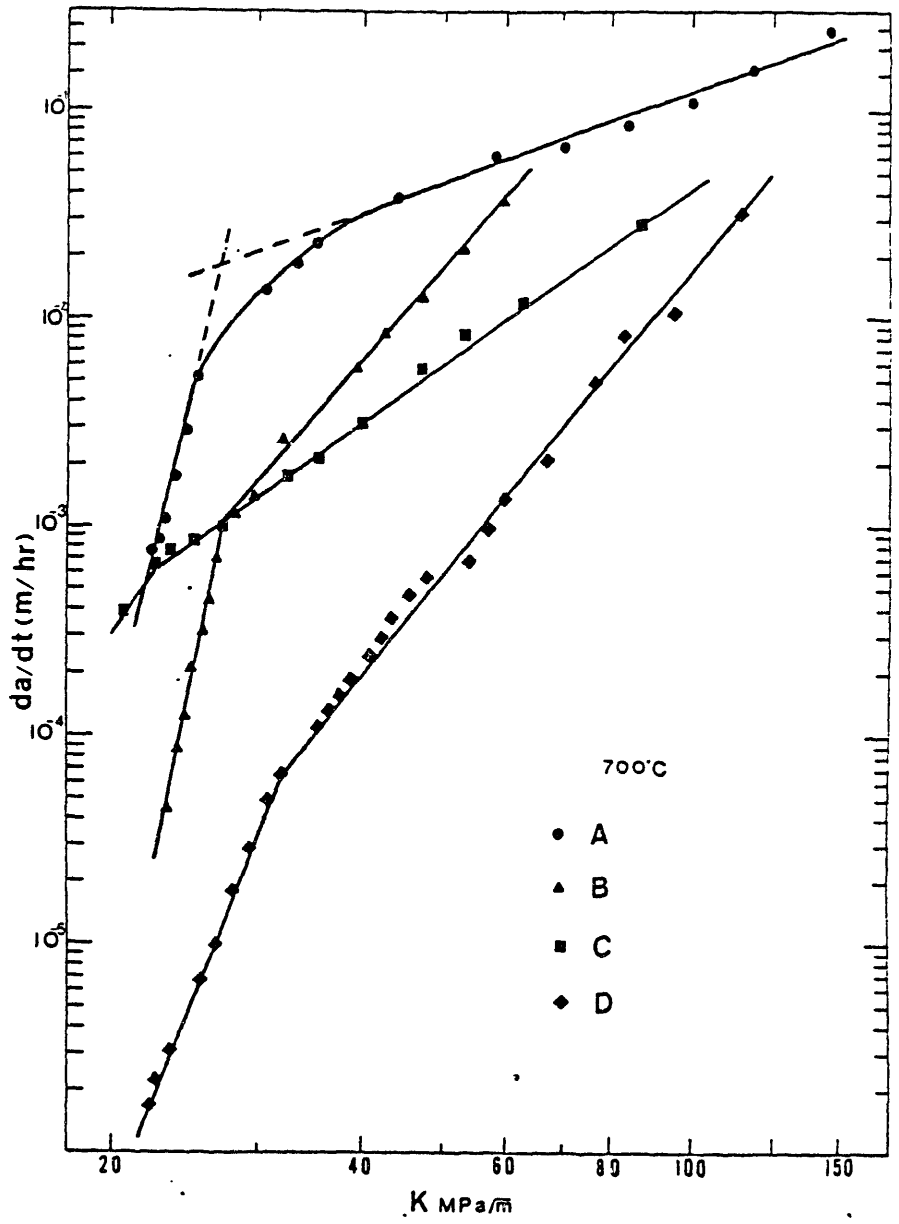

FIGURE 2.14) Comparison of CCGR results for IN-100 in air at 700°C with four different heat treatments (A-D). (ref. 57)

2.4. Theories of Creep Crack Growth

Creep crack growth is generally thought to be a process in which a single macro-crack advances through a material at high temperature (T>.5 Tm) as a result of the nucleation, growth and coalesence of grain boundary cavities ahead of the crack. Cavity nucleation and growth result from the existance of high stresses and strains in the region ahead of the crack tip.

Cavity growth theories are based on either the diffusional growth of cavities by vacancy transport or creep constrained cavity growth. Creep constrained cavity growth is essentially the same as diffusional growth with the exception that the cavity growth rates are limited by the accommodation of the matrix via bulk creep plasticity.

CCGR models have been developed on the assumption of one of the above cavity growth mechanisms. These CCGR models are based on the time dependance of crack tip stresses.

2.4.1. Crack Tip Stress Distribution

A study of creep crack growth theories must begin with a description of the state of stress ahead of the crack tip. Several good reviews of crack tip stress calculations have been written by McClintock and Bassani (65), Huang (63), and Bensussan et. al. (39). The stresses ahead of a crack are complicated by the accumulation of creep deformation which relieves the stresses with time.

In the elastic region where the elastic strains (ε^e) are dominant, the stresses, for small scale yeilding, are given by the usual singular field (69):

$$\sigma_{ij}=\frac{K_I}{\sqrt{2\pi r}} f_{ij}(\Theta) \qquad \text{(Equ. 2.4)}$$

Where K_I is the mode I stress intensity factor, "r" is the distance ahead of the crack tip, and $f(\Theta)$is a function which varies with the angle from the plane of the crack.

In the plastically deformed region ahead of the crack tip, the material is assumed to harden with plastic strain (ε^P) by power law hardening:

$$\varepsilon^P=B_p(\sigma)^{N_p} \qquad \text{(Equ. 2.5)}$$

where ε^P is the plastic strain, B_p and N_p are material dependant parameters. The stresses at time=0 in the region where plastic strain dominates are represented by the Hutchinson, Rice, and Rosengren (HRR) singularities (70-72):

$$\sigma_{ij}=\left(\frac{J}{B_p\, I_{N_p} r}\right)^{(1/(N_p+1))} f_{ij}(N_p,\Theta) \qquad \text{(Equ. 2.6)}$$

where the loading parameter is the J-integral (73), and $I_{N_p} \approx \pi$.

As time increases creep strain will accumulate ahead of the crack. The accumulating creep strain will relax the crack tip stresses.

The minimum creep rate with applied stress is given by the following power law expression:

$$\dot{\varepsilon}^c=B_c(\sigma)^{N_c} \qquad \text{(Equ. 2.7)}$$

where $\dot{\varepsilon}^c$ is the creep rate, B_c and N_c are material dependent parameters. If the plastic strains are neglected, the stresses in the region where the creep strain is the dominent factor are given by the Riedel and Rice (RR) singularity (74) which is analogous to the HRR singularity:

$$\sigma_{ij}=\left(\frac{C(t)}{B_c\ I_{N_c}\ r}\right)^{(1/(N_c+1))} f_{ij}(N_c,\Theta) \qquad \text{(Equ. 2.8)}$$

where C(t) is given below:

$$t<t_{tr} \qquad C(t)=\frac{J}{(N_c+1)\ t} \qquad \text{(Equ. 2.9a)}$$

$$t>t_{tr} \qquad C(t) = C^* \qquad \text{(Equ. 2.9b)}$$

where C^* is the time dependent C^* integral (75), and t_{tr} is the creep transition time. The creep transition time is given by:

$$t_{tr}=\frac{J}{(N_c+1)\ C^*} \qquad \text{(Equ. 2.10)}$$

Another expression for the transition time has been suggested by McClintock and discussed by Huang (63):

$$t_{tr} = \frac{\varepsilon_\infty^e}{\dot{\varepsilon}_\infty^c} = \frac{\sigma_{net}}{E\,\dot{\varepsilon}_\infty^c} \qquad \text{(Equ. 2.11)}$$

where $\dot{\varepsilon}_\infty^c$ is the creep rate in the far field, E is Young's modulas, and σ_{net} is the net section stress.

The transition time approximates the time to relax the stresses at the tip of the crack. If t<< transition time, the stresses have not relaxed significantly and the alloy is called creep-brittle. If the time = transition time, the stresses will have significantly relaxed.

The J-integral for small scale yielding condition can be approximated as for plane strain (73):

$$J = \frac{(1-\nu^2)\,K_I^{\,2}}{E} \qquad \text{(Equ. 2.12)}$$

Therefore, when the conditions of small scale yielding apply in a creep brittle material the stresses and strains ahead of the crack tip can now be described by K_I. These conditions generally apply for Ni-base alloys operating in modern gas turbines, and, therefore, K_I is the parameter which is being used to correlate CCGR data.

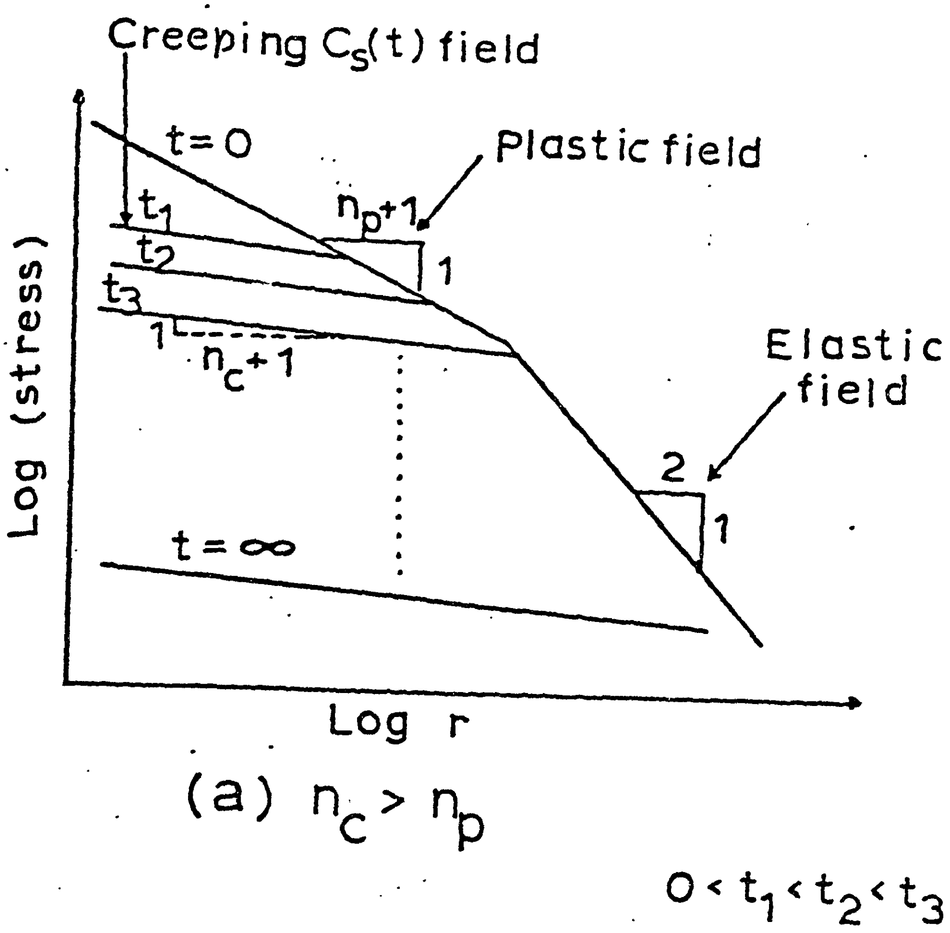

FIGURE 2.15) Schematic crack tip stress distribution versus time in a creeping solid. (ref. 63)

The above relationships are used to calculate stresses ahead of a crack tip in Astroloy (Figure 2.15) (63). The calculated stresses are highest upon loading at t=0 and are given by the HRR singularity. As time progresses the stresses given by the RR singularity slowly relax.

2.4.2. CCGR Models

There have been several attempts to predict creep crack growth rates in metallic materials. The models are based on either diffusional growth of cavities (76-79) or by power law creep deformation controlled cavity growth as suggested by Hancock (80). Power law creep has been coupled to diffusional cavity growth by Argon (81) and Chen (82).

2.4.2.1. Diffusional Creep Models

Diffusion models have been proposed by Vitek (83), Pilkington (84), and Raj. et al. (85):

Vitek:
$$\frac{da}{dt} = \frac{.516\ \delta\ D_B \Omega}{k\ T\ d^4} \left(\frac{K}{E}\right)^4 \qquad \text{(Equ. 2.13)}$$

Pilkington:
$$\frac{da}{dt} = \frac{1}{\sqrt{2}} \quad \frac{D_s \Omega^{4/3}}{kT\ \gamma_s^2} \frac{(2\lambda^3)(d)^{1/2} K^3}{(1-\gamma_B/\gamma_s)^{3/2}(\lambda-R_o)^4 (2\pi)^{3/2}} \qquad \text{(Equ. 2.14)}$$

Raj et al.:
$$\frac{da}{dt} = 7 \times 10^5 \frac{\Omega\ \delta\ D_s\ K^2}{E\ k\ T\ \lambda^3} \qquad \text{(Equ. 2.15)}$$

where:

E - Young's modulus

δD_B - Grain boundary thickness multiplied by grain boundary diffusion coefficient

Ω - Atomic volume of controlling diffusion species

k - Boltzman constant

T - Temperature (absolute)

s - Crack width

K - Stress intensity factor

D_s - Surface diffusion coefficient for controlling species

γ_s - Surface energy of matrix

γ_B - Surface energy of grain boundary

R_0 - Radius of cavity nuclei

λ - One-half cavity spacing.

The diffusional models predict a CCGR dependance on K with a slope between 2 and 4. CCGR tests performed in inert environments, however, have given results which have a higher slope in the Stage IIregion of creep crack growth. (63) These models do not account for the effect of plastic strain on the crack tip stress field, environmental damage is not considered, and the Stage I CCGR behavior is not predicted.

2.4.2.2. Deformation Controlled CCGR Models

Deformation controlled models have been proposed by Barnby, (86) Nix, (87) and Pilkington. (84)

Barnby: $$\frac{da}{dt} = \frac{\dot{\varepsilon}_o}{\sqrt{dt}} \left[\frac{\sigma_{net}}{\sigma_o}\right]^{N_c} \qquad \text{(Equ. 2.16)}$$

Nix: $$\frac{da}{dt} = \frac{B_c K^{N_c} (d)^{(-N_c/2 + 1)}}{\ln(\frac{\lambda}{R_o}) (\pi)^{N_c/2} (N_c-2)} \qquad \text{(Equ. 2.17)}$$

Pilkington: $$\frac{da}{dt} = \frac{B_c K^{N_c} (2\lambda)^{(-N_c/2 + 2)}}{\ln(\frac{\lambda}{R_o}) (\lambda) (2\pi)^{N_c/2} (N_c-2)} \qquad \text{(Equ. 2.18)}$$

where "d" is the grain size, and σ_{net} is the net section stress ($\dot{\varepsilon}^c = B_c \sigma^{N_c}$).

The deformation models predict that the CCGR dependence on K is given by N_c, the creep exponent. This slope is approximately the slope of the observed Stage I CCGR behavior, but the observed stage two CCGR behavior is not predicted. Again, as in the diffusional CCGR models, these models do not predict any effect of environment. A review of CCGR models was given by Huang (63)

2.4.3. Iterative CCGR Models

An iterative computer model of CCGR was attempted by Huang (63). This model calculated damage ahead of the crack tip in terms of average grain boundary cavity radius along the grain boundaries ahead of the crack tip. The crack tip advances by one grain-diameter when the average cavity size equals the cavity spacing in the grain immediately ahead of the crack tip. Huang calculated the stress field using the HRR, RR, and elastic singularities already described, and the stresses were allowed to relax with time.

The idea of damage accumulation and creep relaxation of stress represent a realistic view of the actual conditions which are believed to exist during creep crack advance. The slope of the predicted CCGR versus K curves will vary with crack advance and K. The slope will be initially large and decrease as damage accumulates ahead of the crack. The model proposed by Huang (63) predicts a high dependance of CCGR on K in the region of Stage I growth. The slope decreases with increasing K as a result of the increase in the number of grains in the plastic zone ahead of the crack tip.

The only major problem in the Huang model results from the calculation of stress versus time. The stress in the loading direction was used to predict cavity growth rate rather than the equivalent stress. The stress in the loading direction is much larger than the equivalent stress. An adjustable parameter $\tilde{\sigma}_{11}(\theta)$ was used to correct for this over prediction of stress. The model also assumes there is no relaxation of stresses ahead of the crack tip until the stresses predicted by the RR-singularity drop below the stresses calculated from the HRR-singularity. The stresses ahead of the crack tip should begin to relax immediately after loading due to the high stresses in the plastic zone ahead of the crack. The RR singularity is only valid at t=0 when the plastic strains are small when compared to the creep strains. However, This is not the situation ahead of the crack tip at t=0 in creep crack growth. The stress and creep strain accumulation at a point ahead of the crack tip with time is shown schematically in Figure 2.15. The consequence of assuming the stress relaxation beginning with t = 0 is that creep strain accumulates too fast and the creep crack growth rate is over-predicted.

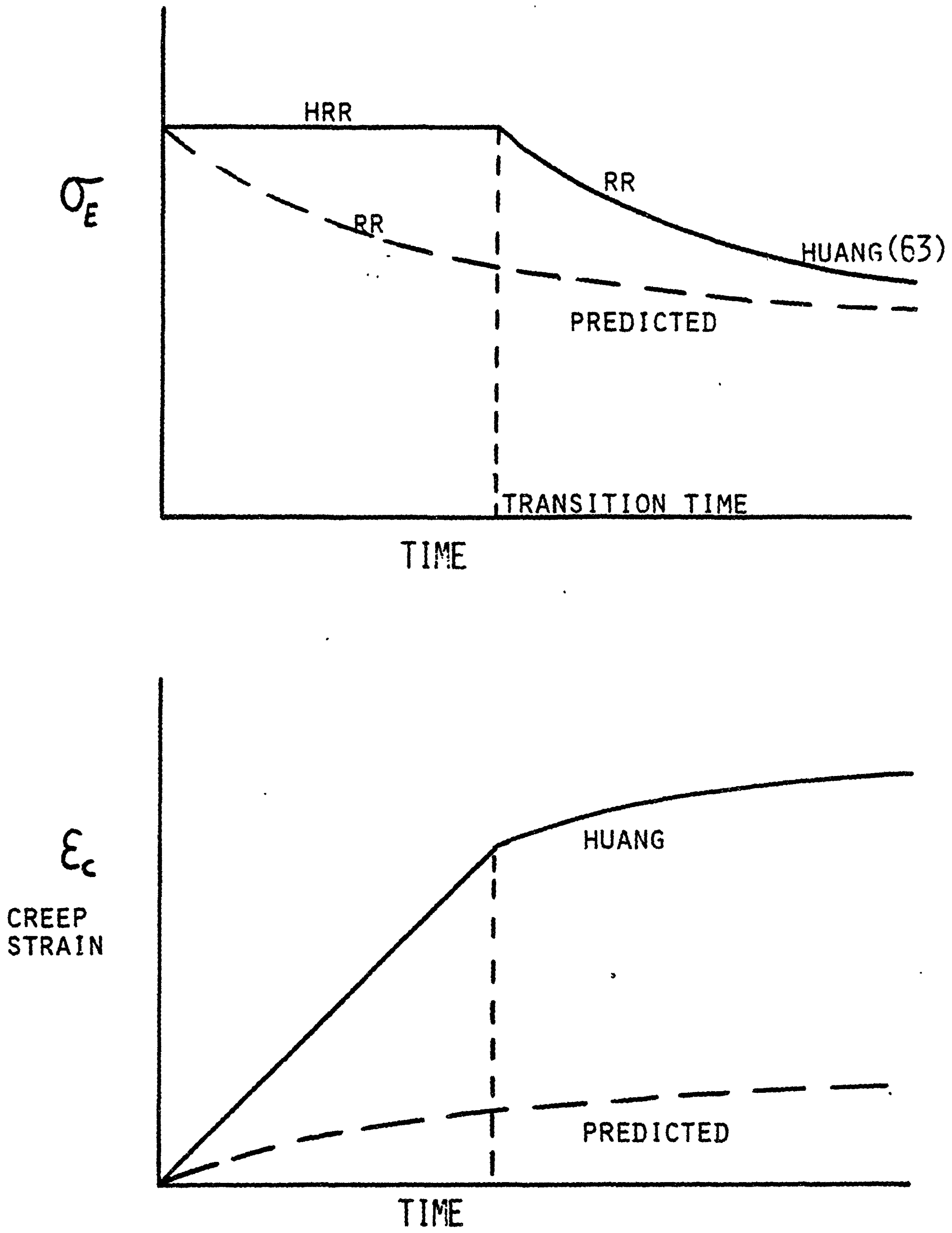

FIGURE 2.16) Stress and strain ahead of the crack tip versus time from the computer model given by Huang(63) and the predicted values in the present model.

EXPERIMENTAL PROCEDURES

3.1 Materials

Four γ / γ' nickel base superalloys were chosen for this study. They are Low Carbon Astroloy, Merl-76, Low Carbon IN-100, and Rene-95. These alloys were chosen for their varying susceptibility to grain boundary embrittlement in oxygen. The alloys were produced by HIP processing of PM alloys into 9/16" diameter rods. The powder mesh size for each alloy is shown in Table 3.1 along with the maximum particle diameter. Rene-95 was obtained in two mesh sizes.

Table 3.1

	Powder Size	
	Mesh Size	Particle diameter, μm
Astroloy	100	149
Merl-76	325	45
IN-100	60	250
Rene-95	60	250
Rene-95	120	125

3.1.1. Chemistry and Processing

The thermal and HIP processing parameters for the alloys are given in Table 3.2. The heat treatment used was chosen to yield similar mechanical properties for all the alloys.

TABLE 3.2.

Thermal Processing
1. HIP Cycle
a. Astroloy - 1232° C/4 hours/Furnace cool/15 Ksi
b. IN-100, Merl-76, Rene-95 - 1177°C/4 hours/ Furnace Cool/15 Ksi
2. Heat Treatment
Solution: 1177°C/4 hours/air cool
Age: 871 °C/8 hours/air cool
982 °C/4 hours/air cool
650°C/24 hours/air cool
760°C/8 hours/air cool

The alloy chemistries were determined using atomic adsorption and wet chemistry by Luvac, Inc. The chemistries and microstructures for the alloys are given in Table 3.3. The calculated γ' volume fraction for each alloy is also given in Table 3.3. (3.1) The concentration of trace elements which segregate to the grain boundaries such as B, Zr, C, O, P and S were determined. The grain size and prior powder particle size were determined via the linear intercept method. (98)

TABLE 3.3.

Alloy Chemistries and Microstructure

	Sample 1 Astroloy	Sample 2 Rene-95	Sample 3 Merl-76	Sample 4 IN-100
Chromium	14.8	14.0	12.2	12.2
Cobalt	16.3	7.71	17.8	18.3
Molybdenum	4.82	3.33	3.20	3.39
Columbium	.004	3.36	1.36	<.01
Aluminum	3.97	3.31	4.71	4.88
Titanium	3.39	2.41	4.19	4.17
Hafnium	.01	.01	.10	<.01
Vanadium	<.001	.007	.009	.97
Carbon	.044	.082	.034	.082
Boron	.025	.007	.020	.021
Zirconium	.037	.064	.050	.037
Oxygen	.0129	.0137	.0238	.0111
Sulfur	<.001	.001	<.001	<.001
Phosphorus	.014	<.001	<.001	<.001
Nitrogen	.0008	.0020	.0029	.0016
Silicon	.02	.07	.10	.04
Iron	.24	.18	.077	.082
Tungsten		3.42		
Nickel	Remainder	Remainder	Remainder	Remainder
γ' Volume Fraction (Calculated)	0.50	0.52	0.58	0.63
Grain Size (um)	28	25 and 24	11	23
Prior Powder Size (um)	95	70 and 34	22	35

3.1.2. Microstructural Characterization

Several samples of heat treated material were mounted in Buehler plastimet, ground on 240, 320, 400, and 600 grit silicon carbide paper, polished with 3 um diamond paste on nylon cloth, and finally polished with Nalcoag 1060 (colloidal silica solution) on nylon cloth. The specimens were etched using No. 2 stainless reagent (100 ml methanol, 50 ml HCl, and 5 gm $FeCl_3$).

The etched specimens were observed under both a Zeiss Universal optical microscope and an AMR-1000 A scanning electron microscope. Figures 3.1 - 3.4 show the after heat treatment microstructures of Astroloy, Merl-76, IN-100, and Rene-95 respectively. IN-100 and Astroloy have a coarse grain size with carbides decorating the grain boundaries. Merl-76 and Rene-95 have a finer grain size with large primary ' particles along the boundaries.

Prior powder boundaries were easily observed at low magnification in all the alloys tested. These boundaries usually coincide with grain boundaries. The prior powder boundaries result from the existence of large carbides on the surface of the powder particles. These carbides do not go into solution on subsequent heat treatment. In the case of Rene-95 and Merl-76 these carbides are known to be Columbium carbides, while in Astroloy and IN-100 they probably are Titanium carbides. (3.2) These carbides precipitate during solidification of the powder and segregate to the powder surfaces. The prior particle

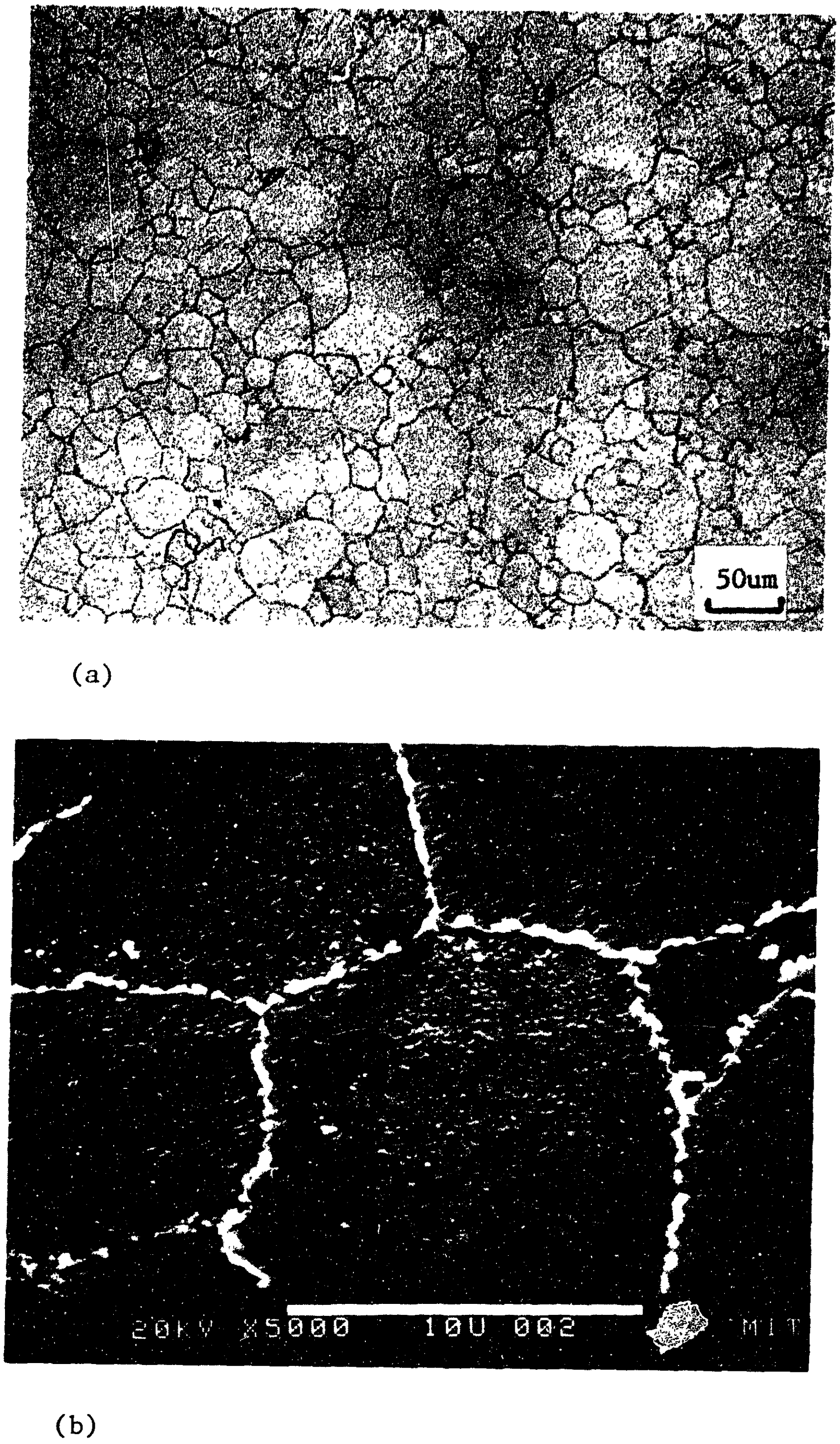

FIGURE 3.1) Photomicrographs of PM/HIP low carbon Astroloy. (a) optical, (b) SEM (etchant: 100ml Methanol, 50ml HCl, and 5g $FeCl_3$)

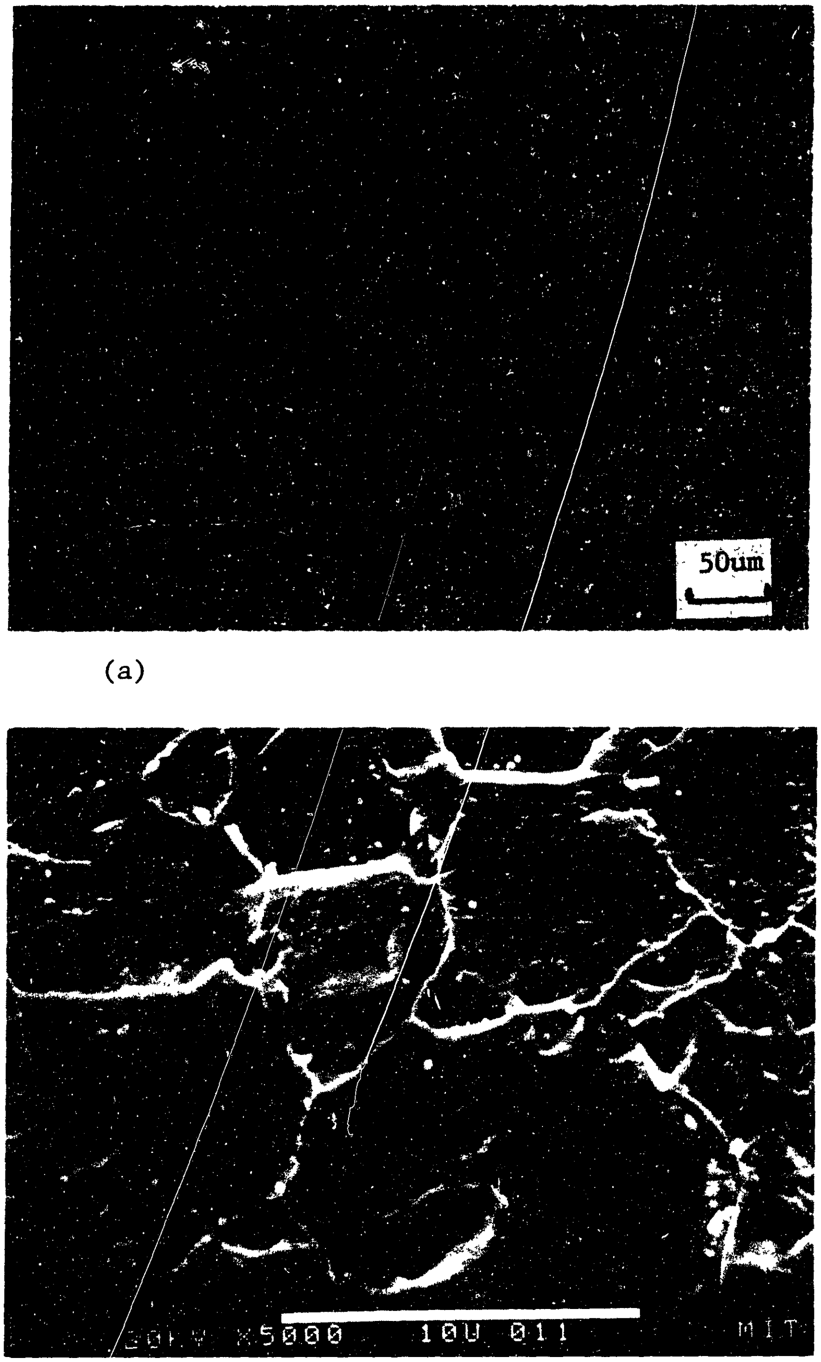

(a)

(b)

FIGURE 3.2) Photomicrographs of PM/HIP MERL-76. (a) optical (b) SEM (etchant: 100ml Methanol, 50ml HCl, and 5g $FeCl_3$)

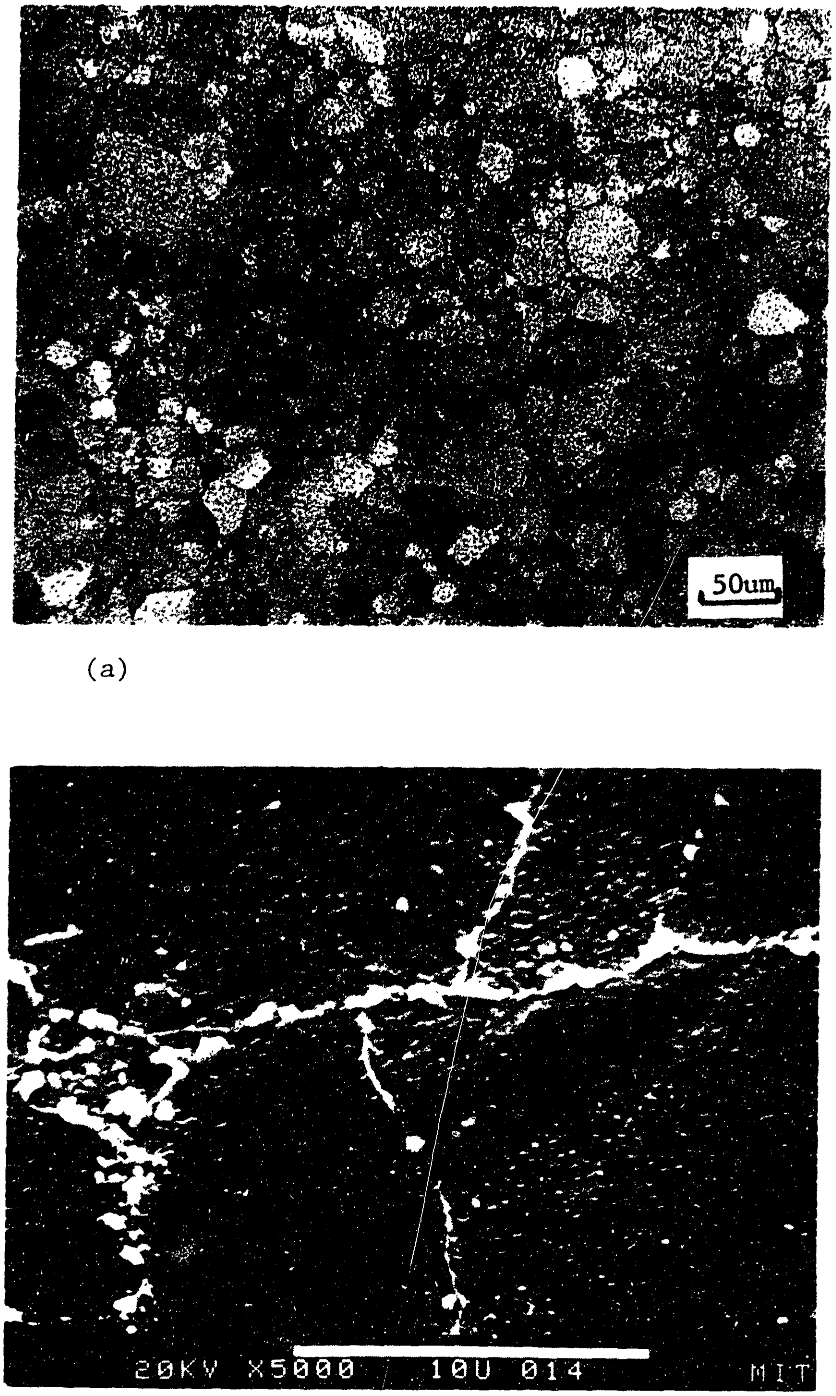

(a)

(b)

FIGURE 3.3) Photomicrographs of PM/HIP low carbon IN-100. (a) optical, (b) SEM. (etchant: 100 ml Methanol, 50 ml HCl, and 5 gm $FeCl_3$)

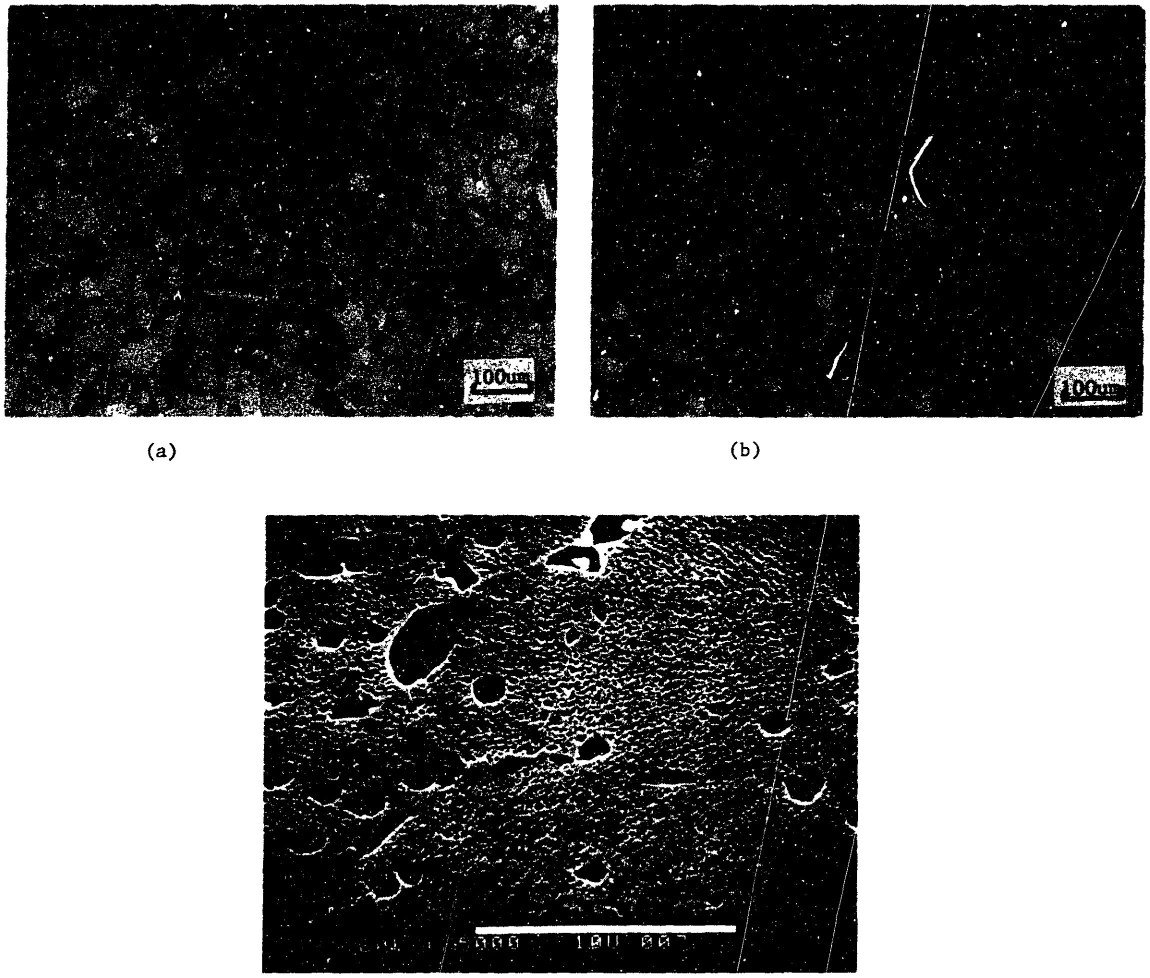

(a) (b)

(c)

FIGURE 3.4) Photomicrographs of PM/HIP RENE-95. (a) optical (60 Mesh), (b) optical (120 mesh), (c) SEM. (etchant: 100ml Methanol, 50ml HCl, and 5g $FeCl_3$)

boundaries have a higher concentration of carbides than grain boundaries which are not along the prior powder particle boundaries.

3.2. Mechanical Testing

Different mechanical tests were performed to determine the high temperature tensile, creep, and creep crack growth behavior of the alloys. The test procedures are described in the following sections.

3.2.1. Tensile Testing

Tensile tests were performed using a screw driven floor mounted Instron Tensile Tester. The tests were run at 704°C and a crosshead displacement rate of .02 inches per minute. An A.T.S. three-zone resistance heater with a Leeds and Northrup Electromax III temperature controller were used for specimen heating. Load vs. Displacement was recorded using a strip chart recorder incorporated in the Instron machine. The .2% yield stress and ultimate tensile strength were measured graphically. Elongation and reduction of area were measured directly off the failed test specimen. Figure 3.5 illustrates the specimen geometry used in both tensile and creep-rupture tests.

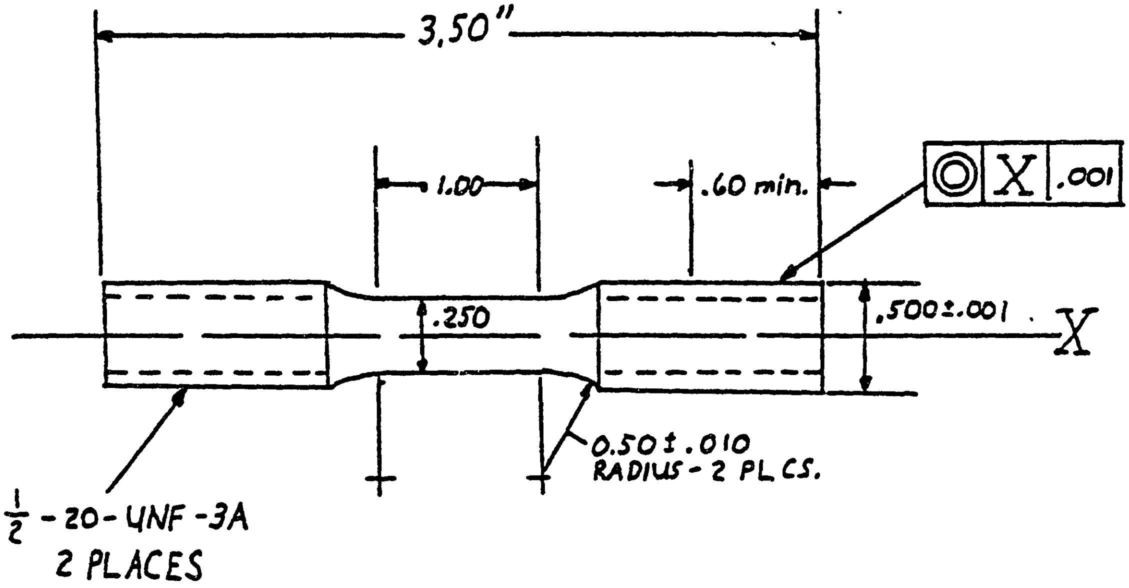

FIGURE 3.5) Smooth bar creep-rupture and tensile specimen geometry. (Dimensions in inches)

3.2.2. Smooth Bar Creep Testing

Creep tests were conducted to obtain the power law creep constitutive equations for the purpose of theoretical modeling of creep crack growth, and to determine the creep-rupture properties of the alloys. Creep tests were conducted at 704°C within stress range of 600 to 1200 MPa. The test temperature was accurate to within ±4°C. The elongation was measured using an extensometer connected to a dc-dc LVDT with a .25 inch range per 100 mV, and a resolution of 1 micron. Tests were conducted on an A.T.S. level arm tester. The minimum creep rate was recorded for several stress levels. The stress was increased in steps in order to obtain several stress versus minimum creep rate data points per specimen. Smooth bars were tested at a constant load and the time to rupture was recorded as well as the minimum creep rate.

3.2.3. Notched Stress Rupture Testing

Circumferentially notched specimens were used for NSR testing. (Figure 3.6.) The notch has 60° flank angles, a root radius of .33 mm, and a calculated elastic stress concentration factor of 3.2. Tests were conducted at 704°C in air in an A.T.S. level arm test system with a 3-zone resistance heater. The time to rupture for each test was recorded. The tests were performed in a range of stress from 400 MPa to 800 MPa. Several specimens of PM/HIP Rene-95

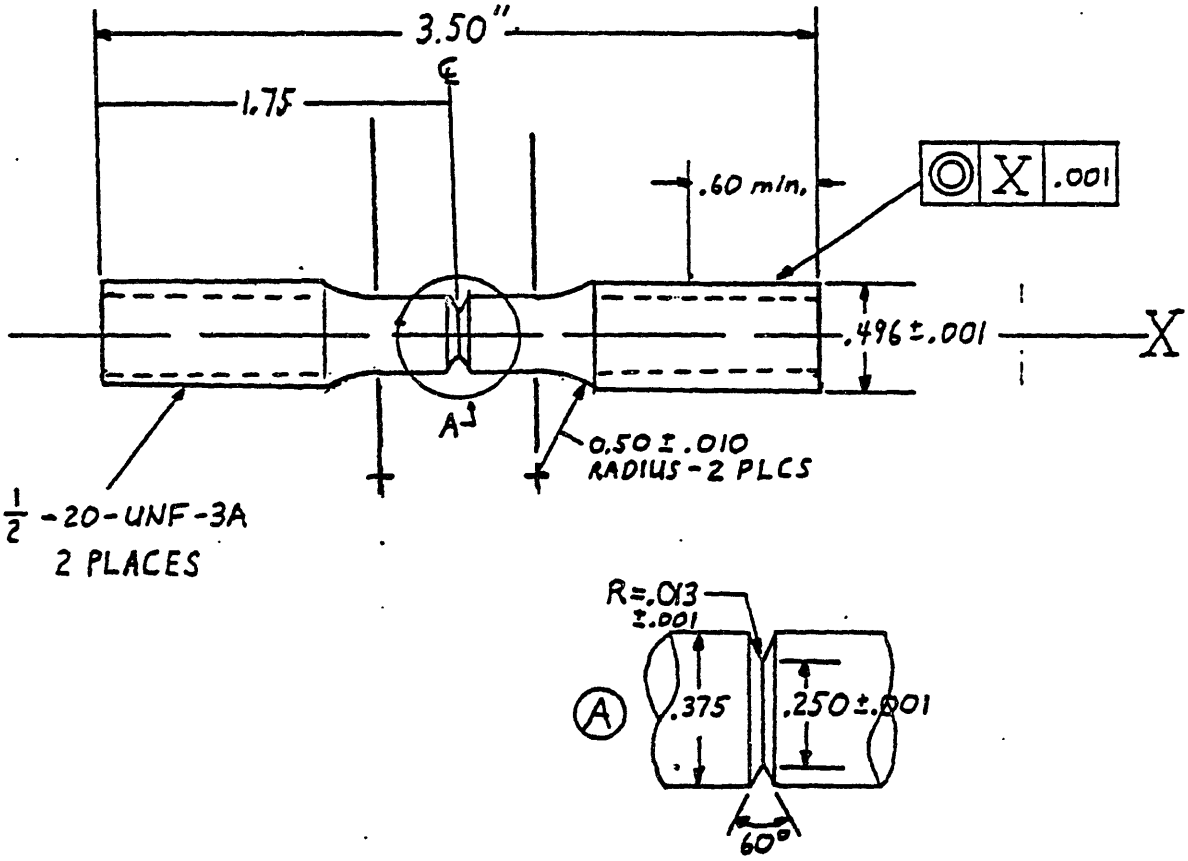

FIGURE 3.6) Notched Stress-Rupture (NSR) specimen geometry. (Dimensions in inches)

were pre-exposed to air at 704°C to determine the effect of oxygen on the notched stress rupture (NSR) behavior.

3.2.4. Creep Crack Growth Rate Testing

Creep crack growth rate tests were conducted at 704° C with a constant applied load in a level arm tester supplied by Applied Testing System Company (ATS). The temperature was controlled within ± 4°C in the gauge section of the specimen using a 3-zone resistance heater. Tests were conducted in two environments: air and 99.999 percent pure argon. A retort supplied by ATS was used in the argon tests. Argon tests were conducted at a pressure of 5 psig in order to insure no back streaming of air.

A single edge-notched test specimen was used in the creep crack growth rate tests. (Figure 3.7) The specimen has side grooves added to prevent crack tip tunnelling. Tunnelling of the crack results from the slower creep crack growth rate in the plane stress condition which would exist on the specimen surface without side grooves.

A starter notch is cut using a 150 um thick diamond saw. Specimens were fatigue precracked at room temperature. The maximum stress intensity, K, used in precracking was always less than the initial stress intensity in subsequent creep crack growth testing at 704°C.

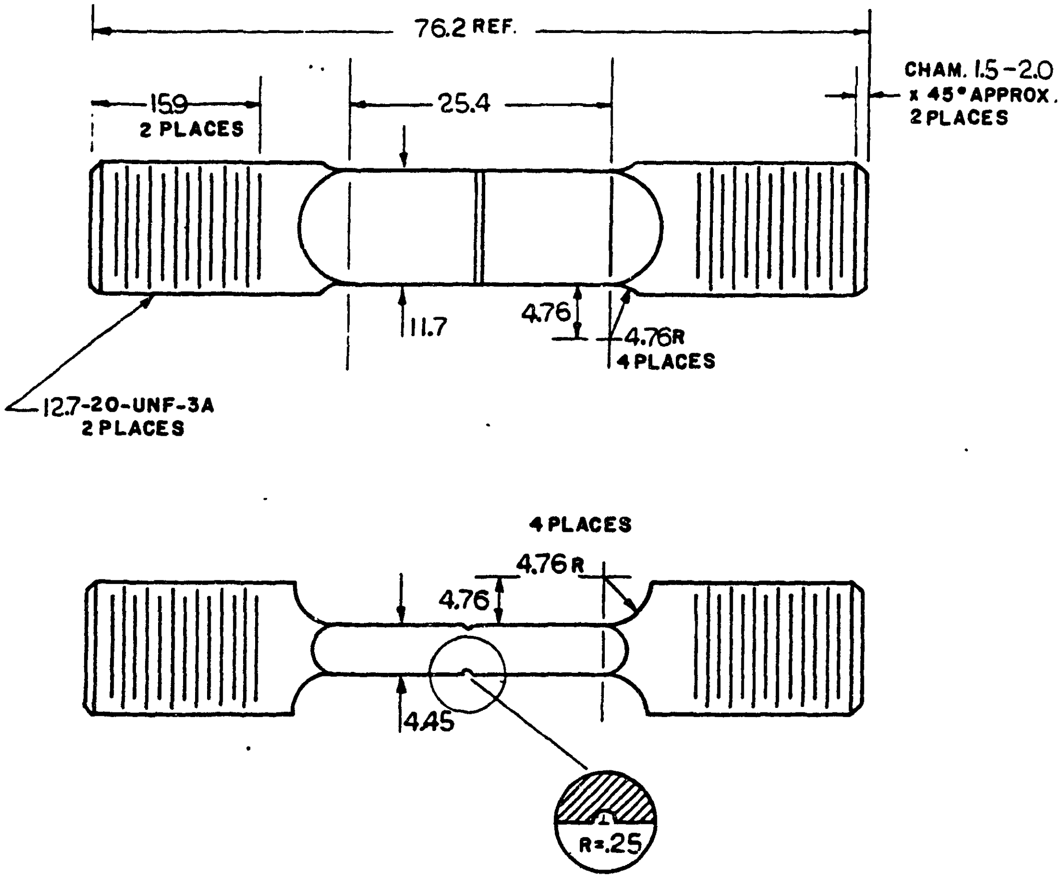

FIGURE 3.7) Single Edge Notched (SEN) specimen geometry used in CCGR tests. (Dimensions in mm)

3.2.4.1. D.C. Potential Drop Technique

The d.c. electrical potential drop method is based on the fact that in a current carrying body, a discontinuity such as a crack, results in a disturbance in the potential field. In order to monitor the crack length, a current is passed through the specimen and the electrical potential across the crack mouth is measured. An increase in crack length causes the potential between two fixed points on either side of the crack to increase. By continuously monitoring this potential increase and comparing it to a reference potential (V_o), the crack length to specimen width ratio (a/w) can be inferred.

Several theoretical solutions for crack length versus potential have been made by solving Laplace's equation. A solution by Johnson (88) developed for a center-cracked plate specimen with a razor slit starter is as follows:

$$\frac{V}{V_o} = \frac{\cosh^{-1}\left\{\dfrac{\cosh(\pi Y/W)}{\cos(\pi a/W)}\right\}}{\cosh^{-1}\left\{\dfrac{\cosh(\pi Y/W)}{\cos(\pi a_o/W)}\right\}} \qquad \text{(Equ. 3.1)}$$

Johnson later worked out a similar solution for a SEN specimen with a razor sharp slit starter notch (89):

$$\frac{V}{V_o} = \frac{\cosh^{-1}\left[\dfrac{\cosh(\pi Y/2W)}{\cos(\pi a/2W)}\right]}{\cosh^{-1}\left[\dfrac{\cosh(\pi Y/2W)}{\cos(\pi a_o/2W)}\right]} \qquad \text{(Equ. 3.2)}$$

In both equations V is the measured potential, V_o is the measured potential for a crack of length a_o, Y is one half the distance between the two potential measurement leads, 'a' is the crack length (for the center-cracked specimen the crack length and reference crack length are 2a and $2a_o$ respectively), and W is the specimen width.

Other theoretical calibrations have been performed by Che-Yu Li and Wei (93) who modified Johnson's relations for an elliptical starter notch. Recent work has been performed on modeling the potential distributions using finite element techniques (94). The finite element solutions verify equation 3.2 by Johnson.

The theoretical calibration by Johnson (89) has been shown to be valid for the SEN specimen geometry in several experimental calibrations (63, 90-92, 94). Figure 3.8 shows the results of a theoretical and an experimental calibration for the SEN specimen shown in Figure 3.7. The calibration was accomplished by growing a fatigue crack at room temperature while monitoring the potential. The crack length was measured by periodically altering the R-ratio to beach

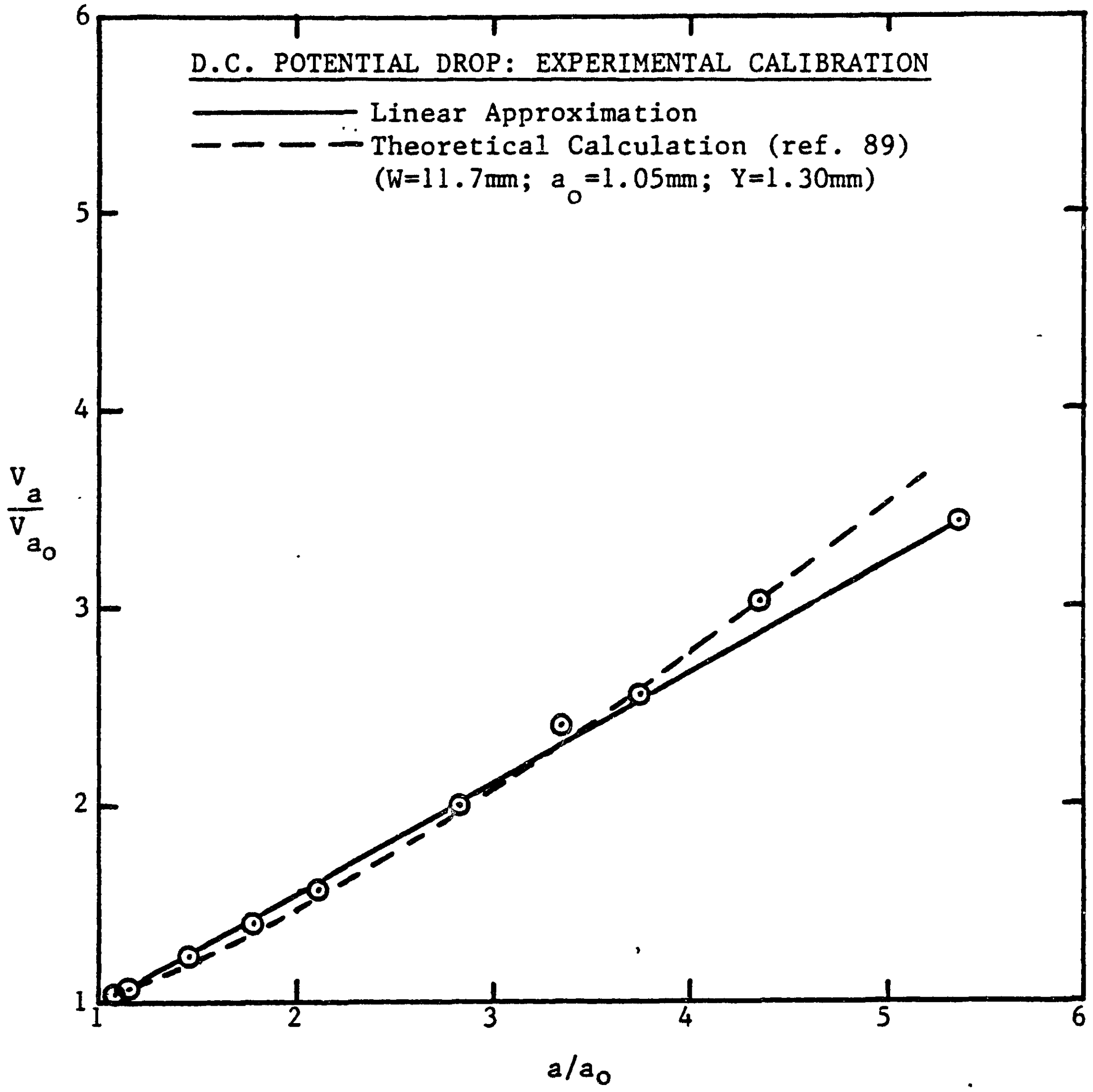

FIGURE 3.8) Experimental calibration of the d.c. potential drop technique for crack length measurement for the SEN specimen shown in figure 3.7.

mark the fracture surface. Agreement between the actual data and the theoretical calculation were obtained.

Figure 3.9. shows a schematic for the test system used in creep crack growth testing. All of the equipment used was off-the-shelf and did not have to be specifically manufactured.

There exists several sources of potential errors in this method of crack length measurement from both electrical and configurational sources.

A source of electrical error which is possible comes from the DC power supply used as a constant current source. A Hewlett- Packard Regulated DC Power Supply Model 6295B was used in this study.

Possible errors are:

1.) Current Drift -The current output can drift by .05% in an 8 hour period at constant temperature.

2.) Temperature Variation -Ambient temperature variation can cause a variation of .012%/°C in a range from 20 to 40°C.

3.) AC Line Variation -Variation in AC line current can cause .012% variation in DC output current.

4.) Ripple -Background current fluctuations of .05% peak to peak are possible with system.

5.) Insufficient Warm Up Time -Significant variation in output current and voltages can occur if the power source is not allowed a 30-minute warmup.

6.) Plotter Accuracy -The Omega plotter has an accuracy of .5% of full scale. With a typical full scale of 10mV the error becomes 50 μV.

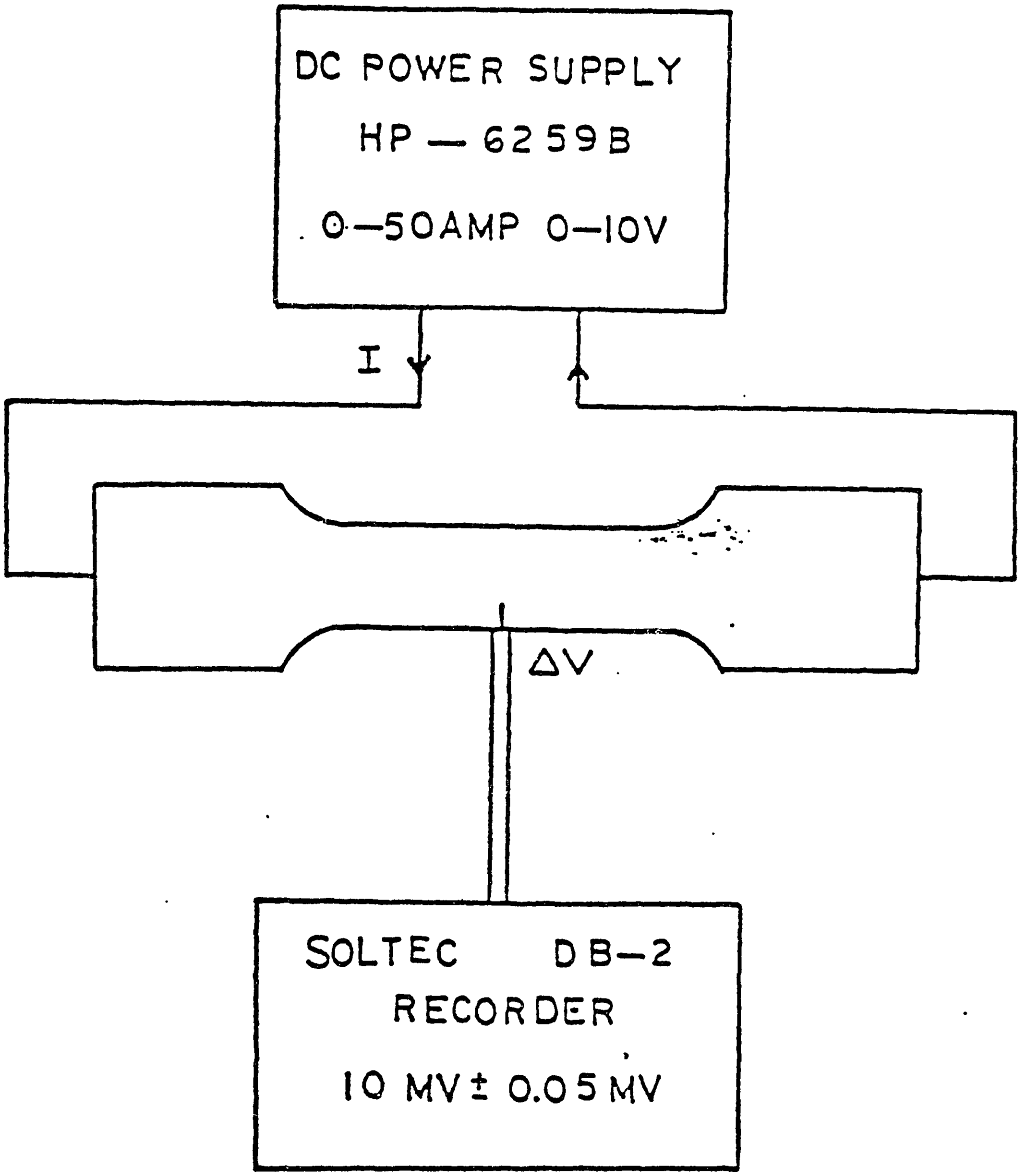

FIGURE 3.9) Schematic of the d.c. potential drop system for crack length measurement.

In a 24-hour time period with a 10°C variation in temperature, a .33% maximum variation in output current is possible. This variation is small and not detectable with the recorder used in the study. Using the calibration curve in Figure 3.8 and assuming an initial voltage of 2 mV yields a minimum resolution of 60 microns change in crack length.

Analysis of potential sources of error has been performed by several researchers (90-92, 95). The sources of error include temperature variation, electrical variations, and geometry variations. Electrical and temperature variation have been calculated to cause a limit of 100 um in crack length resolution for a compact tension specimen (95). Configurational variations such as lead position can cause extreme errors and should be tightly controlled.

The d.c. potential difference method requires careful positioning of both current-input leads and potential measurement leads. The lead positioning will affect the sensitivity and precision.

The current leads should be positioned at a distance of at least 2w from the crack plane (90). Closer positioning of the leads increases the sensitivity, but reduces reproducibility and therefore should only be used when increased sensitivity is demanded. The specimen must be insulated from the loading frame in order to force the current to pass only through the specimen. The current lead wires should be large enough to conduct up to 50 amps d.c. current.

The potential measurement leads should be placed as close as possible and across the mouth of the crack. This positioning has been shown to give the best reproducibility while maintaining sensitivity (90). The contact area of the potential lead wires should be small, and wires on the order of .2 mm in diameter are usually used.

Attachment of the potential measurement leads is accomplished by electrical discharge welding to the specimen. These welds should be strong enough to endure the high temperature and oxidizing environment experienced during creep crack growth rate testing. The current input leads in several studies have been attached outside the heating furnace and passing the current through the specimen grips thus eliminating some problems of attachment.

The calculated value for crack length given by equation 3.2 will vary significantly with the potential lead spacing 'Y'. The variation in the theoretical calibration is shown in Figure 3.10. for three values of Y which represent a lower limit, upper limit, and nominal spacing.

Configuration errors can be eliminated by stopping the test before failure and breaking the specimen at room temperature in fatigue. An accurate measurement of the final crack length can be obtained from the fracture surface. This along with the potential measurement at test termination will give a point with which to calibrate the

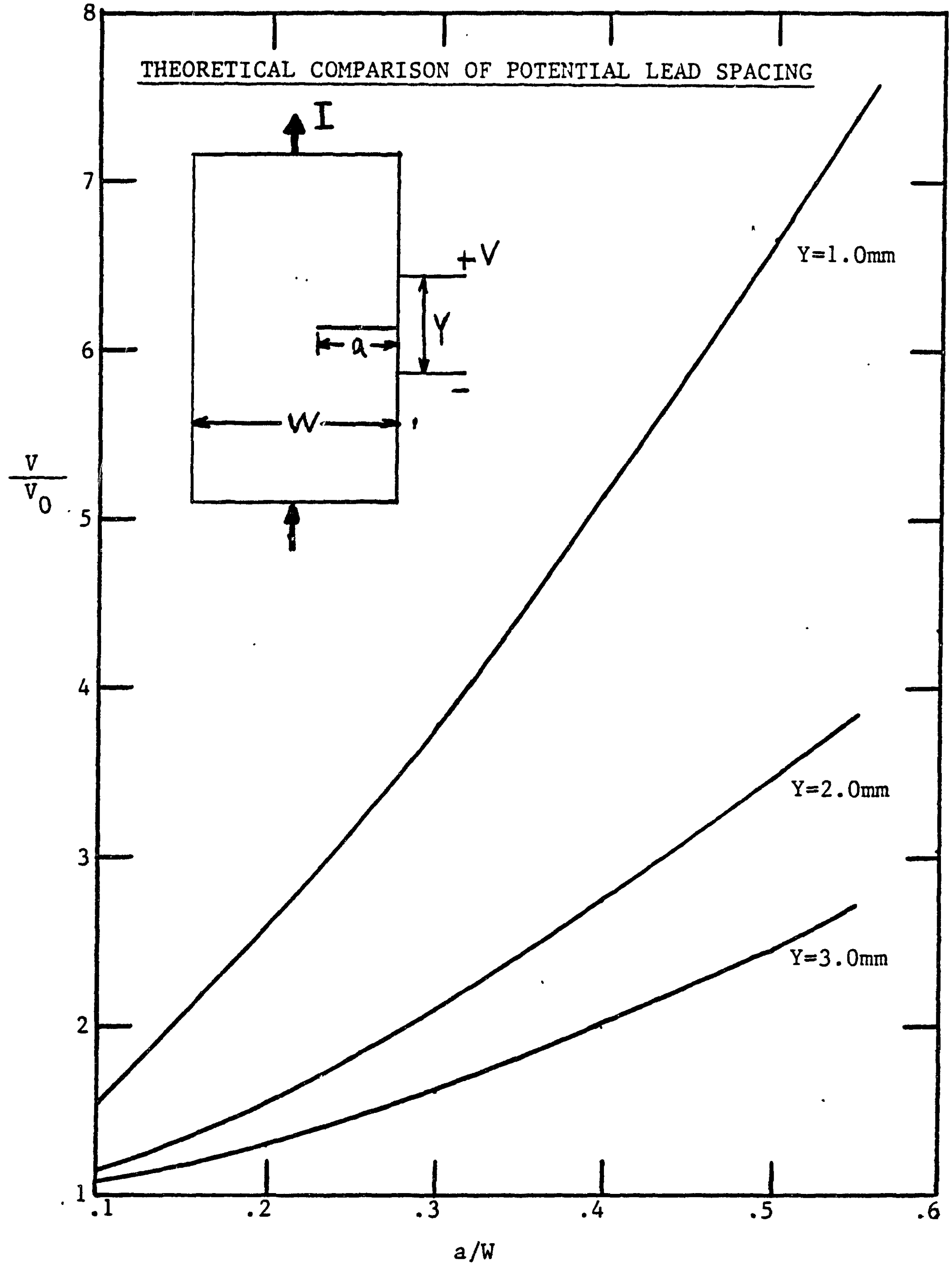

FIGURE 3.10) Comparison of the effect of potential measurement lead spacing, Y, on the potential versus crack length curve. SEN specimen geometry. (equation 3.2)

test. The final and initial crack lengths and potentials are used to calculate the lead spacing Y. This procedure eliminates the major source of configurational error in crack length measurement.

The effect of crack tip bowing on the d.c. potential drop technique has been analyzed by Druce and Booth (92) who indicate a significant under-prediction of crack length for short cracks if a straight crack front is assumed. The addition of side grooves on SEN specimens by several researchers (39, 63) eliminates the plane stress condition at the specimen surface and reduces crack tip bowing.

3.2.4.2. Data Analysis

The crack length versus time data is calculated from the potential versus time results. The conversion from potential, V, to crack length, 'a', is given by solving equation 3.2. for crack length:

$$a = \left(\frac{2W}{\pi}\right) \cos^{-1}\left(\frac{\cosh(\pi Y/2W)}{\cosh\left[\left(\frac{V}{V_o}\right) \cosh^{-1}\left(\frac{\cosh(\pi Y/2W)}{\cos(\pi a_o/2W)}\right)\right]}\right) \qquad \text{(Equ. 3.3)}$$

The crack growth rate is calculated by determining the slope of a least squares fit to 3 data points. The data points must span .2 mV in measured potential (which is 4 times the limit of resolution).

The stress intensity factor, K, for the SEN specimen is given by Brown and Strawly (96):

$$K_I = \sigma\sqrt{\pi a}\ (1.12-.23(a/w)+10.6(a/w)^2-21.7(a/w)^3 +30.4(a/w)^4) \qquad \text{(Equ. 3.4)}$$

where K is the stress intensity factor, σ is the gross section stress in MPa, 'a' is the crack length, and w is the width of the specimen. This equation is for a single edge notched specimen (SEN) which is free to bend. The gross section stress for a notched specimen is given as:

$$\sigma = \frac{P}{W\sqrt{B*B_N}} \qquad \text{(Equ. 3.5)}$$

where P is the applied load, B is the gross thickness, and B_N is the net section thickness (97).

3.3 Pre-exposure Oxygen Penetration Tests

One SEN specimen (figure 3.7) of each material was exposed to air at 704°C for 100 hours with no applied load in order to allow oxygen to diffuse into the material. The bars were notched using a 150 um thick diamond saw, and fatigue-precracked at room temperature before the high temperature exposure. The bars were pulled to failure in an Instron screw driven tensile tester at 704°C with extension rate of .2 inches/minute.

The depth of inter-granular fracture is measured. The intergranular fracture is a result of oxygen embrittlement of the alloys (30). An apparent diffusivity of oxygen is calculated using the following equation:

$$D= X^2/t \qquad \text{(Equ. 3.6)}$$

where x is the depth of intergranular fracture, t is the exposure time (3.6 x 10 seconds), and D is the apparent diffusivity of oxygen along the grain boundary (30).

3.4. Fractography

The fractography was performed using an AMR-1000 scanning electron microscrope. The specimens were cleaned with acetone and coated with gold to avoid charging of oxidized surfaces.

4. EXPERIMENTAL RESULTS

4.1. Tensile Properties at 704°C

The tensile test results at 704 °C are shown in Table 4.1. The 0.2% yield strength, Elastic modulas, and U.T.S. measured for all the alloys are approximately the same. The total elongation varies by a factor of three from 5.0% for Rene-95 to 15.4% for Astroloy. The specimens with low ductility exhibited failure via the propagation of surface cracks. The plastic strain hardening exponent N_p and proportionality constant B_p are also given in Table 4.1. $(\varepsilon_p = (\sigma / B_p)^{N_p})$.

TABLE 4.1.

704°C Tensile Test Results

	U.T.S. (MPa)	.2% Y.S. (MPa)	% El.	E (GPa)	Bp (MPa)	Np
Rene-95	1199	947	5.0	167	1785	8.93
IN-100	1167	1012	8.4	162	1454	16.39
MERL-76	1164	1012	13.1	160	1448	16.67
Astroloy	1200	950	15.4	170	1662	9.71

4.2. Smooth Bar Creep Results

4.2.1. Minimum Creep Rate Results

The minimum creep rate for each alloy was measured in air at 704°C in a range of applied stress from 600 to 1200 MPa. The results are given in Figure 4.1 as a plot of stress versus minimum creep rate. The creep exponents, Nc, and constants, Bc, for the power law equation for secondary creep rate are given in Table 4.2. The minimum creep rates range from 10^{-8} sec^{-1} to 10^{-4} sec^{-1}. The creep behavior of all four alloys measured is similar. Rene-95 has a larger creep exponent (Nc) and proportionality constant (Bc) than the other alloys.

TABLE 4.2.

Minimum Creep Rate Results at 704°C

$$\dot{\varepsilon}c(\text{sec}^{-1}) = Bc(\sigma\,(\text{MPa}))^{N_c}$$

	Bc	Nc
Astroloy	6.29×10^{-61}	18.5
Merl-76	1.66×10^{-65}	20.0
IN-100	7.81×10^{-61}	18.5
Rene-95 (60 mesh)	4.03×10^{-37}	10.3

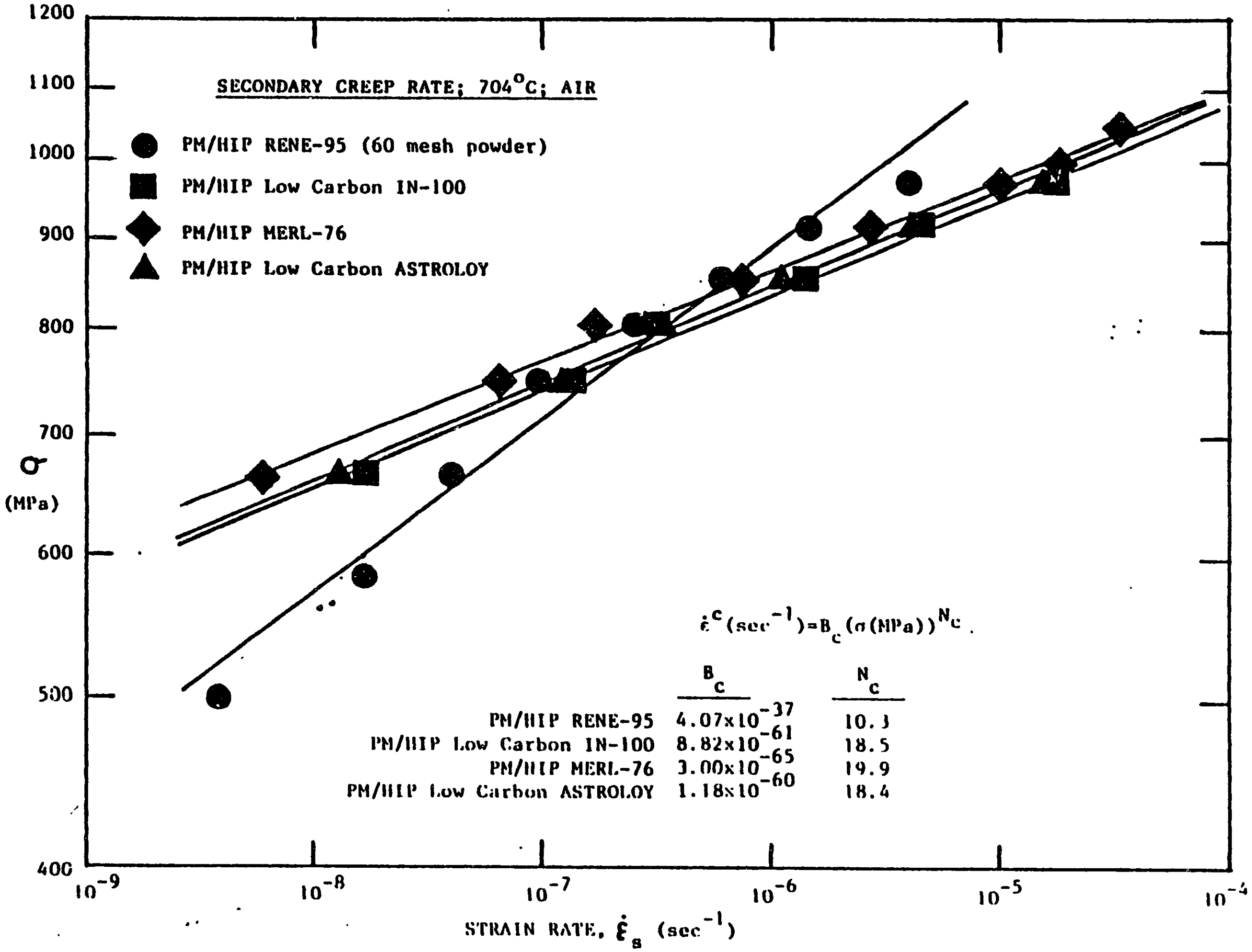

FIGURE 4.1) Secondary creep rate results for four PM/HIP Nickel-Base Superalloys at 704°C.

4.2.2. Creep Rupture Results

Four creep-rupture tests (one from each alloy) were performed at 800 MPa in air at 704°C. The results for the four alloys were similar with the exception of Merl-76 which gave a longer time to rupture. The individual results are shown below:

Table 4.3.

Creep-Rupture Results, Air, 704°C, 800 MPa

	t (hrs)	$\varepsilon_{critical}$
Rene-95	7.2	.0083
IN-100	4.7	.0068
Merl-76	28.7	.0202
Astroloy	5.8	.0068

Table 4.3. also shows the secondary creep strain at failure. The secondary creep strain is the product of the minimum creep rate and the time to rupture. This value is constant for an alloy at a given stress, which is the basis for the well known Larson-Miller parameter used to correlate creep-rupture results.

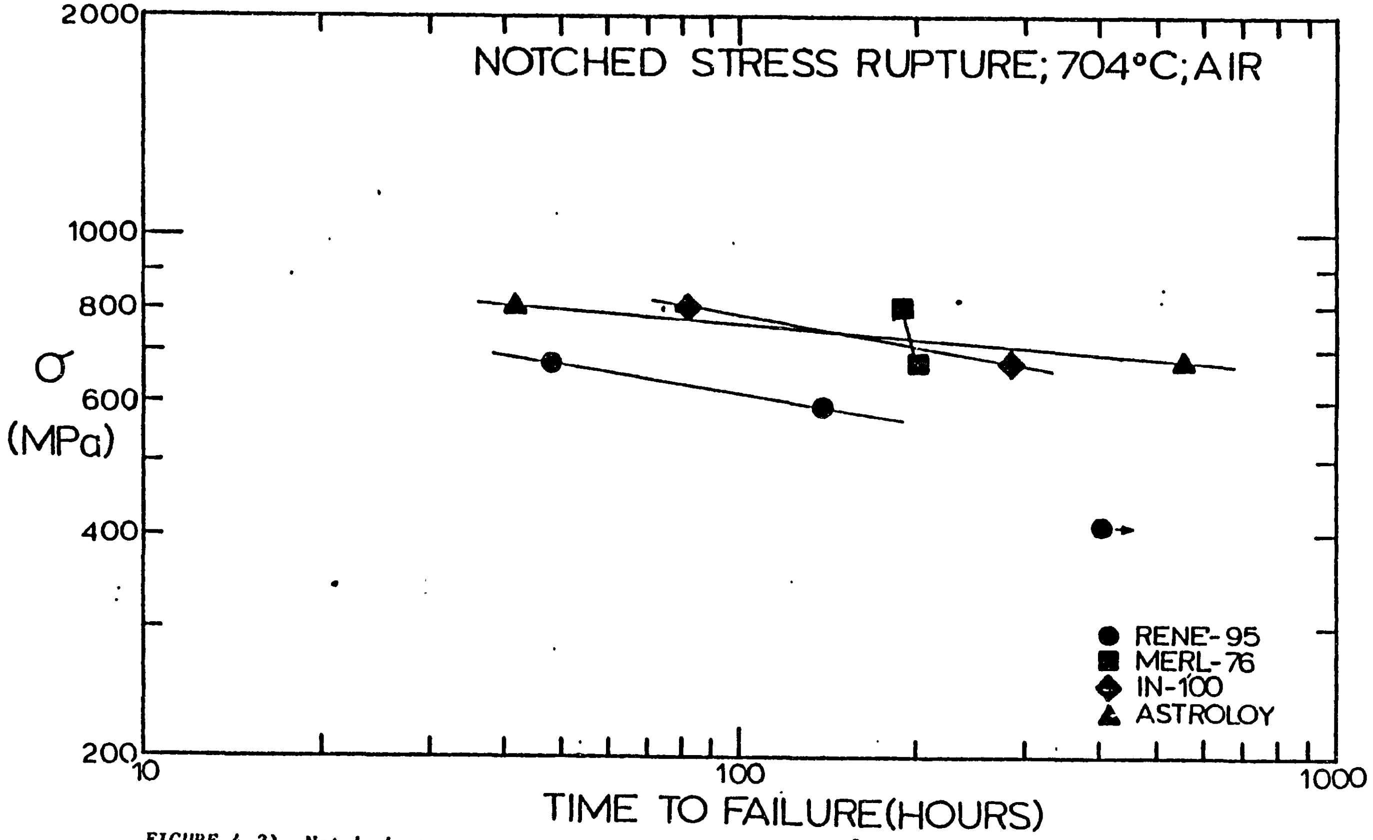

FIGURE 4.2) Notched stress rupture results in air at 704°C for four PM/HIP Nickel-Base Superalloys.

4.3. Notched Stress Rupture Results

4.3.1. Constant Load Results

Notched stress rupture (NSR) tests were performed on all four alloys in air at 704 °C. The results are given in Figure 4.2. The results indicate that Rene-95 has a shorter rupture time than the other three alloys tested. At high stress Merl-76 gave the longest time to rupture, but at the lower stress a crossover occurs and Astroloy has the longest time to rupture.

The NSR results can be interpreted as giving a measure of the relative CCGR behavior of the four alloys when tested in air. Astroloy had the longest time to rupture at the lower stress, but at the higher stress Astroloy fails sooner than IN-100 and Merl-76.

4.3.2. Air Pre-Exposure Results

Three Rene-95 specimens were exposed to air at 704° C for 100 hours prior to NSR testing. Some specimens had a small applied load during the pre-exposure. They were then run to failure at a higher stress in air at 704°C. The results are summarized in Table 4.4.

TABLE 4.4.

Notched Stress-Rupture of Rene-95, 704°C

Pre-exposure	Test Results
408 MPa/403.4 hrs.	675 MPa/<1 min.
No Pre-exposure	591 MPa/137.2 hrs.
0 MPa/73.4 hrs.	591 MPa/237.8 hrs.
338 MPa/69.0 hrs.	571 MPa/153.8 hrs.

The tests were inconclusive but they did present a few interesting results: 1) pre-exposure in air with a small tensile stress was more damaging than a pre-exposure to air with no stress; and 2) a long pre-exposure with a small stress exhausted the residual life at the higher load.

4.4. Creep Crack Growth Rate Results

4.4.1. CCGR for Five·Ni-Base Alloys

The creep crack growth rates were measured at 704°C in air and in 99.999% pure argon on all five alloys. The alloys tested were all in the PM/HIP condition. They were low carbon Astroloy, Merl-76, low carbon IN-100, Rene-95 (60 mesh), and Rene-95 (120 mesh).

The creep cracks could not be made to grow if the maximum K used in pre-cracking the specimen was higher than the initial K for CCGR testing. The lack ofcreep crack growth is probably due to the presence of residual compressive stresses imposed by the larger plastic zone remaining from the fatigue precracking.

4.4.1.1. CCGR of PM/HIP low C Astroloy

The results of 6 CCGR tests on PM/HIP low C Astroloy are shown in Figure 4.3. Four tests were performed in air and exhibited an increasing da/dt versus K, but the CCGR curve was not linear over the entire range of K tested. A three stage creep crack growth curve was obtained. The lowest initial K in air was 22 MPa $\sqrt{m}$, and the lowest initial K in argon was 33.2 MPa $\sqrt{m}$.

The tests had an initially large rise in CCGR followed by a region of decreasing slope. The slope in the second region was approximately 3.5 in air and 7.0 in argon.

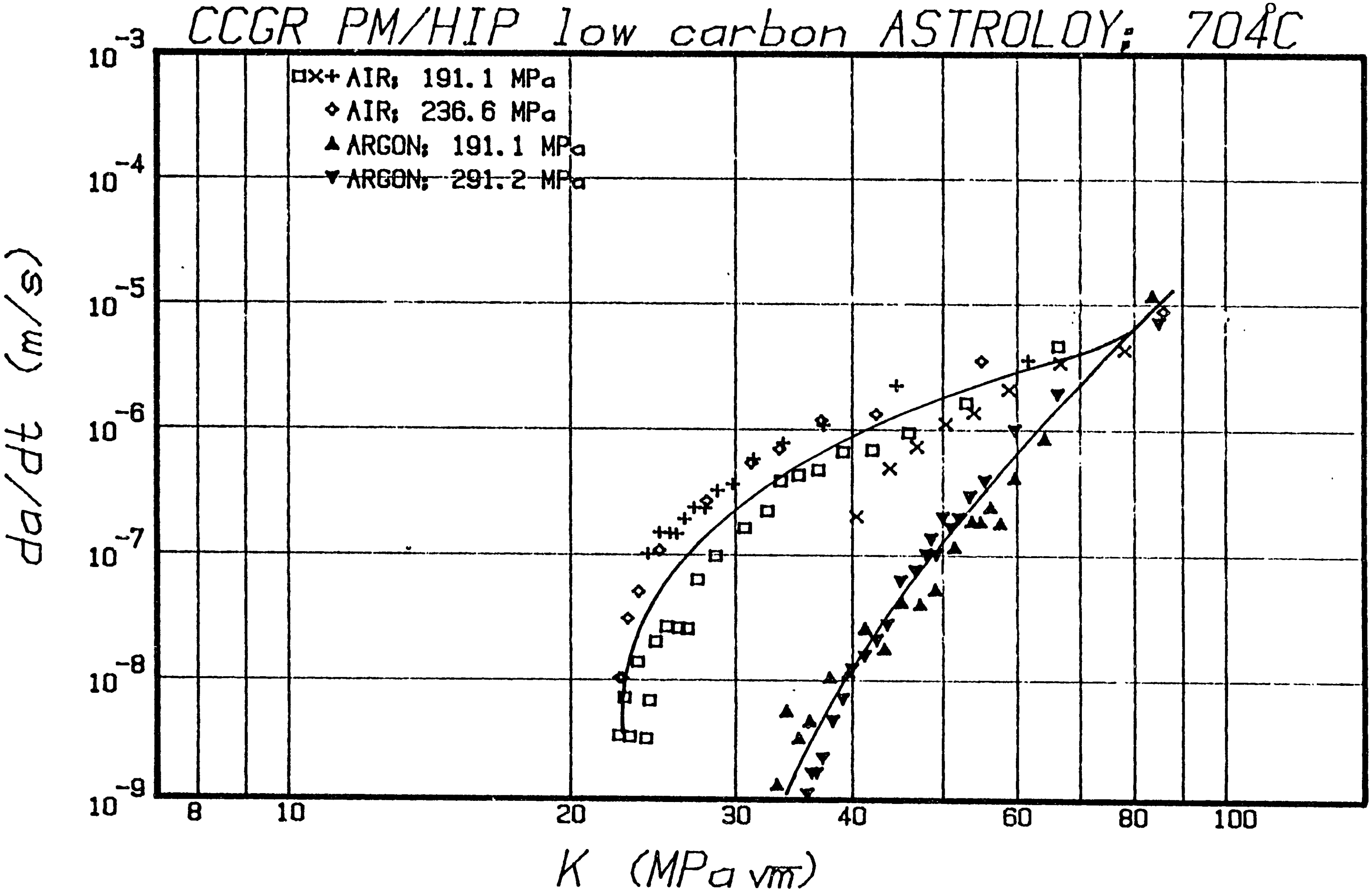

FIGURE 4.3) CCGR results for PM/HIP low carbon ASTROLOY at 704°C in both air and in 99.999% pure argon.

The CCGR in air is 100 times faster in air than in argon at K = 40 MPa$\sqrt{m}$, but for K = 70 MPa$\sqrt{m}$ the air and argon CCGR curves are the same at 3.5 x 10^{-6} m/s. The two curves merge at high crack growth rate indicating that the crack front was advancing faster by creep fracture with no effect of oxygen embrittlement.

4.4.1.2. CCGR of PM/HIP Merl-76

Four CCGR curves in air and two CCGR curves in argon at 704°C were obtained. (Figure 4.4) The results in air were for gross section stress from 145.6 MPa to 655.0 MPa, and an initial crack length from 1.01 mm to 2.62 mm. The CCGR results in air increased 20 times over the CCGR in argon at K = 40 MPa$\sqrt{m}$. The behavior in air and in argon are similar to Astroloy. All the tests have an initially fast increase in the CCGR followed by a region of linearly increasing CCGR on a log-log plot. The slope of the air CCGR versus K curves are approximately 3, and the CCGR tests in argon had a slope of 4.

A definite rise in the CCGR measured in air was observed before failure at K = 80 MPa$\sqrt{m}$, while in an argon atmosphere the final K was approximately 110 MPa$\sqrt{m}$.

The CCGR measured in air away from the initial transient was slightly higher in specimens which had a lower gross section stress. This effect is probably due to the change in dK/da with gross stress in the specimen. This result will be discussed later.

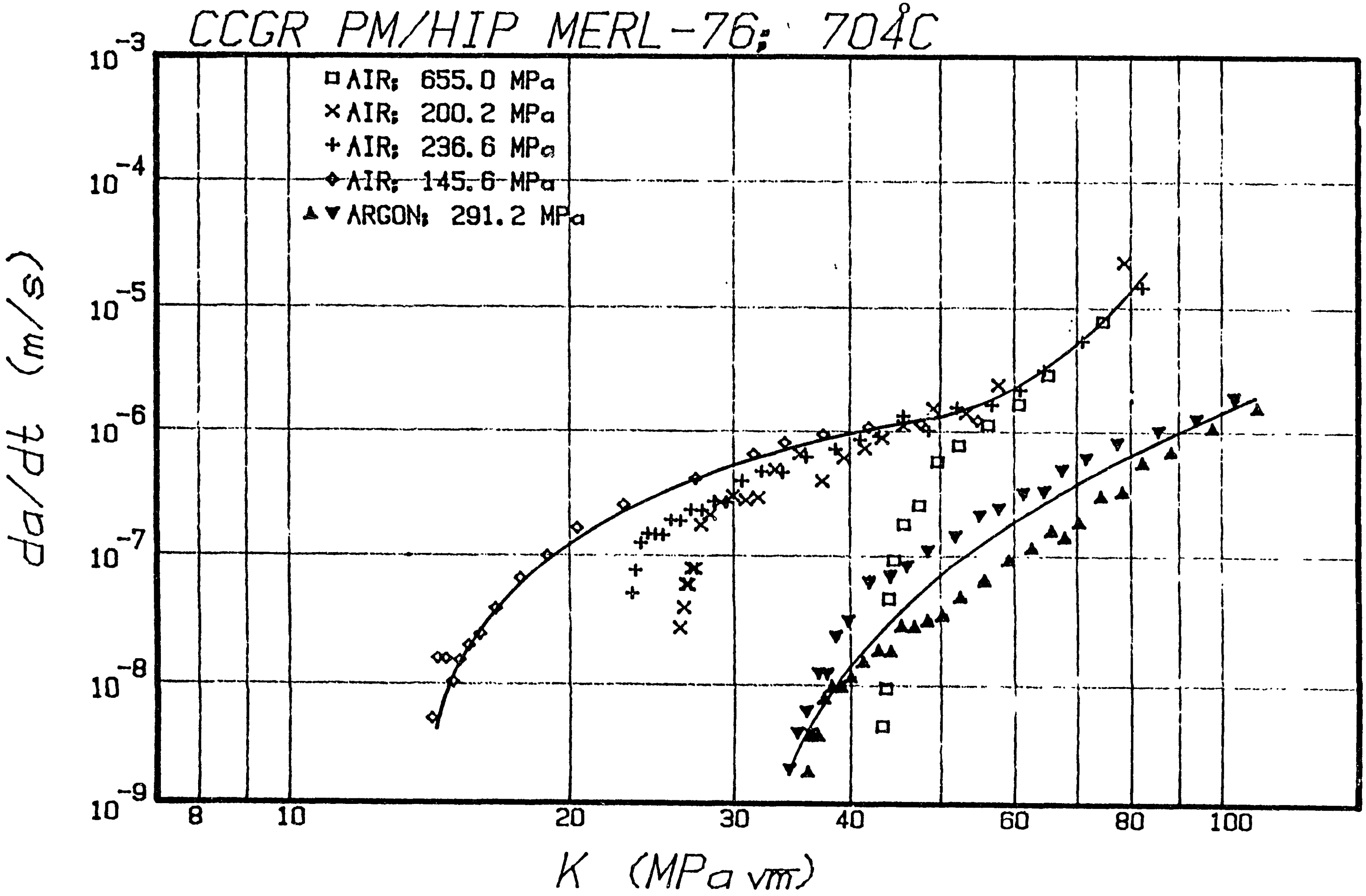

FIGURE 4.4) CCGR results for PM/HIP MERL-76 at 704°C in both air and 99.999% pure argon.

4.4.1.3. CCGR of PM/HIP Low C IN-100

The CCGR for PM/HIP Low C IN-100 at 704°C is shown in Figure 4.5. Both air and high purity argon CCGR results are given. The CCGR in air increased to 4 times the CCGR in argon at K = 40 MPa $\sqrt{m}$. The apparent K_{IC} for IN-100 in both air and argon was 100 MP$\sqrt{m}$.

The effect of dK/da on the CCGR in an argon atmosphere is easily observed. The higher the gross section stress the lower the CCGR for the same stress intensity factor, K.

4.4.1.4. CCGR of PM/HIP Rene-95 (60 Mesh)

Rene-95 (60 mesh) showed the largest effect of environment on the creep crack growth behavior. (Figure 4.6) The CCGR in air was 300 times higher than the CCGR measured in argon. K_{IC} at 704°C was observed to occur at 80 MPa$\sqrt{m}$.

CCGR tests in air were performed over a range of gross section stresses from 91 MPa to 291 MPa, and a range of initial crack lengths from 1.40 mm to 3.35 mm. The results of the air tests were similar, but the effect of gross stress on the Stage II CCGR was observed in this alloy as in all the previous alloys tested.

The CCGR results indicate similar initial CCGR behavior. The crack growth rates were initially very low and increased rapidly with crack advance. This sharp rise in CCGR was followed by a region of gradually increasing CCGR over a broad range of K. The slope of the CCGR versus

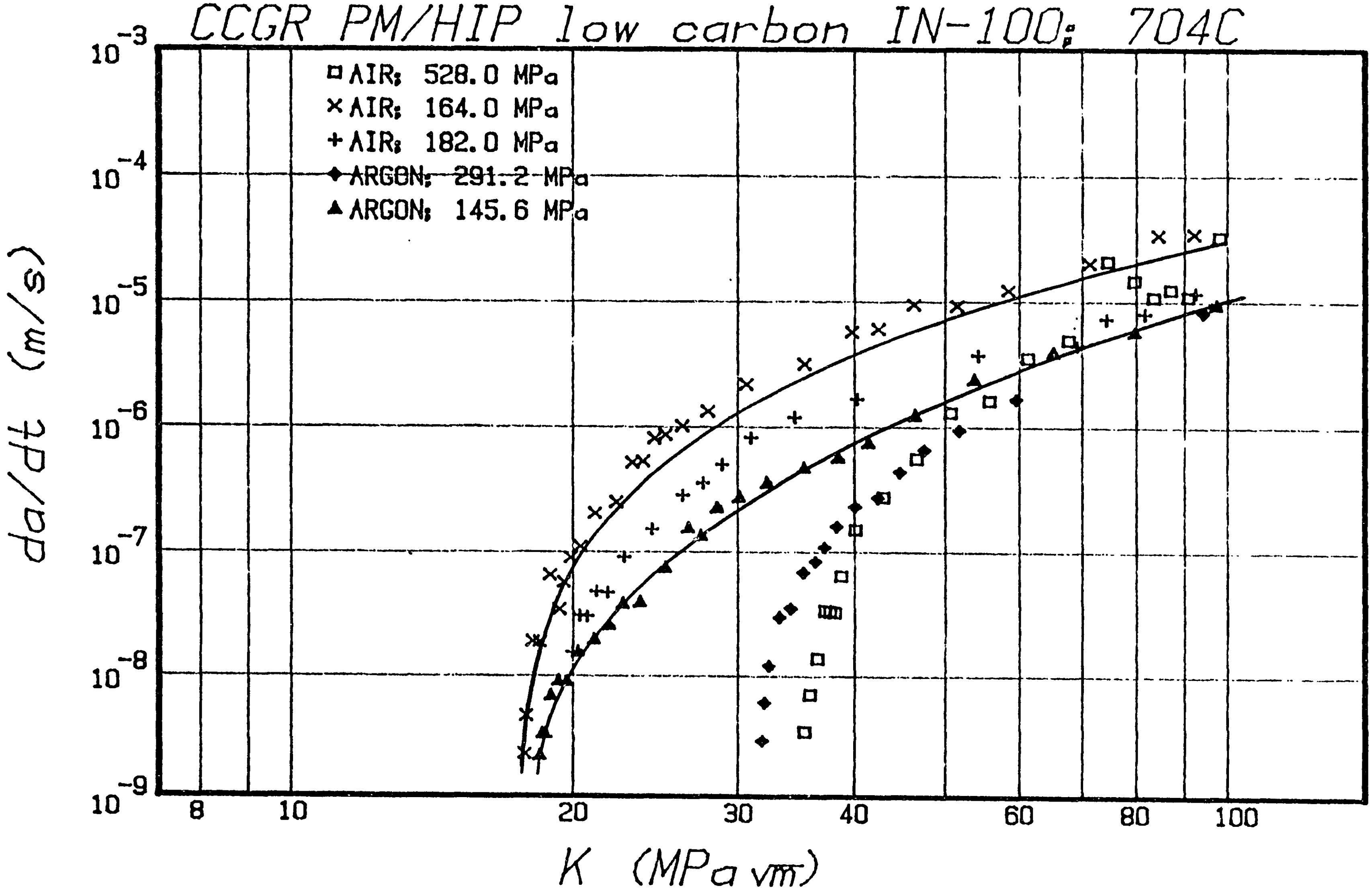

FIGURE 4.5) CCGR results for PM/HIP low carbon IN-100 at 704°C in both air and in 99.999% pure argon.

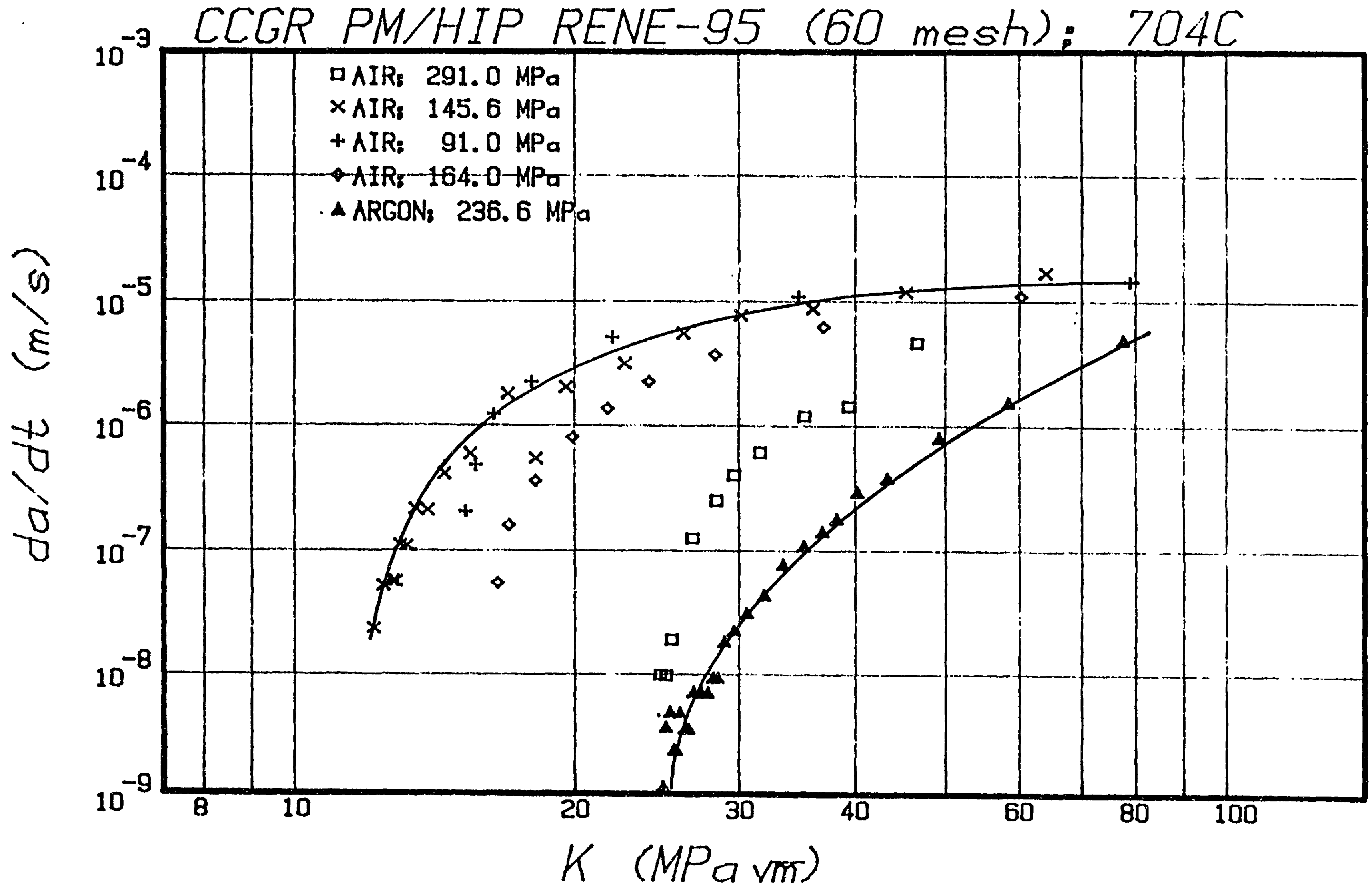

FIGURE 4.6) CCGR results for PM/HIP RENE-95 (60 mesh powder) at 704°C in both air and in 99.999% pure argon.

K curve Stage II in air was 2, and for purified argon the slope was 4.

4.4.1.5. CCGR of PM/HIP Rene-95 (120 mesh)

The change in the CCG behavior at 704°C between an air atmosphere and an argon atmosphere was not as pronounced as was observed for the larger mesh size. (Figure 4.7) The increase in the CCGR in air over the CCGR in argon is only 10 times.

The CCGR in air for the finer 120 mesh size is the same as the larger 60 mesh size Rene-95. The finer mesh size has a faster CCGR in an argon atmosphere. The difference is the result of grain size and powder particle size variations. The crack follows the prior particle boundaries in argon, but it follows the grain boundaries in air. The finer mesh size has a faster CCGR in argon because of the smaller prior particle size, but the grain size for both mesh sizes is the same (grain size = 25um.)

4.4.2. Effect of Initial Stress Intensity Factor

The initial stress intensity factor, K_i, was varied from $K_i = 14.2\ \text{MPa}\sqrt{m}$ to $43.2\ \text{MPa}\sqrt{m}$ for PM/HIP Merl-76 at 704°C in an air atmosphere. (Figure 4.8) The CCGR rises quickly to a region of gradually increasing CCGR versus K. The initially low CCGR results from the lack of damage ahead of the crack. Once the first jump in the crack front has occurred, the crack tip encounters material which has been

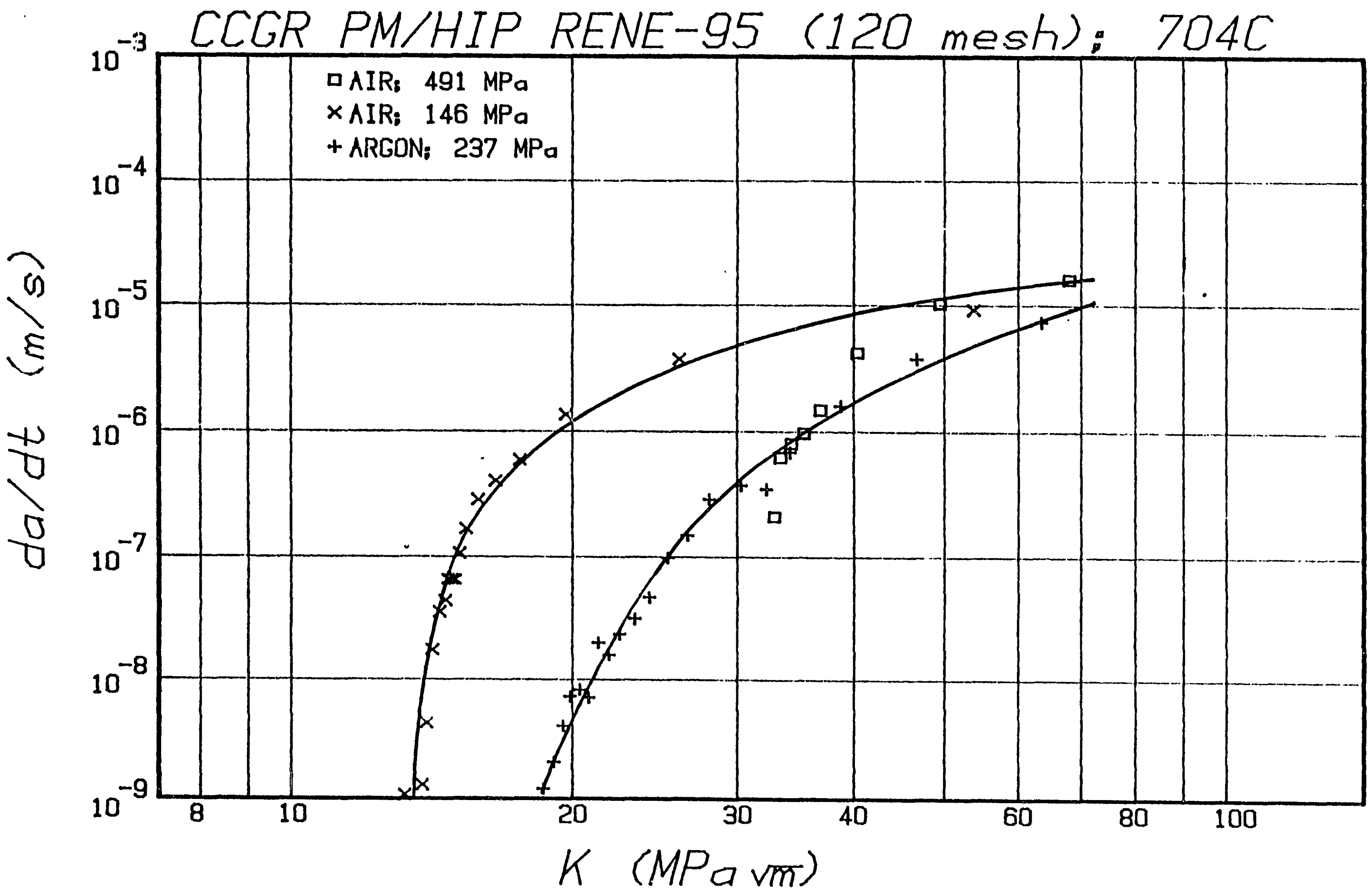

FIGURE 4.7) CCGR results for PM/HIP RENE-95 (120 mesh powder) in both air and in 99.999% pure argon.

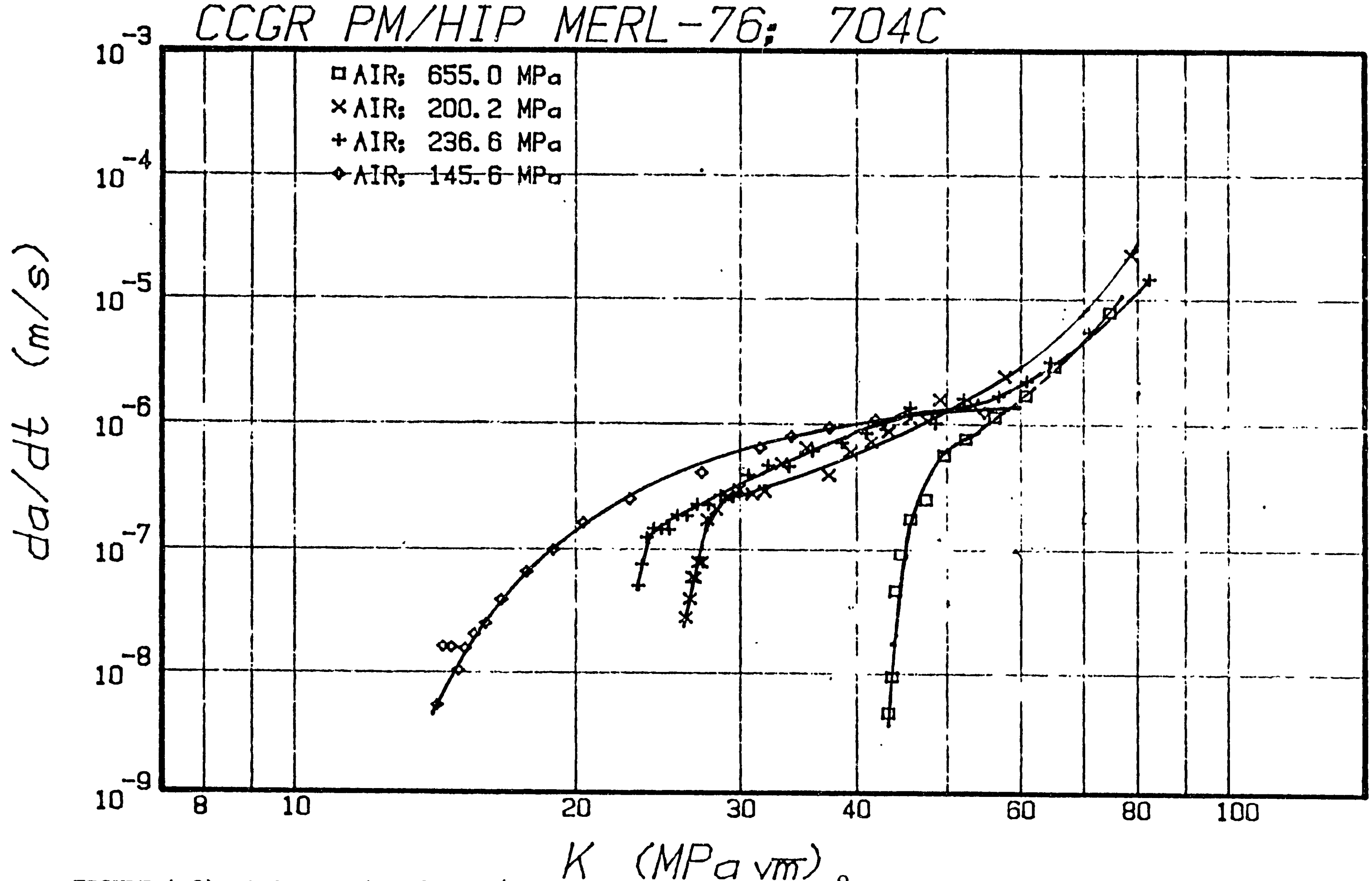

FIGURE 4.8) CCGR results for PM/HIP MERL-76 in air at 704°C for different initial K and gross section stresses.

creep and oxidation damaged ahead of the crack tip. This damaged material requires less time (and creep ductility) to fracture and the crack growth rate increases. The CCGR increases until the dynamic process of damage accumulation ahead of the crack tip and the crack advance reach equilibrium. The CCGR depends on changes in the load history, the stress intensity factor, and dK/da in the specimen.

4.4.3. Comparison of CCGR in Air

A comparison of CCGR versus K curves for all the alloys in air at 704°C is given in Figure 4.9. The results indicate that all the alloys exhibit CCGR between 10^{-7} m/s to 10^{-5} m/s in a range of K from 20 to 100 $\mathrm{MPa}\sqrt{\mathrm{m}}$. The slopes in the stage II region of the curves vary from 2 to 4. Astroloy and Merl-76 have the lowest CCGR in air while Rene-95 (60 and 120 mesh) and IN-100 have the fastest CCGR.

In all the alloys the fracture path is totally intergranular. Fracture surfaces in Astroloy have intergranular prior particle boundary cracking at K greater than 60 $\mathrm{MPa}\sqrt{\mathrm{m}}$.

4.4.4. Comparison of CCGR in Argon

A comparison of the CCGR versus K curves for all the alloys in argon at 704°C is shown in Figure 4.10. The CCGR in argon are compared to the air results in Figure 4.11. The CCGR for all the alloys is higher in air than in argon.

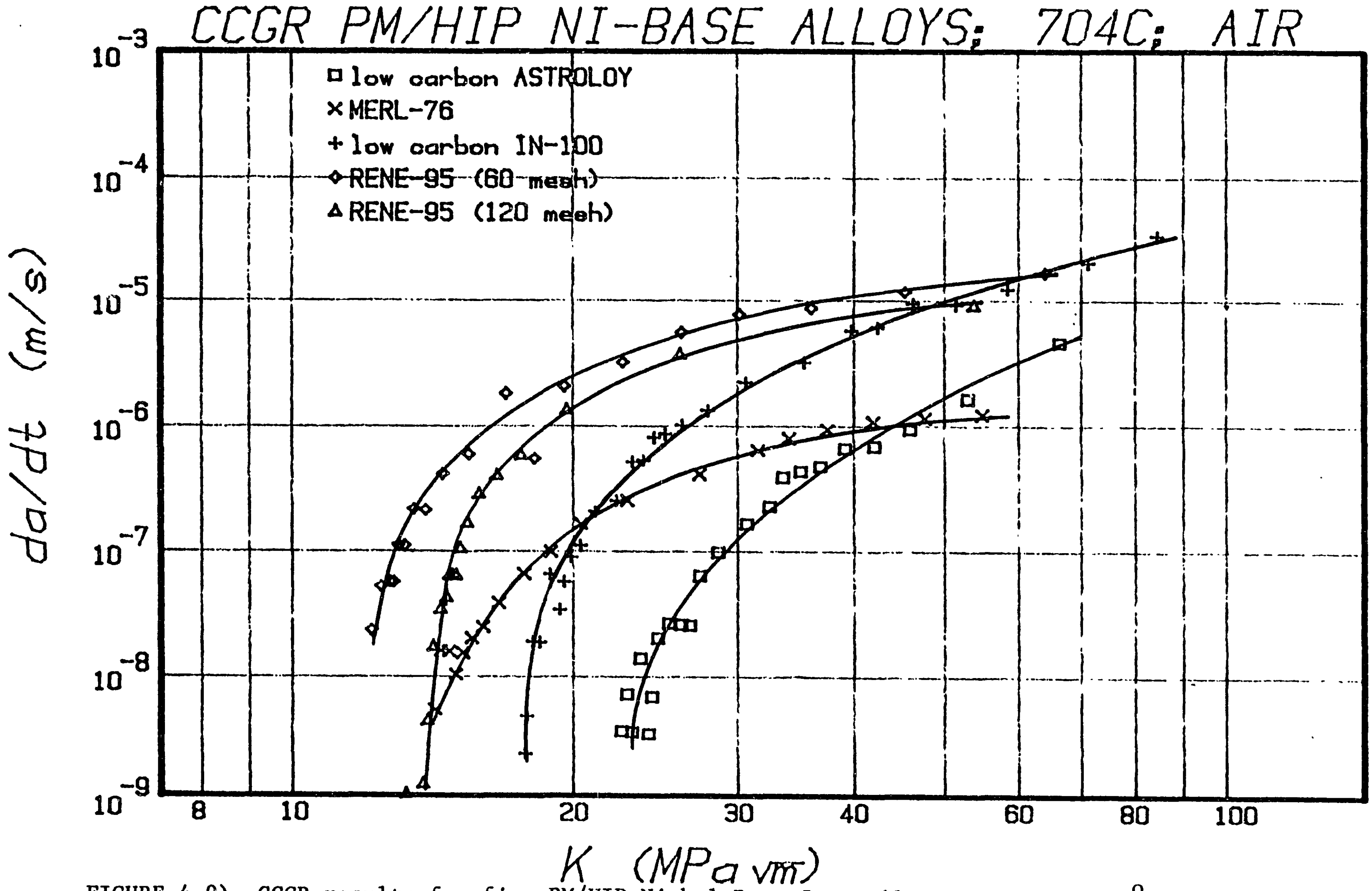

FIGURE 4.9) CCGR results for five PM/HIP Nickel-Base Superalloys in air at 704°C.

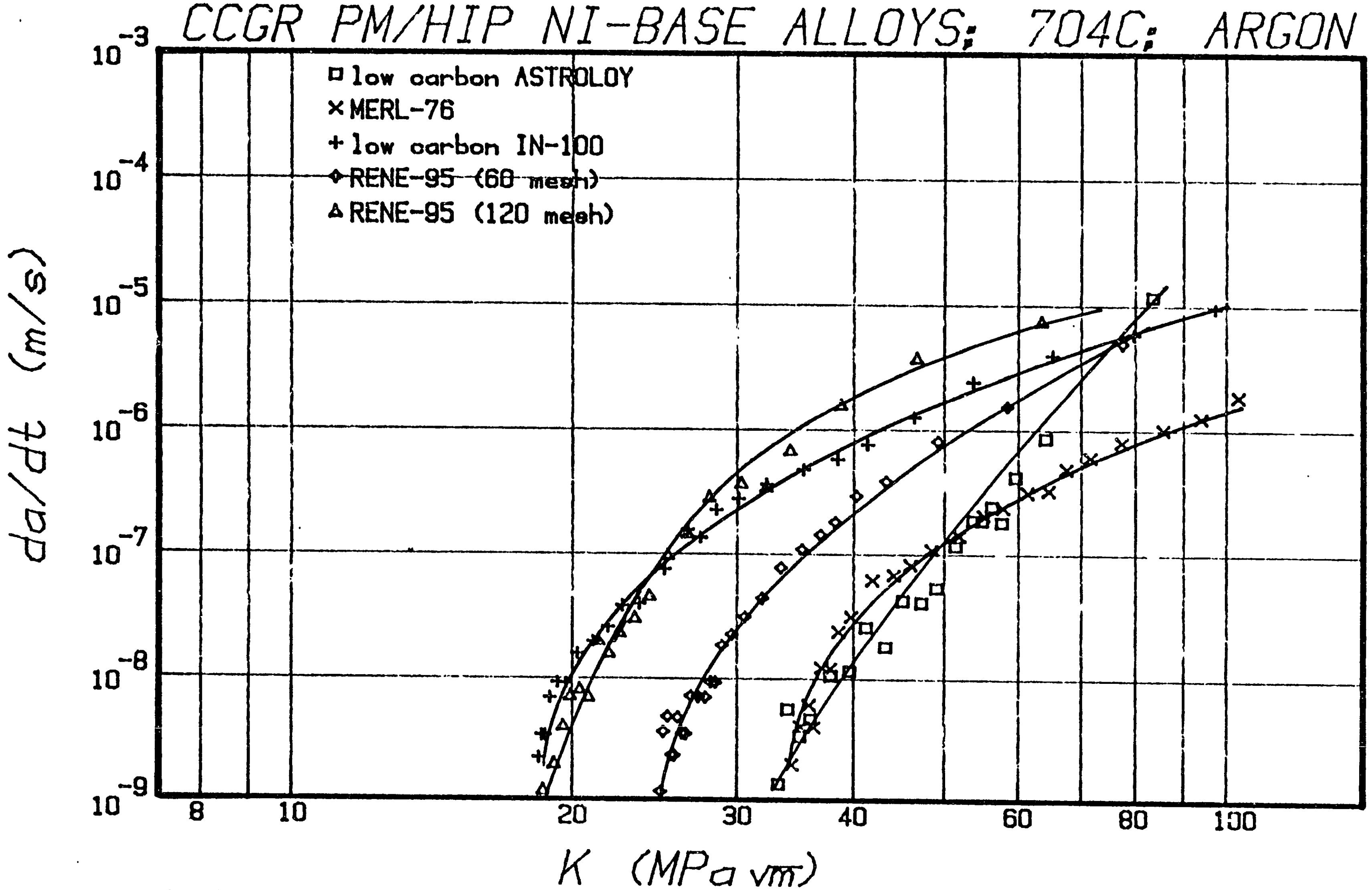

FIGURE 4.10) CCGR results for five PM/HIP Nickel-Base Superalloys in 99.999% pure argon at 704°C.

The slopes of the stage II region of crack growth in argon is higher than in air and it ranges from 3.5 to 6. Astroloy has the lowest CCGR at low K, but Merl-76 becomes slower at higher K values. Rene-95 (120 mesh) and IN-100 have the fastest CCGR in argon at all values of K.

The fracture path in argon is intergranular, along grain boundaries which are also prior powder particle boundaries.

4.4.5. Validity of K Correlation of CCGR

The CCGR curves for Merl-76 in air are shown in Figure 4.8. These results are for a range of gross section stress from 145.6 MPa to 655 MPa. The CCGR for Merl-76 in the Stage II and Stage III regions of creep crack growth rate versus K curves indicate a K-dependancy on crack growth with a scatter of approximately half an order of magnitude in CCGR. There is a trend in the results which indicate a higher crack growth rate for a lower initial K and a lower gross section stress. This behavior is attributed to the value of dK/da in the specimen; it will be explained in chapter 5. A good correlation exists between da/dt and K for all the alloys tested in both air and argon with scatter being within one half an order of magnitude in CCGR. This result should not be surprising since the materials are creep-brittle and the crack tip stresses are well characterized by K.

The initial transient behavior, Stage I cracking, does not correlace with K. In general it is observed that the initial crack growth rate increases with increasing K, but this is not always true. Tests which are performed at a large initial stress intensity never exhibit stage II cracking, but proceed directly from Stage I to Stage III crack growth.

4.4.6. Fractography of CCG Tests

The fracture path for all the creep crack growth tests was intergranular. The tests in argon fractured along grain boundaries which coincided with prior powder boundaries. In air the cracks were not limited to prior powder boundaries.

Fatigue precracking was performed at room temperature. The crystallographic fracture path of the fatigue precrack can be seen in Rene-95 (120 mesh) and IN-100. (Figure 4.11) The transition from fatigue crack growth to creep crack growth appears as a sharp fractographic transition for all the alloy tested.

The transition from creep crack growth to fast fracture is also very sharp for the air tests in air. The sharp transition results from the difference between the brittle intergranular fracture surface observed for CCG in air and the ductile, mixed intergranular-transgranular fracture which is observed for fast fracture. (Figure 4.12) The transition between creep crack growth and fast fracture is more difficult to detect in tests performed in argon.

Figure 4.13 shows the transition from CCG to fast fracture for IN-100 in air.

4.4.6.1. Argon Tests

In general the creep crack in argon follows prior powder boundaries. The fracture surface shows more grain boundary cavitation in argon than in air as is shown in Figure 4.14 for Astroloy. Figures 4.15 and 4.16 show the fracture surfaces for IN-100 and Rene-95 (60 mesh) respectively in argon at 704°C. The round prior powder particles can be easily detected on the fracture surface.

Figure 4.17 shows the typical fracture appearance for argon CCG tests for the 4 alloys. The round prior particles are easily seen in all the fractures. The size of the particles is determined by the mesh size used for each alloy.

High magnification photomicrographs of the alloys in argon revealed fracture features which may be cavities. These cavity like features are shown in Figure 4.18 for Rene-95 (60 mesh) and Merl-76 at 10,000 x. The fracture surfaces in Figure 4.18 were from CCGR tests in argon which were not oxidized.

4.4.6.2. Air Tests

Figure 4.19 shows the typical fracture surfaces for the four alloys when the CCG tests were run in air at 704°C. The fracture path was totally intergranular with flat featureless boundaries characteristic of brittle fracture. The surfaces obtained in air tests are heavily oxidized as a result of exposure to oxygen at 704°C . High magnification photomicrographs failed to reveal any cavity-like features. (Figure 4.20)

The CCGR versus K results for Astroloy in Air intersect the CCGR results obtained in argon at K = 60 $MPa\sqrt{m}$. The fracture surfaces of the CCG tests in air have a transition at K= 60 $MPa\sqrt{m}$ from intergranular, brittle fracture to a predominantly prior particle boundary fracture path which has been shown to be characteristic of the fracture surfaces obtained in an argon environment. This transition is physical evidence supporting the conclusion that at high creep crack growth rates in Astroloy the crack grows faster than the embrittling effect of oxygen.

The fracture surfaces for the notched stress rupture tests in air are the same as that observed for the air CCGR tests.

4.5. Penetration of Oxygen Results

The depth of intergranular fracture following oxygen exposure at 704°C varied from alloy to alloy. Astroloy exhibited the smallest depth of damage and Rene-95 (60 mesh) showed the largest depth of intergranular damage. The results are summarized in Table 4.5.

TABLE 4.5

Depth of Intergranular Embrittlement after a 100 hour Exposure at 704°C in Air

Alloy	Average Depth of Embrittlement (um)	Effective Calculated Diffusivity (m^2/s) $D = x^2/t$
Low C Astroloy	84	1.96×10^{-14}
Merl-76	310	2.67×10^{-13}
Low C IN-100	720	1.44×10^{-12}
Rene-95 (60 mesh)	840	1.96×10^{-12}

The results indicate that Astroloy and Merl-76 are only slightly embrittled and therefore should have lower creep crack growth rates in air than either IN-100 or Rene-95. This result has been verified in section 4.4.3.

FIGURE 4.11) FRACTOGRAPH OF THE FATIGUE PRECRACK-CCG TRANSITION IN PM/HIP RENE-95 (120 MESH POWDER) TESTED AT 704°C IN AIR.

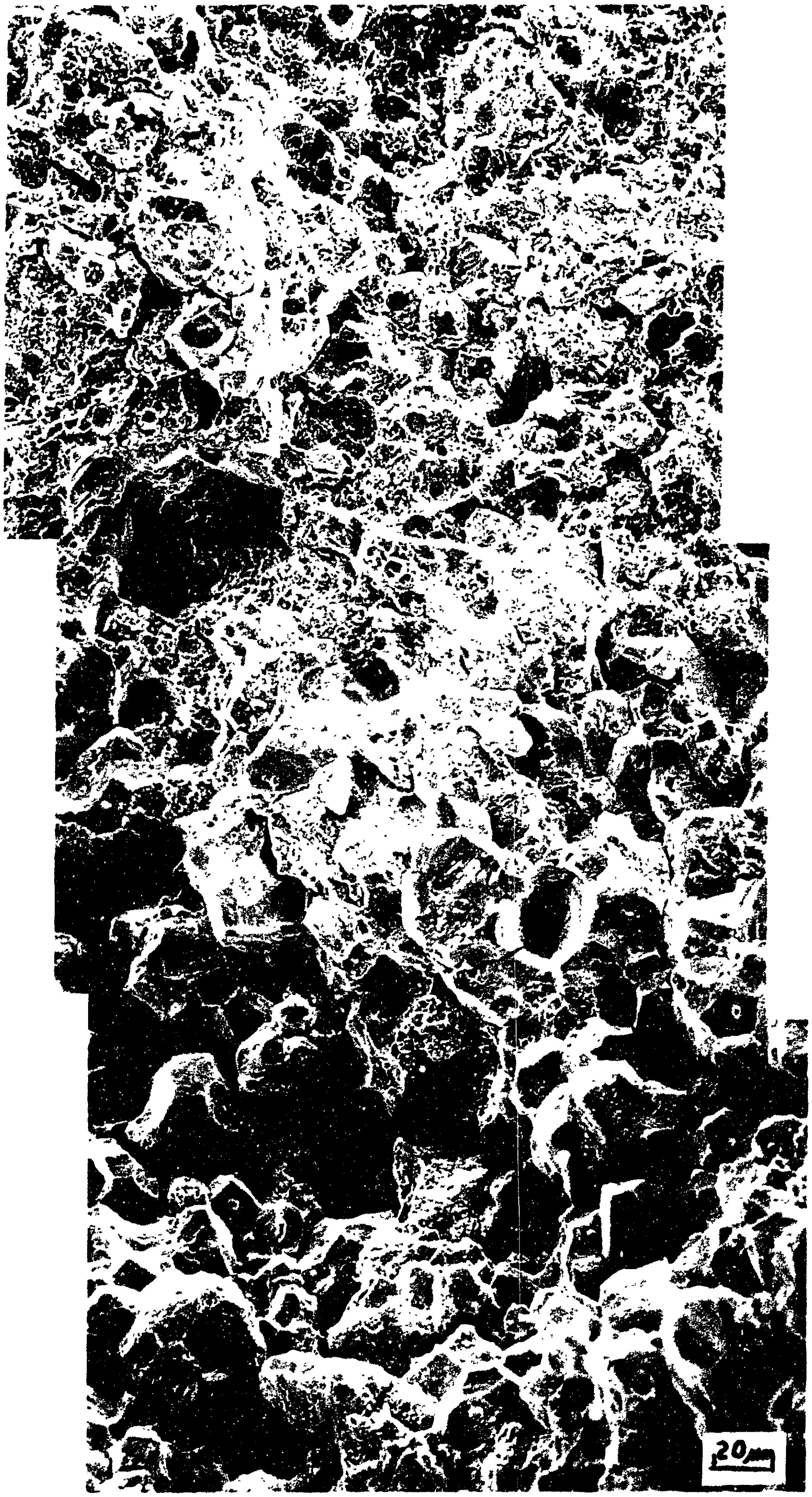

FIGURE 4.12) Fractograph of the CCG-Fast Fracture transition in PM/HIP Low C IN-100 tested at 704°C in air.

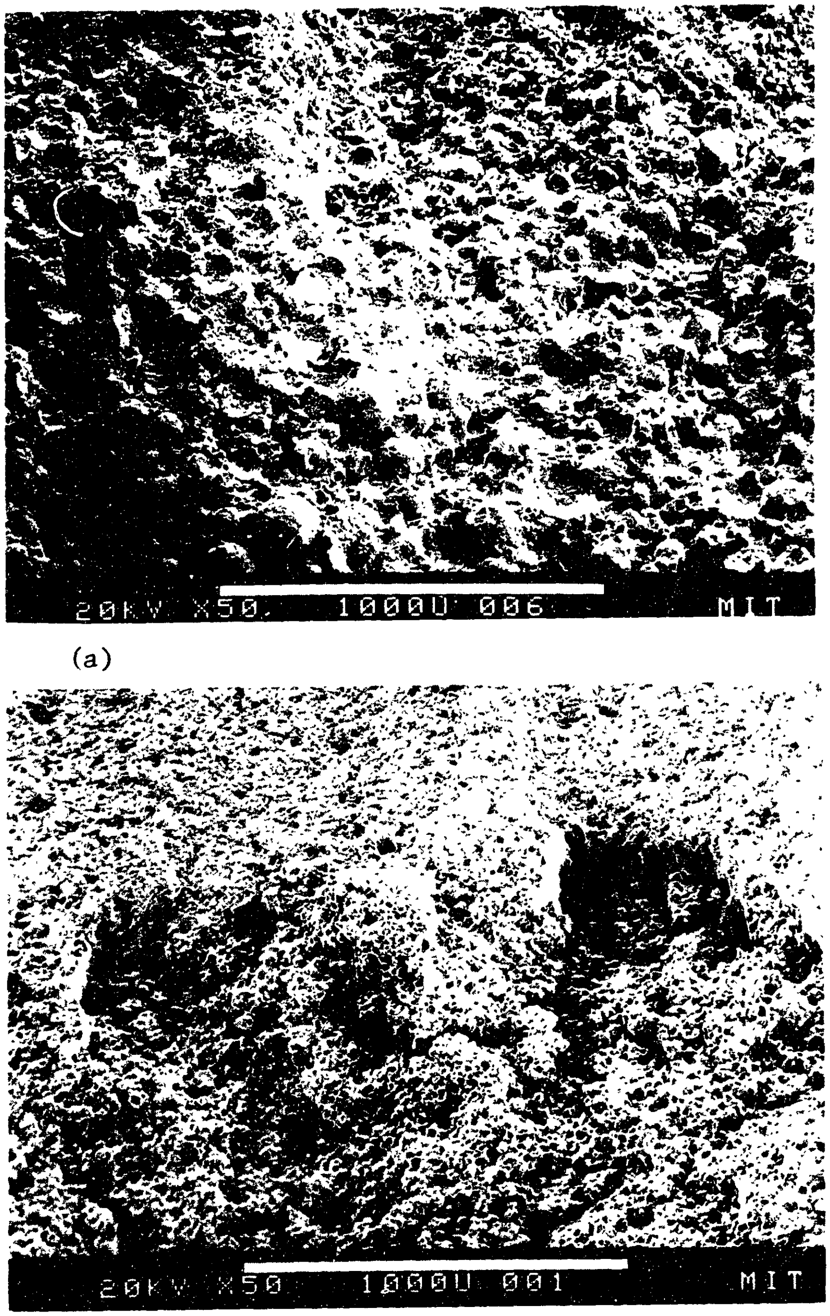

(a)

(b)

FIGURE 4.13) Fractographs of the CCGR-Fast Fracture transition in PM/HIP Low C IN-100 tested at 704°C. (a) in 99.999% pure argon; (b) in air.

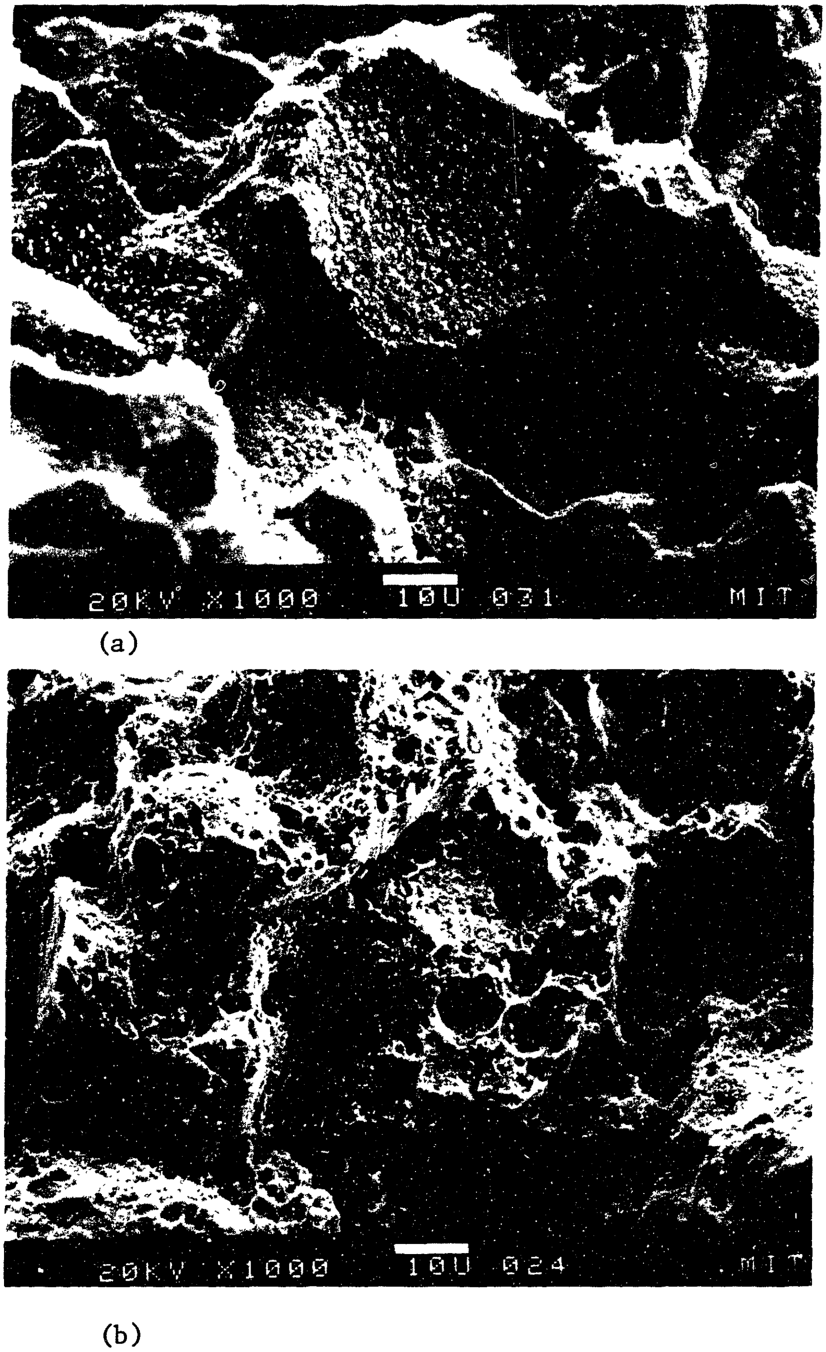

FIGURE 4.14) Fractogrphs of PM/HIP Low C ASTROLOY at 704°C. (a) CCGR test in air; (b) CCGR test in 99.999% pure argon.

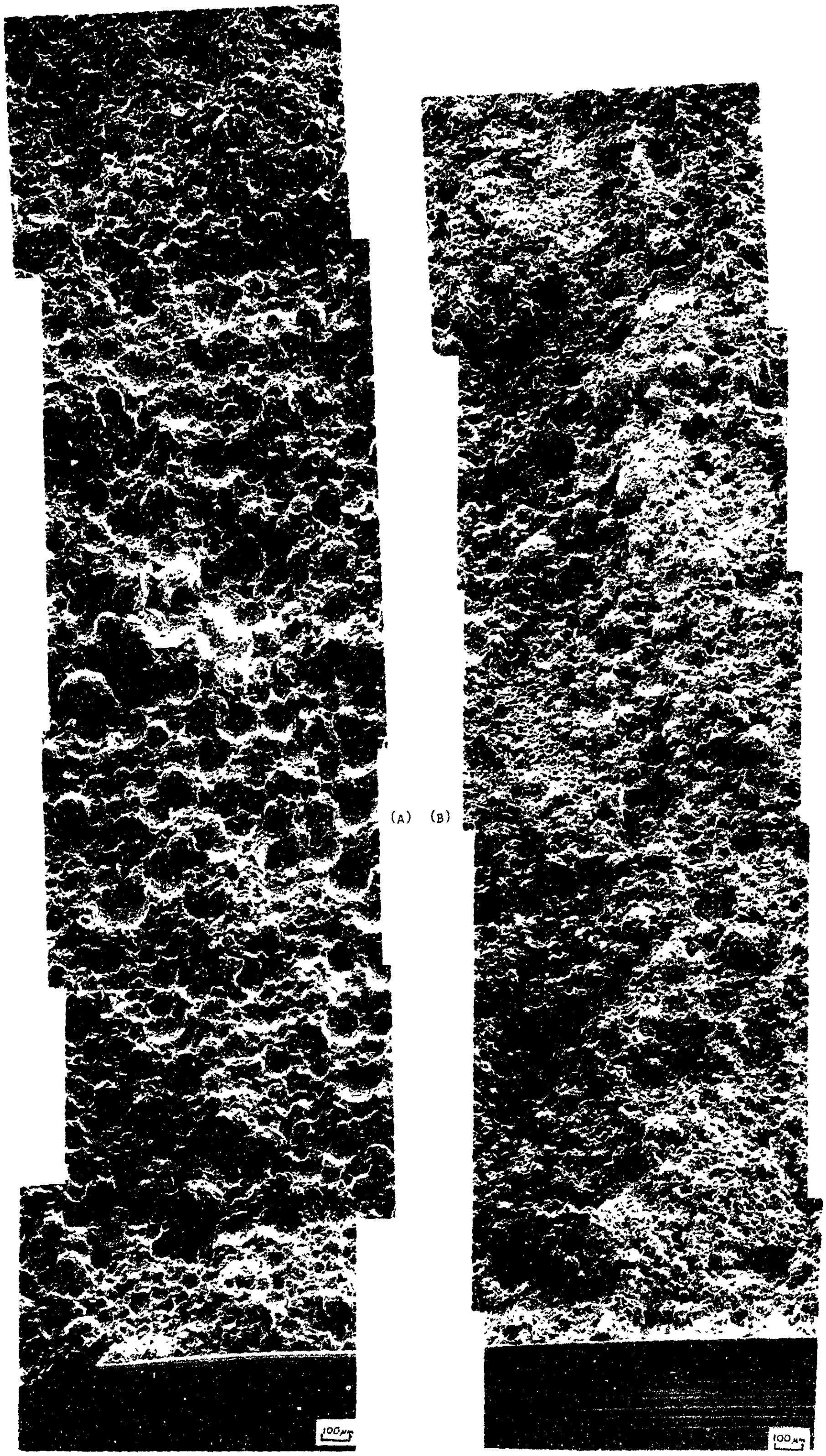

FIGURE 4.15) Fractographs of Creep Crack Fractures in 99.999% pure argon. (a) PM/HIP Low C IN-100: (b) PM/HIP RENE-95 (120 mesh powder)

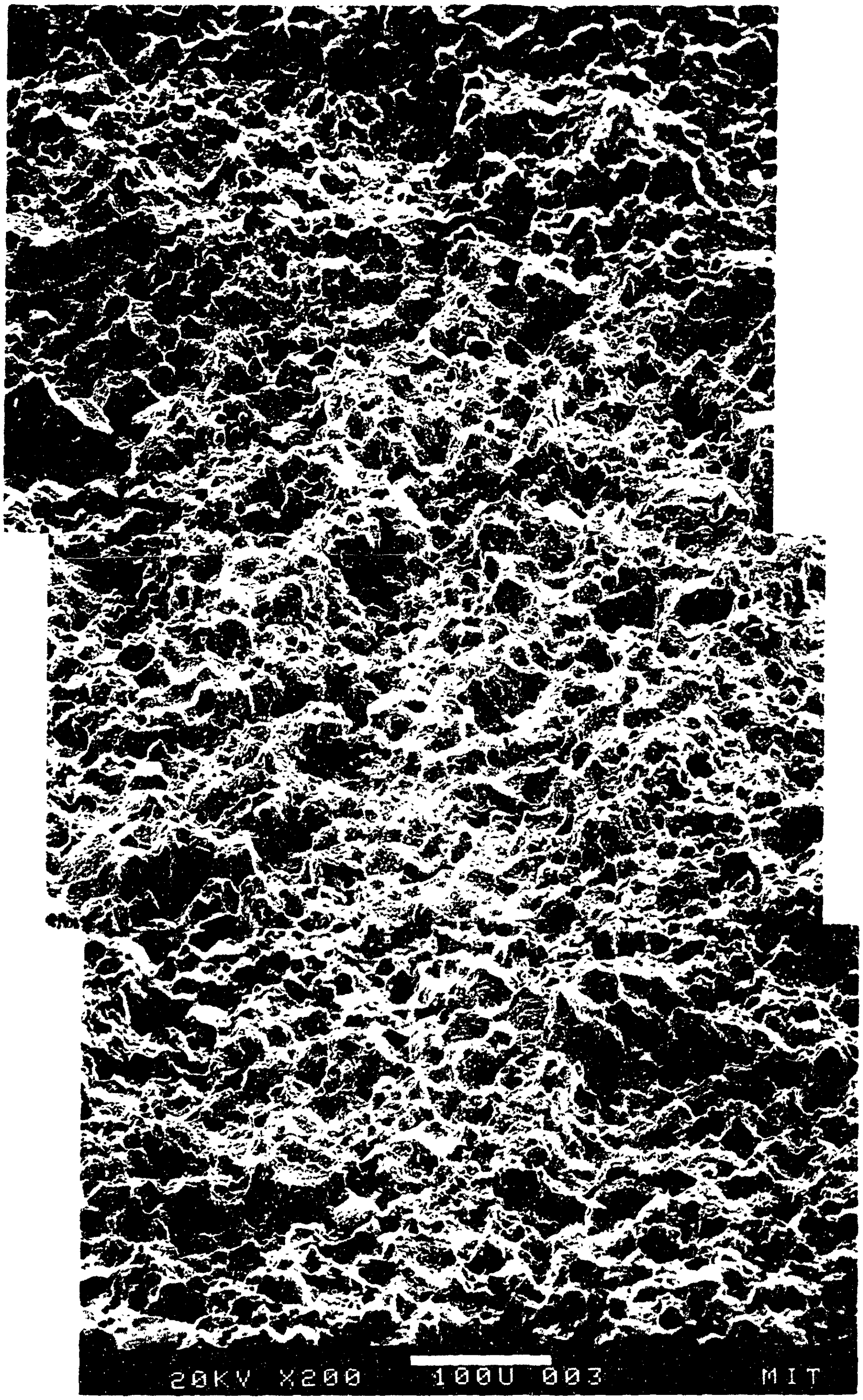

FIGURE 4.16) Fractograph of a CCGR specimen tested in air at 704°C. (PM/HIP RENE-95 (120 mesh powder))

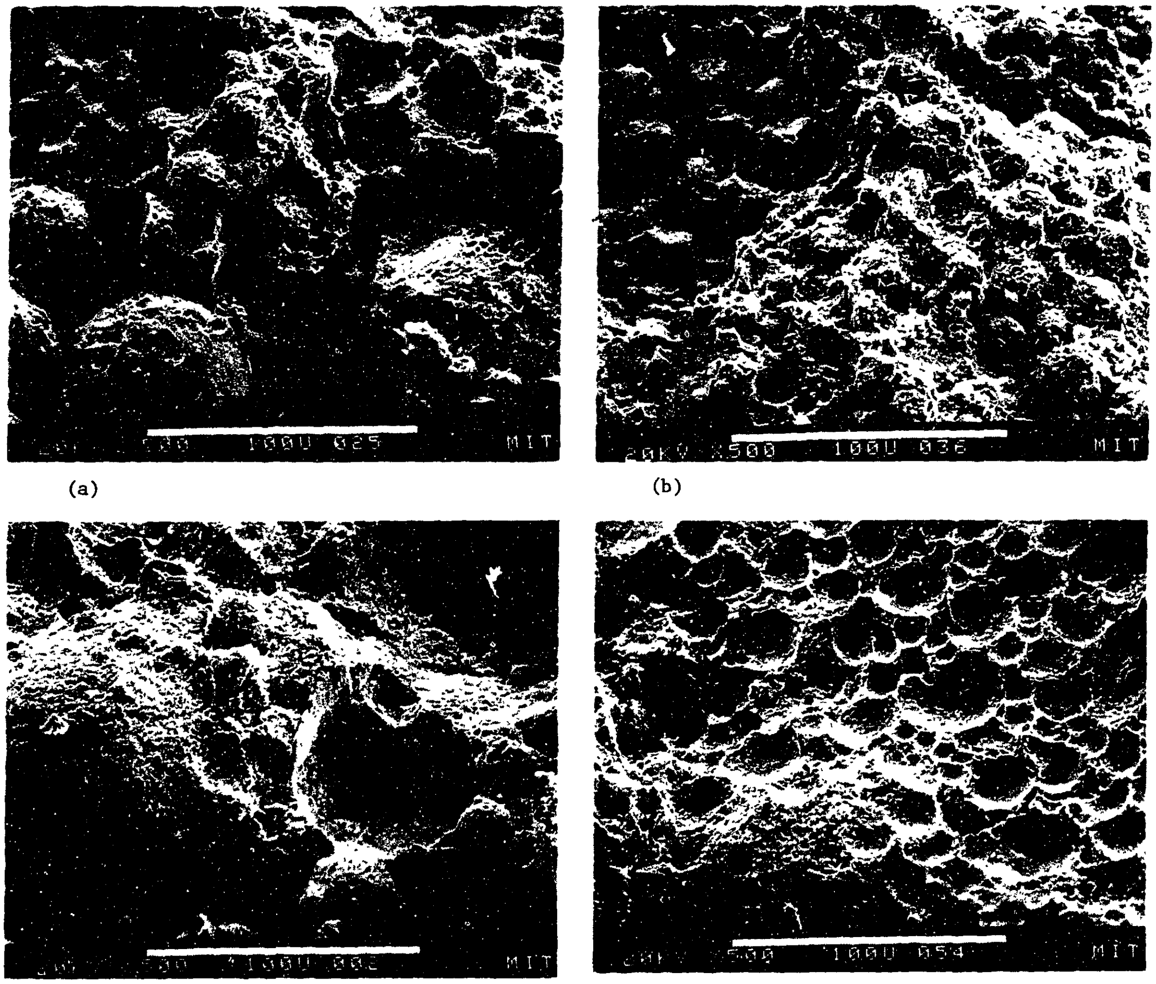

(a) (b)

(c) (d)

FIGURE 4.17) Typical fractographs of four PM/HIP Nickel-Base alloys tested in argon at 704°C. (a) Low C ASTROLOY; (b) MERL-76; (c) Low C IN-100; (d) RENE-95 (60 mesh).

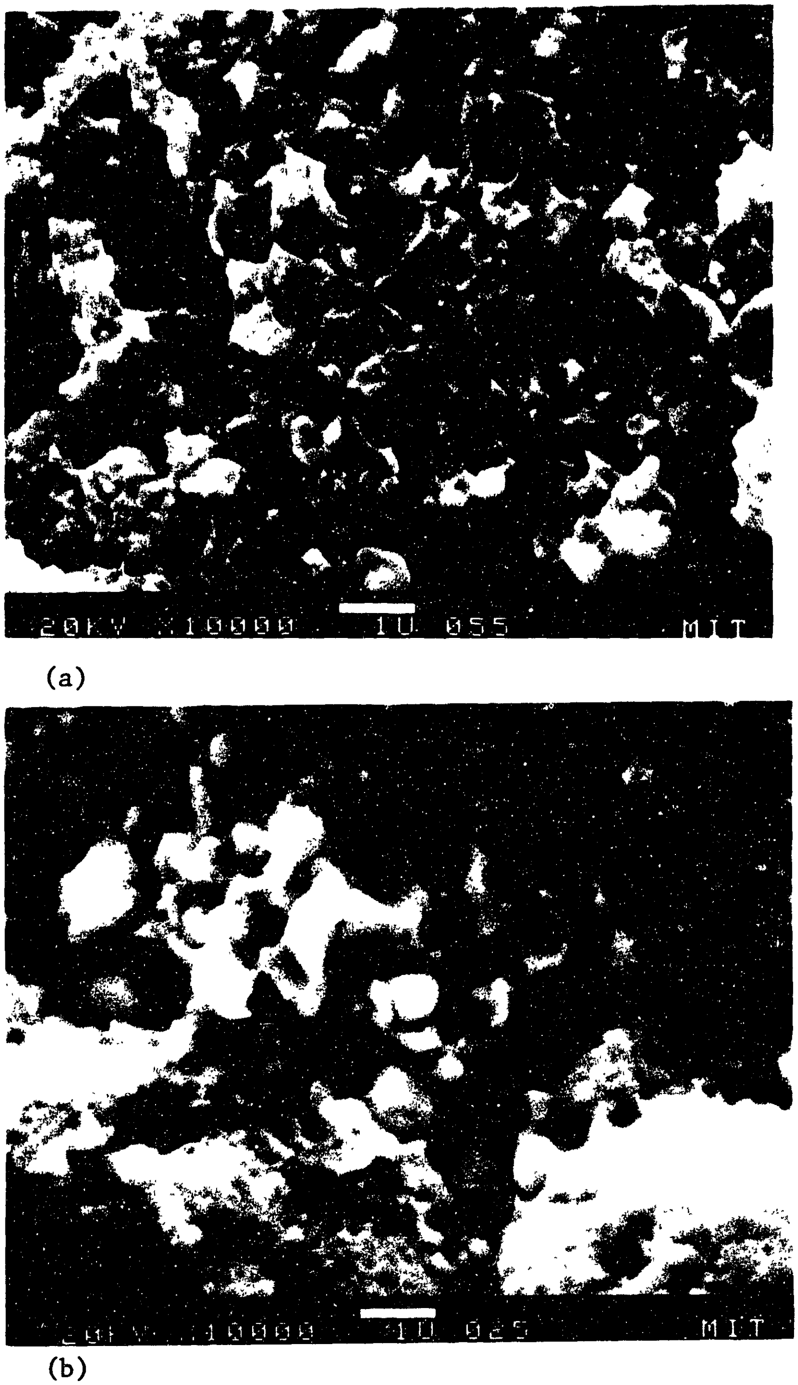

(a)

(b)

FIGURE 4.18) Fractographs of cavity like featurew on creep crack fracture surfaces from CCGR tests in argon at 704°C. (a) PM/HIP RENE-95 (60 mesh); (b) PM/HIP MERL-76.

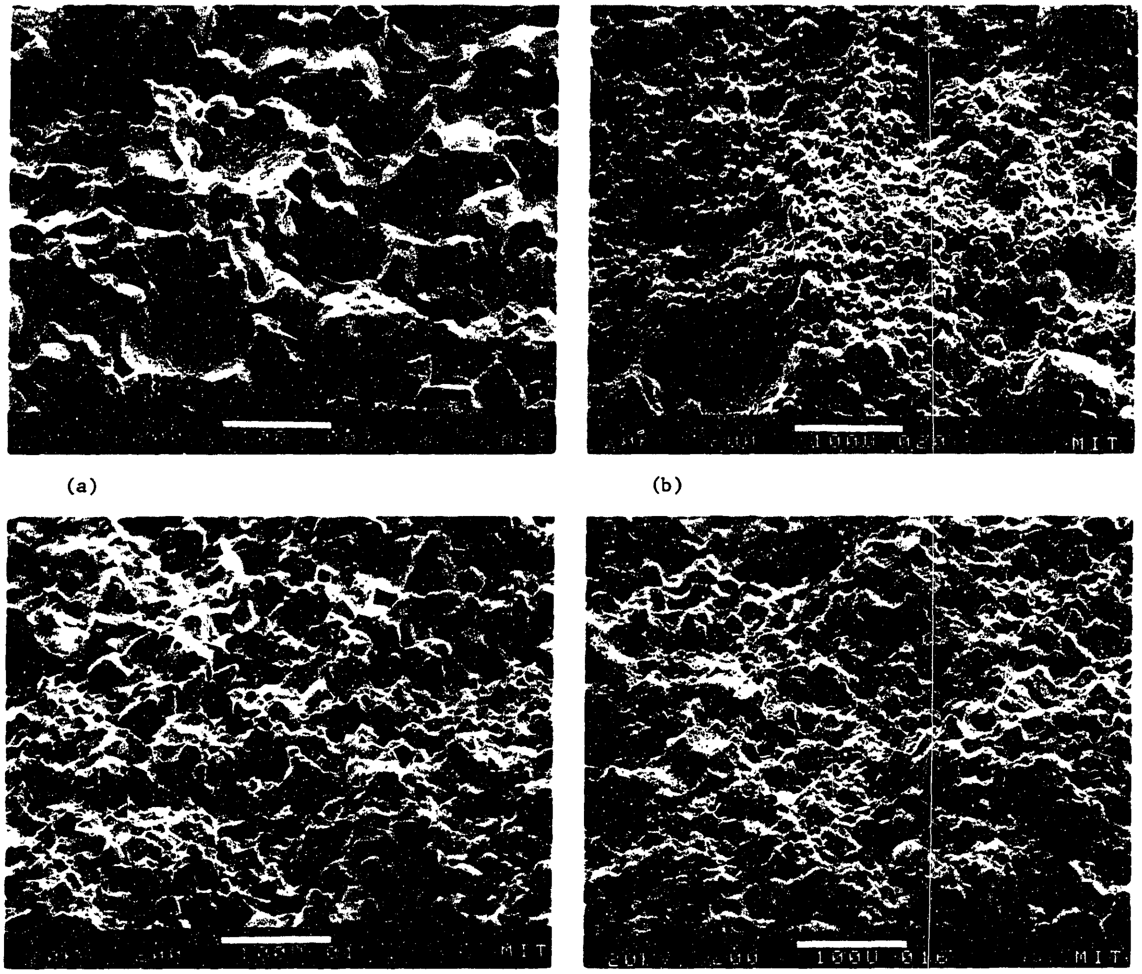

(a) (b)

(c) (d)

FIGURE 4.19) Typical creep crack fracture surfaces in air at 704°C in four PM/HIP Nickel-Base alloys. (a) Low C ASTROLOY; (b) MERL-76; (c) Low C IN-100; (d) RENE-95 (60 mesh).

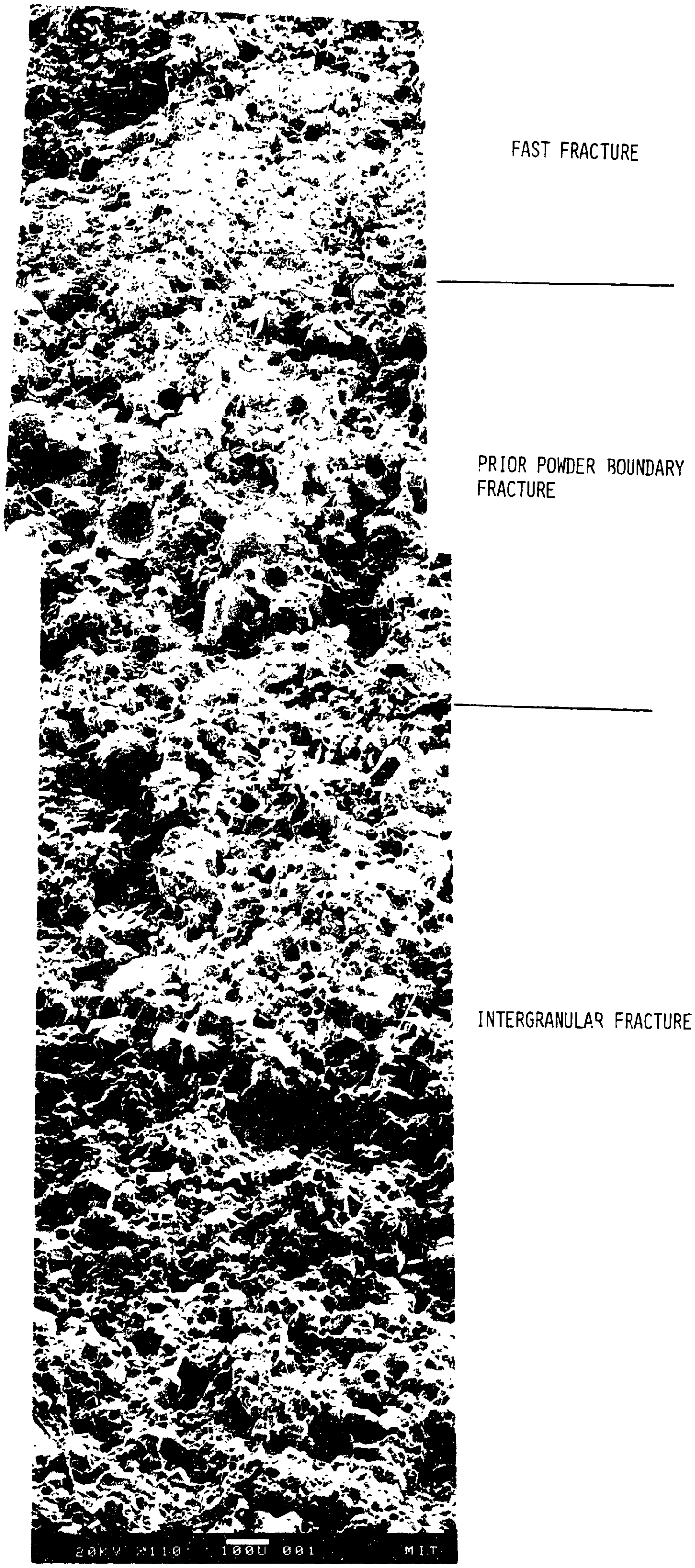

FIGURE 4.20) TYPICAL FRACTOGRAPH OF A CCGR TEST ON PM/HIP LOW C ASTROLOY TESTED IN AIR AT 704°C.

5. AN ITERATIVE MODEL FOR CREEP CRACK GROWTH

5.1. Introduction

A computer model for creep crack growth is developed based on the accumulation of damage ahead of the crack tip for a specimen which is creep brittle and satisfies the conditions of small scale yielding. The damage is based on creep strain accumulation in elements which are assumed to have the dimension of the critical microstructural parameter (i.e. grain size or prior powder size). The plastic strain and primary creep strain are assumed to make a negligible contribution to the total amount of damage. The crack advances by one element when the element immediately ahead of the crack tip achieves a critical value of creep strain. After a crack advance, the stresses in all the elements are reset to calculated initial HRR stress. The assumption that the stresses reset to the HRR stress after a crack advance was done in the interest of simplicity. However, the actual stress will be slightly lower as a result of the accumulated creep strain which has gone before. Creep strain accumulation is calculated using the stress given by Riedel and Rice (74) in creeping material ahead of a stationary crack. This model differs from an earlier model by Huang (63) in placing an upper bound on stress at the crack tip, and by using the equivalent stress rather than stress in the y-direction. Crack tip stresses are assumed to begin relaxing from their HRR values immediately after loading as a result of the accumulating creep strain. (See Figure 2.16).

The effect of oxygen on crack growth is modelled by a change in element size from prior powder size to grain size and a reduction in the value of the critical strain necessary for crack advance.

The model predicts the creep crack growth rate as a function of K-history and K. CCGR is also shown to be strongly dependent upon changes in creep rate, yield strength, and critical strain. The effect of temperature on the predicted CCGR is accounted for in changes in the secondary creep rate and yield strength. The critical creep strain is assumed not to change with temperature.

5.2. Numerical Procedures

5.2.1. Calculation of Stress and Strain

Stresses ahead of the crack tip at time=0 must first be determined. This initial stress distribution then relaxes with increasing time, t>0. The stress in the far field is σ_0. Closer to the crack tip, at radius "r" the stresses are described by the elastic stress intensity factor, K_I (99).

$$\sigma_E = \frac{K_I}{\sqrt{2\pi r}} f_E(\Theta) \qquad \text{(Eq. 5.1)}$$

f (Θ) is a factor for each stress component that depends only on the angle (Θ) from the plane of the crack.

The equivalent stress, σ_E , in the plastic region ahead of the crack at t=0 is given by the HRR singularity (70, 71, 72):

$$\sigma_E \propto \left(\frac{K^2}{r}\right)^{(1/(N_p+1))} \qquad \text{(Equ. 5.2)}$$

N_p is the stress exponent from equation 5.3:

$$\varepsilon^{p} = B_p(\sigma)^{N_p} \qquad \text{(Equ. 5.3)}$$

where ε^p is the plastic strain.

The size of the plastic zone, R_p, is estimated by the expression for plane strain loading and non-hardening plasticity (99):

$$R_p = .1 \left(\frac{K_I}{Y}\right)^2 \qquad \text{(Eq. 5.4)}$$

where Y is the yield strength. The calculation for the plastic zone size can be combined with the HRR stress field:

$$\sigma_E \propto \left(\frac{R_p}{r}\right)^{(1/(N_p+1))} \quad \text{(Eq. 5.5)}$$

At r=Rp σ_E=Y, so equation 5.5 gives:

$$\sigma_E = Y \left(\frac{R_p}{r}\right)^{(1/(N_p+1))} \quad \text{(Eq. 5.6)}$$

The equivalent stress calculated by the model ahead of the crack tip at t=0 is illustrated in Figure 5.1. The approximation of the stress-strain relationship given by equation 5.3 and substituted into equation 5.6 yields stresses which are slightly above the actual stresses given by the HRR singularity. The effect of a lower stress is corrected by assuming a 10-20% smaller critical strain than is obtained from smooth bar creep rupture results.

For t>0 the stresses in the plastic and elastic zones relax as a result of creep strain ahead of the crack tip. The relaxation is described by Riedel and Rice (74):

$$\sigma_E = \left(\frac{.29\ K^2}{r\ E\ (N_c+1)\ B_c\ t}\right)^{(1/(N_c+1))} f_E(\Theta,N_c) \quad \text{(Eq. 5.7)}$$

where B_c and N_c are the material constants for Norton's law:

$$\dot{\varepsilon}^c = B_c(\sigma)^{N_c} \qquad \text{(Eq. 5.8)}$$

$\dot{\varepsilon}^c$ is the minimum creep rate as determined via smooth bar creep rate measurements. The term f (Θ,N) is taken as 1.

The RR stress calculation indicates that at time 0 the stress (σ_E) starts at infinity. This is obviously impossible and an upper bound on stress is the stress predicted for t=0 by HRR. A transition time can be calculated at which the creep-relaxed stress given by the RR calculation (5.7) is the same as the stress $\sigma_{t=0}$ at r and t=0 given by HRR (5.2). (See Figure 2.16)

$$t_{transition} = \frac{.29\ K^2}{B_c E\ (N_c+1)\ r\ (\sigma_{t=0})^{(N_c+1)}} \qquad \text{(Eq. 5.9)}$$

This calculated transition time does not relate to the real test time, but it is only a starting time for subsequent creep strain calculated according to the RR equation (5.7).

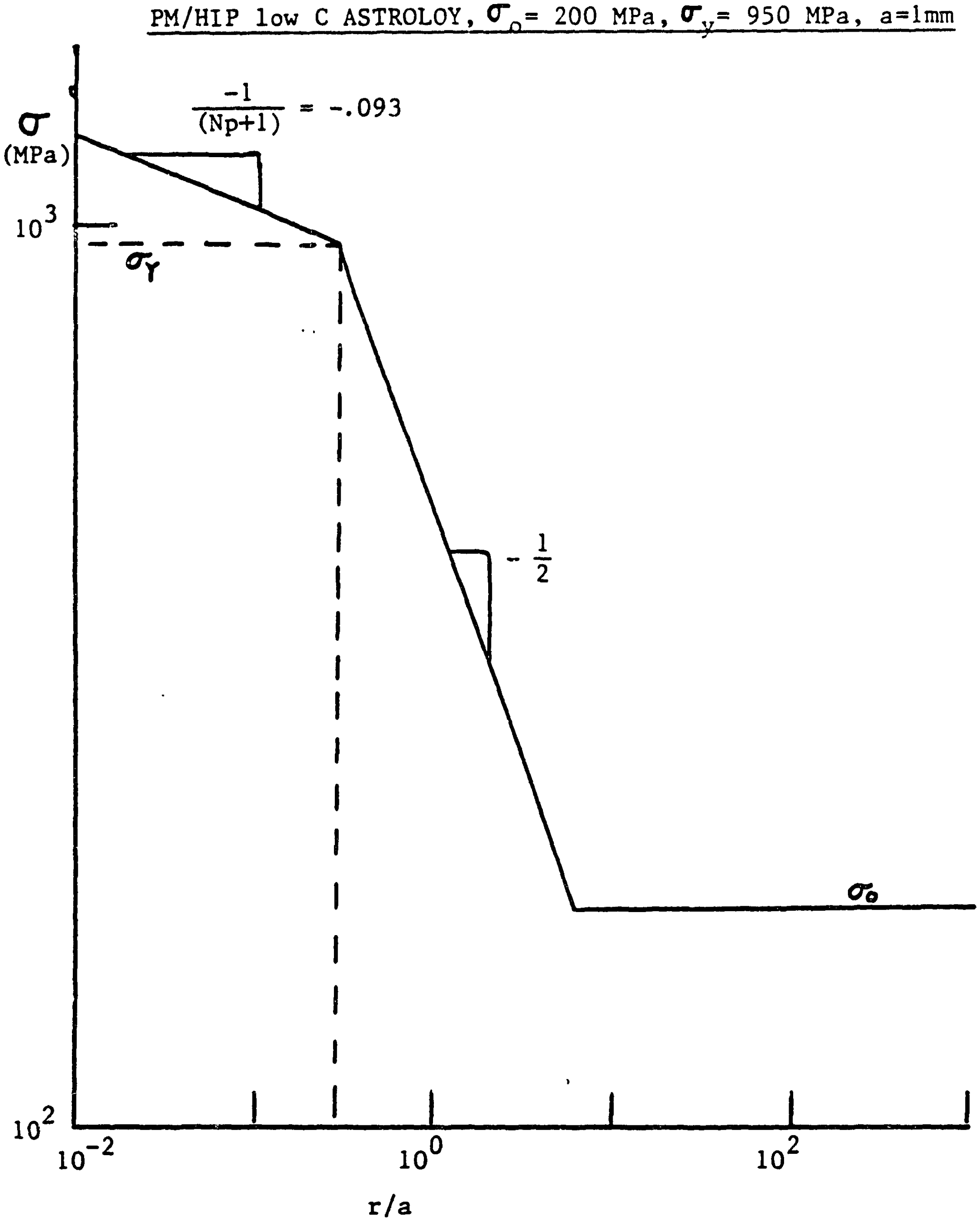

FIGURE 5.1) Equivalent stress ahead of a creep crack at time=0 in a PM/HIP nickel-base superalloy at 704°C.

5.2.2. The Accumulation of Strain

The creep strain ahead of the crack tip as a function of time is found by integrating the Norton Law expresssion with time using the stress given from the RR analysis.

$$\varepsilon_c(t) = \int_0^{t_f} \dot{\varepsilon}^c \, dt = \int_0^{t_f} B_c(\ _{RR})^{N_c} \, dt \qquad \text{(Eq. 5.10)}$$

where $\varepsilon_c(t)$ is the creep strain as a function of time, t_f is the time interval to advance the crack, and σ_{RR} is the time-dependent stress given by the RR singularity. The result of integrating equation 5.10 is:

$$\varepsilon_c(t) = \left(\left(\frac{.29 \, K^2}{E \, r} \right)^{N_c} B_c \; (N_c+1) \; t \right)^{(1/(N_c+1))} \qquad \text{(Eq. 5.11)}$$

Equation 5.11 predicts the creep strain ahead of the crack, but for short times the accumulation of strain is very fast resulting from the infinite stresses predicted at t=0 by the RR singularity.

The model calculates the creep strain for each element ahead of the crack tip within the plastic zone. When the strain in an element reaches the critical creep fracture strain (ε_{crit}) the crack advances by one element.

For each element a transition time for $\sigma_{RR} = \sigma_{HRR}$ is calculated and this time is used to calculated a transition strain. This transition time given by equation 5.9 becomes t=0 and is combined with the calculation of creep strain with time in equation 5.11 to calculate a transition strain:

$$\varepsilon_c(t_{transition}) = \frac{.29\ K^2}{r\ E\ \sigma_{t=0}} \qquad \text{(Eq. 5.12)}$$

It is interesting to note that this strain is independent of B_c, N_c, and time. This transition strain must be subtracted from the calculated creep strain to compensate for the over-prediction in stress as short times by the RR singularity.

The time increment to advance one element is calculated as:

$$\Delta t = \left\{ \frac{\varepsilon_c(t_{tran}) + \varepsilon_{crit} - \varepsilon_i}{\left\{ \left(\frac{.29\ K^2}{E\ r} \right)^{N_c} B_c\ (N_c+1) \right\}^{(1/(N_c+1))}} \right\}^{(N_c+1)} - t_{transition}$$

(Eq. 5.13)

where ε_{crit} is the critical strain for fracture and ε_i is the accumulated strain in that element from previous iterations. (note: $\varepsilon_i = 0$ for the first jump) This is graphically illustrated in figure 5.2.

The creep strain for each element ahead of the crack tip is calculated and will accumulate. The plastic zone size, the change in K with advances in crack length, and load history will have a strong effect on the predicted creep crack growth rate.

The creep strain in an element ahead of the crack tip is calculated as:

$$\varepsilon_c(\Delta t) = \left[\left(\frac{.25\ K^2}{E\ r}\right)^{N_c} B_c\ (N_c+1)\ (\Delta t + t_{trans.})\right]^{(1/(N_c+1))} - \varepsilon_c(t_{trans.}) \quad \text{(Eq. 5.14)}$$

Creep strain accumulates only for elements within the plastic zone. Elements outside the plastic zone are assumed to accumulate negligible creep strain as a result of the smaller stresses in the elastic region. However, at low values of K the creep in the elastic region may become significant. The stresses are reset to the calculated stresses at t=0 given by the HRR singularity for the new crack length. Once the stresses are reset the entire process begins again for the next jump in crack length.

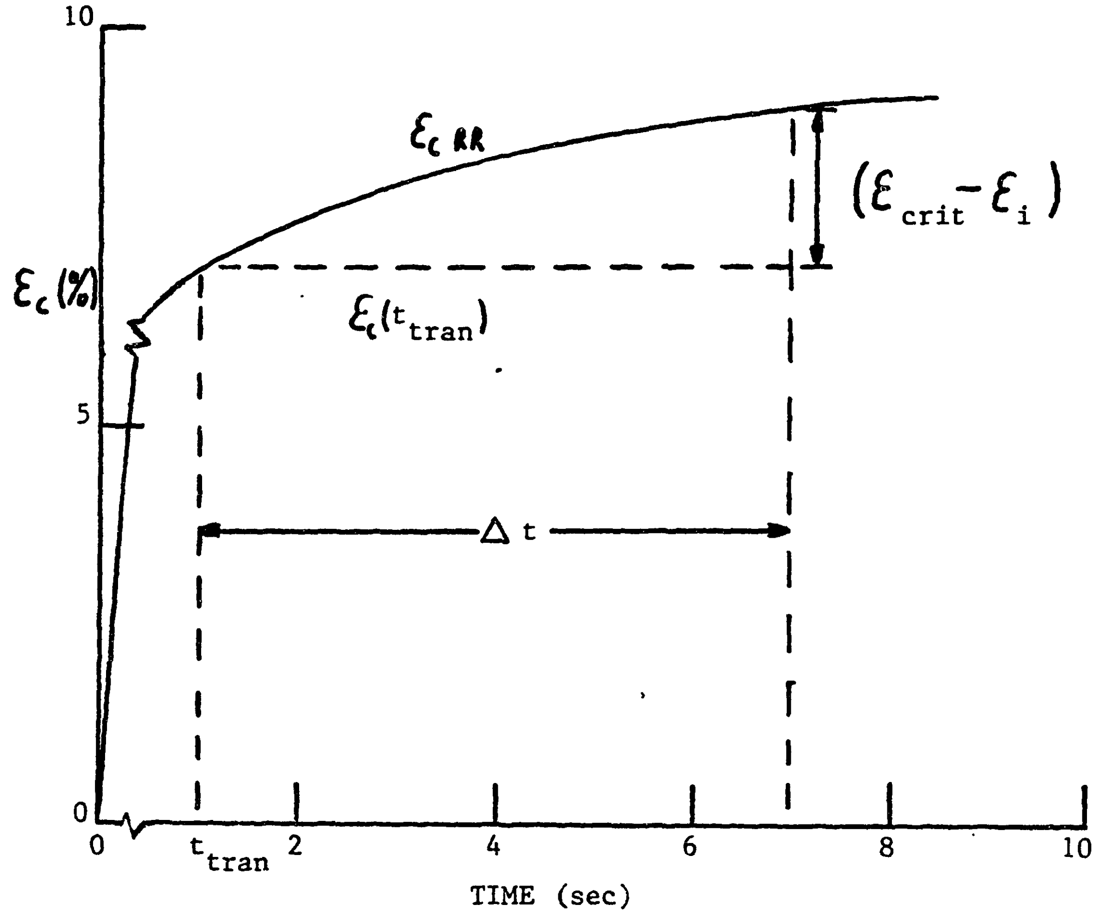

FIGURE 5.2) Schematic representation of the time for a crack advance in CCG, Δt.

5.3. The Effect of Oxygen

Oxygen diffuses ahead of the crack and embrittles the grain boundaries. This results in a loss of creep ductility and an increase in creep crack growth rate. The decrease in fracture ductility in air is observed to vary from alloy to alloy. In addition to a change in ductility, a change in fracture path occurs from prior powder boundaries to grain boundaries. This decreases the element size and results in an increase in the creep crack growth rates. The critical strain for an inert environment is obtained from short time creep-rupture tests by multiplying the minimum creep rate and the time to failure. This is the critical strain given by the Monkman-Grant relationship (100). In air the ductility is determined by fitting the predicted CCGR to the actual CCGR. The required change in ductility for each alloy is given in table 5.1.

TABLE 5.1

Alloy	$\frac{\varepsilon_{crit/air}}{\varepsilon_{crit/argon}}$	$\frac{\text{w/o B in G.B.}}{\text{w/o B in G.B. Astroloy}}$
Astroloy	1.0	1.0
MERL-76	0.2	.30
IN-100	0.71	.70
RENE-95	0.1	.26

The ratio of the grain boundary concentration of Boron to the grain boundary concentration of Boron in Astroloy is also presented. This expression shows the relative amount of boron per unit of grain boundary volume. The weight percent B per unit grain boundary volume is proportional to the w/o B in the bulk times the average grain size divided by the grain boundary thickness (δ). Table 5.1 is graphically illustrated in Figure 5.3.

Woodford and Bricknell (22, 30, 101) have shown that additions of as little as .1 w/o B added to Ni-200 or IN-738 will totally eliminate the embrittling effect of oxygen. The alloys with a large amount of boron per unit area of grain boundary have less of a reduction in creep ductility than an alloy with less boron. The concentration of boron on the grain boundaries was found to be 1000 times greater than in the bulk for PM/HIP Rene-95 as determined by Auger Spectral analysis. This indicates that most of Boron segregates to the grain boundary. Other elements which segregate to grain boundaries such as carbon, sulfur and zirconium should also have an influence on the creep crack growth rates which is a process of grain boundary fracture.

5.4. Predictions of Creep Crack Growth Rates

The model was used to predict the CCGR for the four alloys studied. The predicted and actual results are shown for both the air and the argon CCGR results in figures 5.4

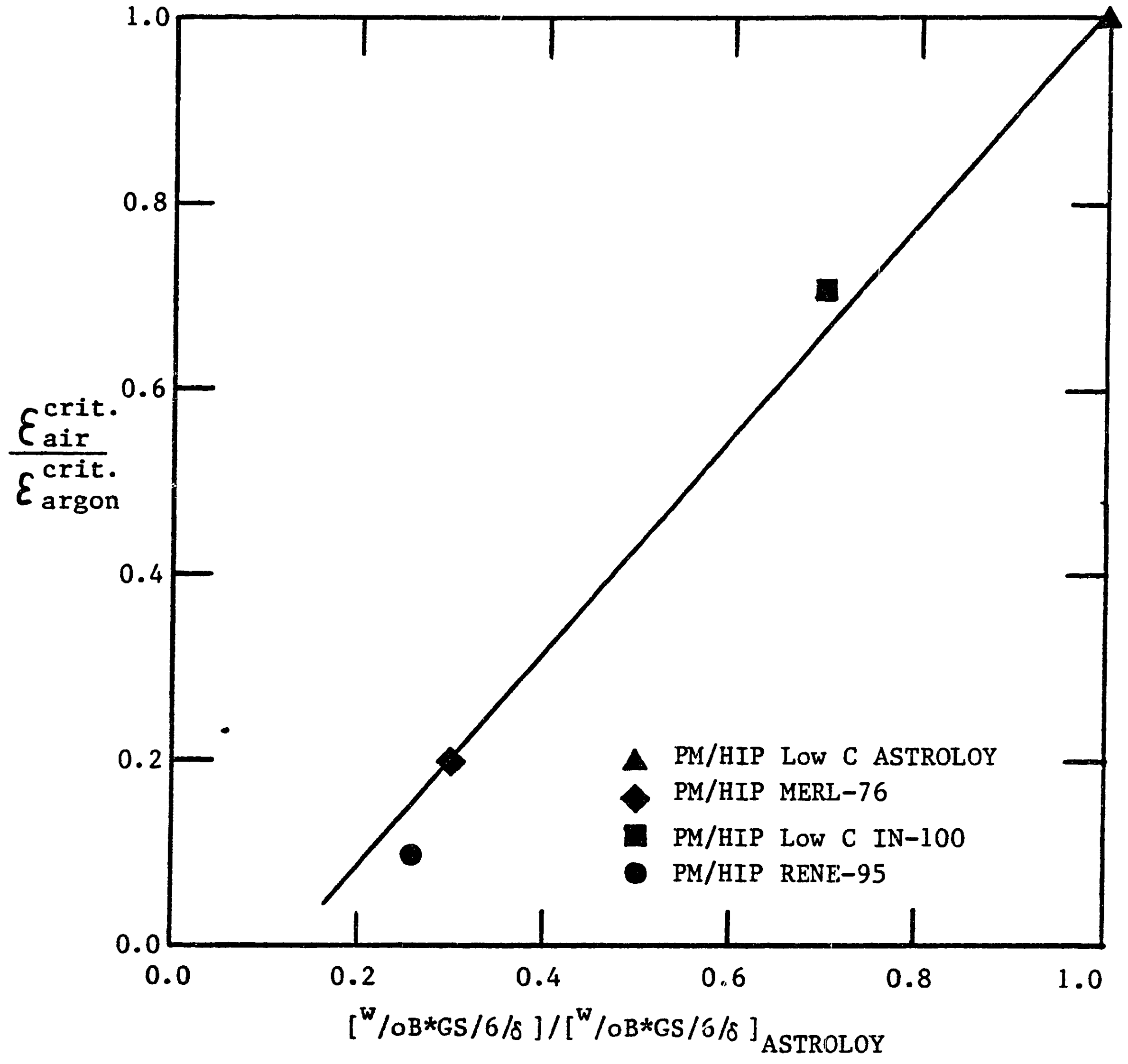

FIGURE 5.3) Ratio of the critical strain in air to the critical strain in argon versus the ratio of the grain boundary concentration of boron in the alloy to that in ASTROLOY. (δ=Grain Boundary Thickness,assumend to be a constant for all the alloys; GS=Grain Diameter). Assuming the boron in the bulk segregated to the grain boundaries the amount of boron will form a zone 17 mono-layers thick in PM/HIP Low C ASTROLOY.

to 5.7 for Astroloy, MERL-76, IN-100, and RENE-95 (60 mesh) respectively.

The model predicts the experimental results within a factor of 2 for all the alloys. The predicted results show an initial transient until damage is established throughout the plastic zone. The variation in the slope of the da/dt versus K plot is a result of the increasing number of elements accumulating strain (damage) as the plastic zone size increases. This effect varies from alloy to alloy because the variation in grain size leads to a variation in the number of elements within the plastic zone changes. Damage is assumed to accumulate only in the region of plastic deformation.

5.5. Effect of Critical Parameters

5.5.1. Effect of Critical Strain to Fracture

Increasing the critical strain results in an increase in the time to accumulate this (ε_{crit}) strain and therefore decreases the predicted CCGR. The model predicts the relationship between critical strain and da/dt is non-linear and for larger values of the critical strain the CCGR becomes exponentially smaller.

Figure 5.8 shows the effect of varying the critical strain on the CCGR predicted for Astroloy in air, at K=50 MPa $\sqrt{m}$. The CCGR is determined for a simulated constant K test after a sufficient number of crack advances for the

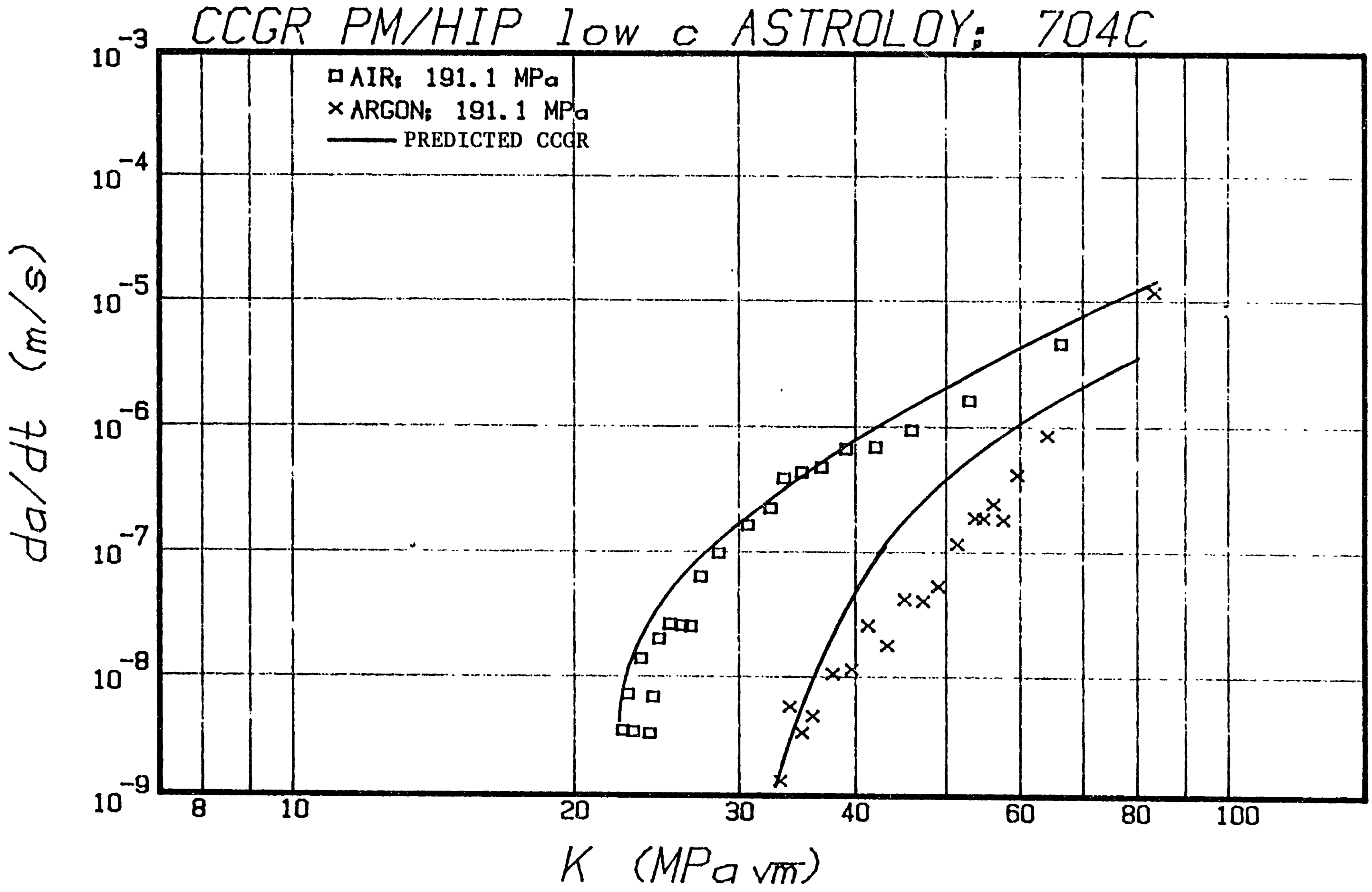

FIGURE 5.4) Predicted CCGR for PM/HIP low C ASTROLOY test in air and in argon at 704°C.

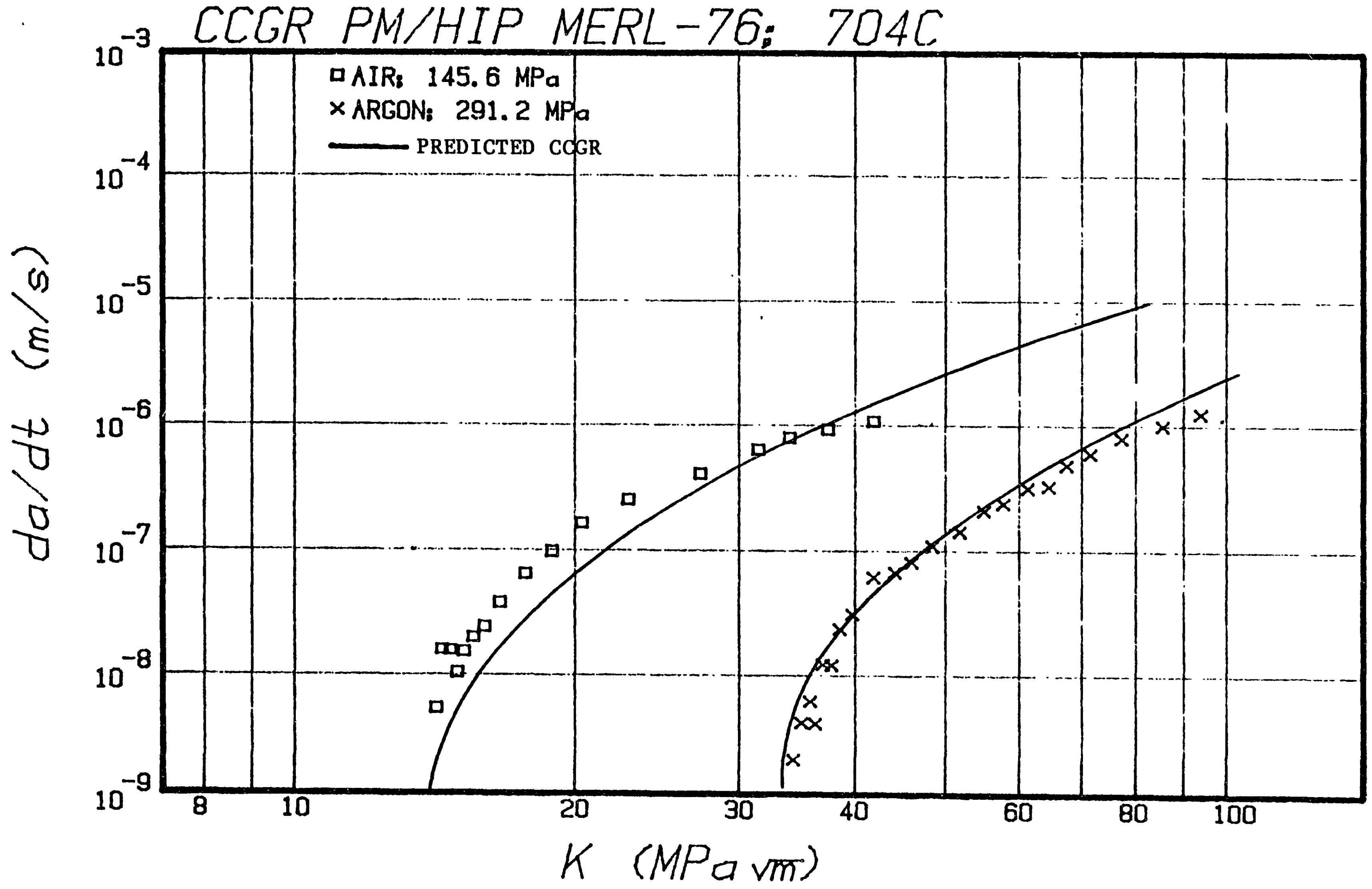

FIGURE 5.5) Predicted CCGR for PM/HIP MERL-76 tested in air and in argon at 704^{o}C.

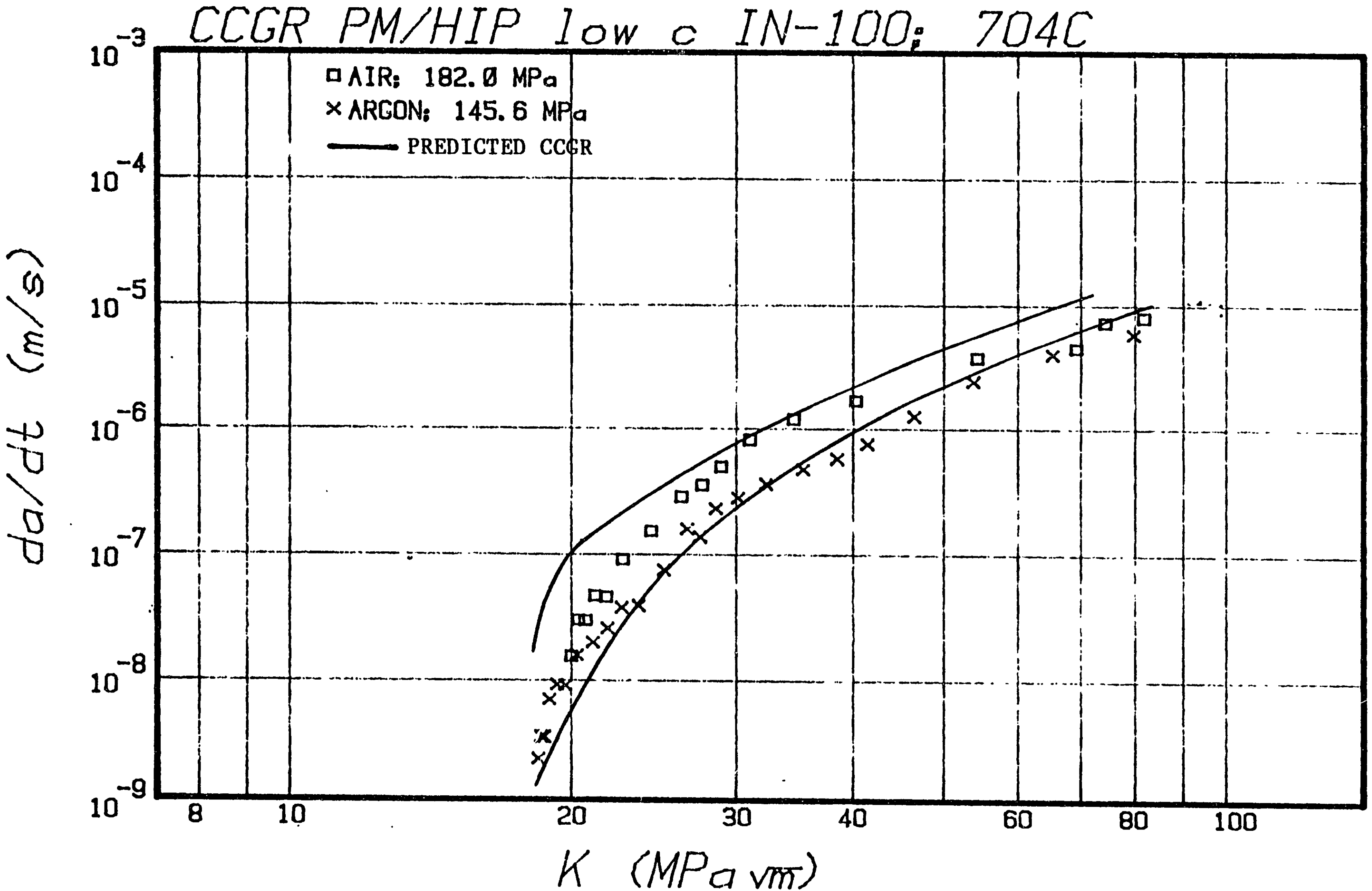

FIGURE 5.6) Predicted CCGR for PM/HIP low C IN-100 in air and in argon at 704°C.

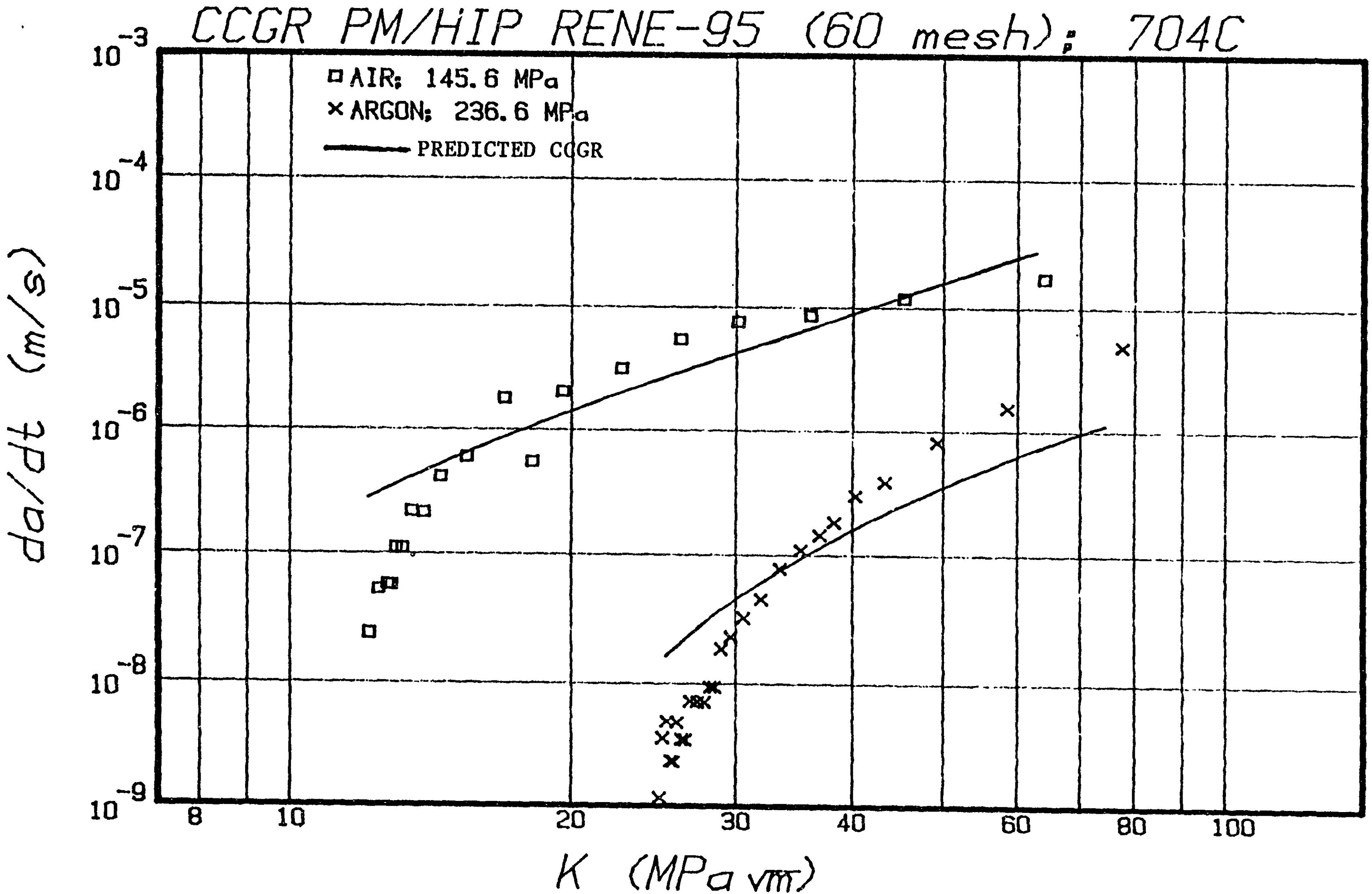

FIGURE 5.7) Predicted CCGR for PM/HIP RENE-95 (60 mesh powder) in air and in argon at 704°C.

CCGR to become constant. The number of crack advances is on the order of the plastic zone divided by the grain size. The slope of the steady state creep crack growth rate $(da/dt)_{ss}$ versus critical strain plot becomes ever steeper with increasing strain. For a small critical fracture strain the slope of figure 5.8 is -1. A slope of -1 results from the fact that for fast creep crack growth rates the stresses at the tip of the crack have little time to relax.

5.5.2. Effect of Grain Size

The effect of grain size on CCGR predictions is taken into account by changing the element size or crack step size. This will cause changes in both the slope of the CCGR versus K curve and in the magnitude of the CCGR predicted as a result of stress at each element node. Figure 5.9 shows the effect of grain size on the predicted constant K CCGR. The curve is similar to figure 5.8 with the constant K creep crack growth rate exponentially decreasing with increasing grain size.

The predicted effect of changing grain size on the CCGR versus K curve for PM/HIP Astroloy tested in air is shown in figure 5.10. The larger grain size resulted in a higher slope and a lower creep crack growth rate. The change in slope resulted from the number of elements which accumulated damage. The CCGR will increase with the number of elements within the plastic zone. However, the CCGR is lower as a result of a decrease in the rate of creep strain accumulation with increasing r as given by equation 5.11.

5.6. Constant K Calculations

The creep crack growth rate for constant K tests has been predicted and is shown in figure 5.11. for PM/HIP Astroloy in air. The plot illustrates how the accumulation of strain ahead of the crack tip affects the creep crack growth rate. The crack growth curves have an initial transient until a sufficient number of crack advances has occurred to bring the crack growth rate and the damage accumulation process to a dynamic equilibrium. This equilibrium should correspond to an upper limit for the creep crack growth rate in an increasing K test. When K is constant, an element ahead of the crack experiences the longest time in the region of plastic deformation and therefore accumulates the most creep strain.

5.7. Effect of dK/da on CCGR

The creep crack growth has been modelled as a process of damage accumulation ahead of a crack tip. Therefore, the load history an element experiences before the crack advances through it will become important. In an increasing or decreasing K CCGR test the rate of change of stress intensity factor with crack advance, dK/da, becomes important. A situation in which the rise in K with each crack advance becomes so large as to not allow the dynamic

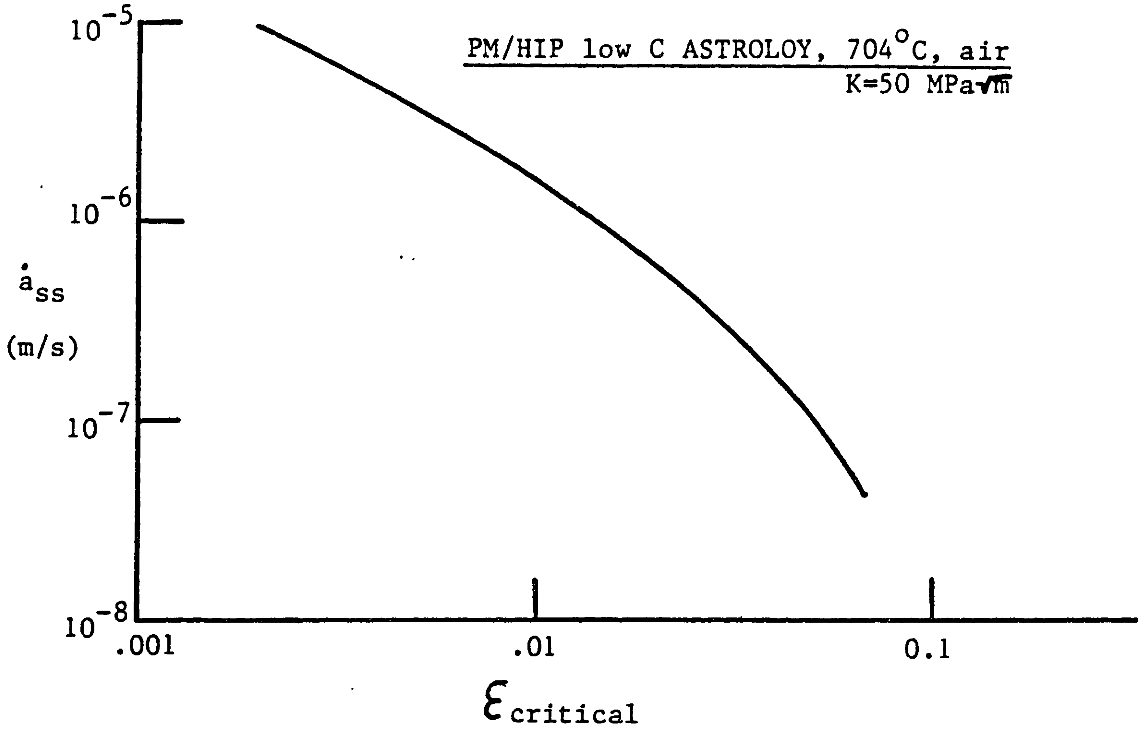

FIGURE 5.8) Predicted effect of $\varepsilon_{critical}$ on the CCGR of a PM/HIP Superalloy at 704°C.

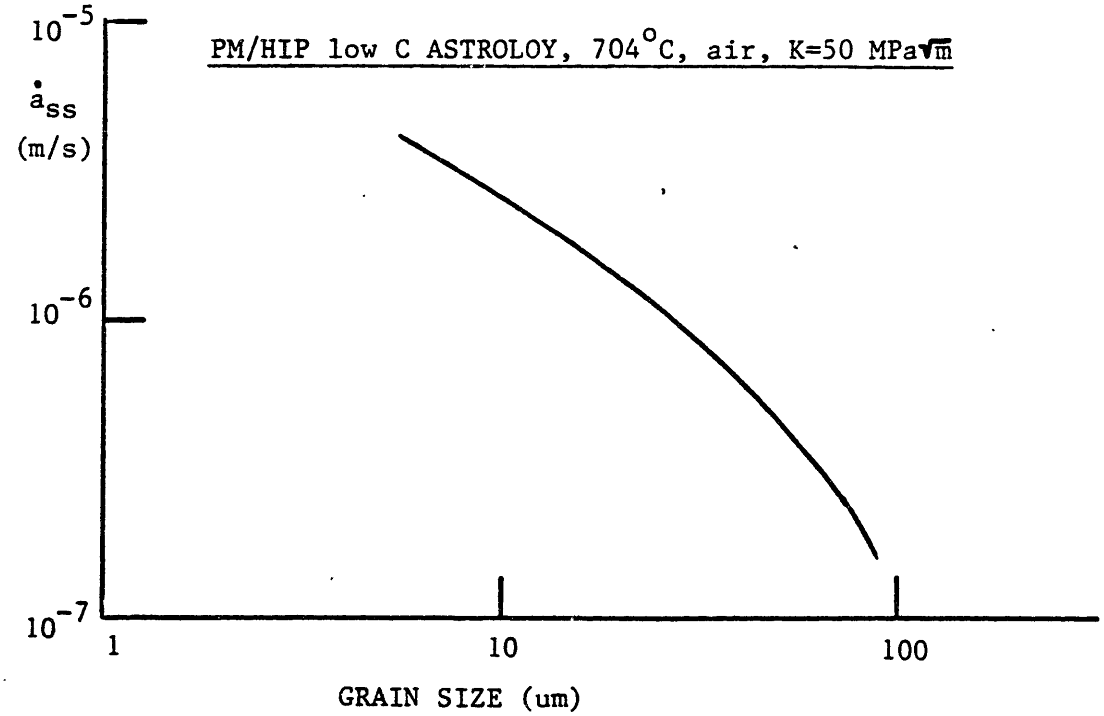

FIGURE 5.9) Predicted effect of grain size variations on the CCGR of a PM/HIP nickel-base superalloy at 704°C.

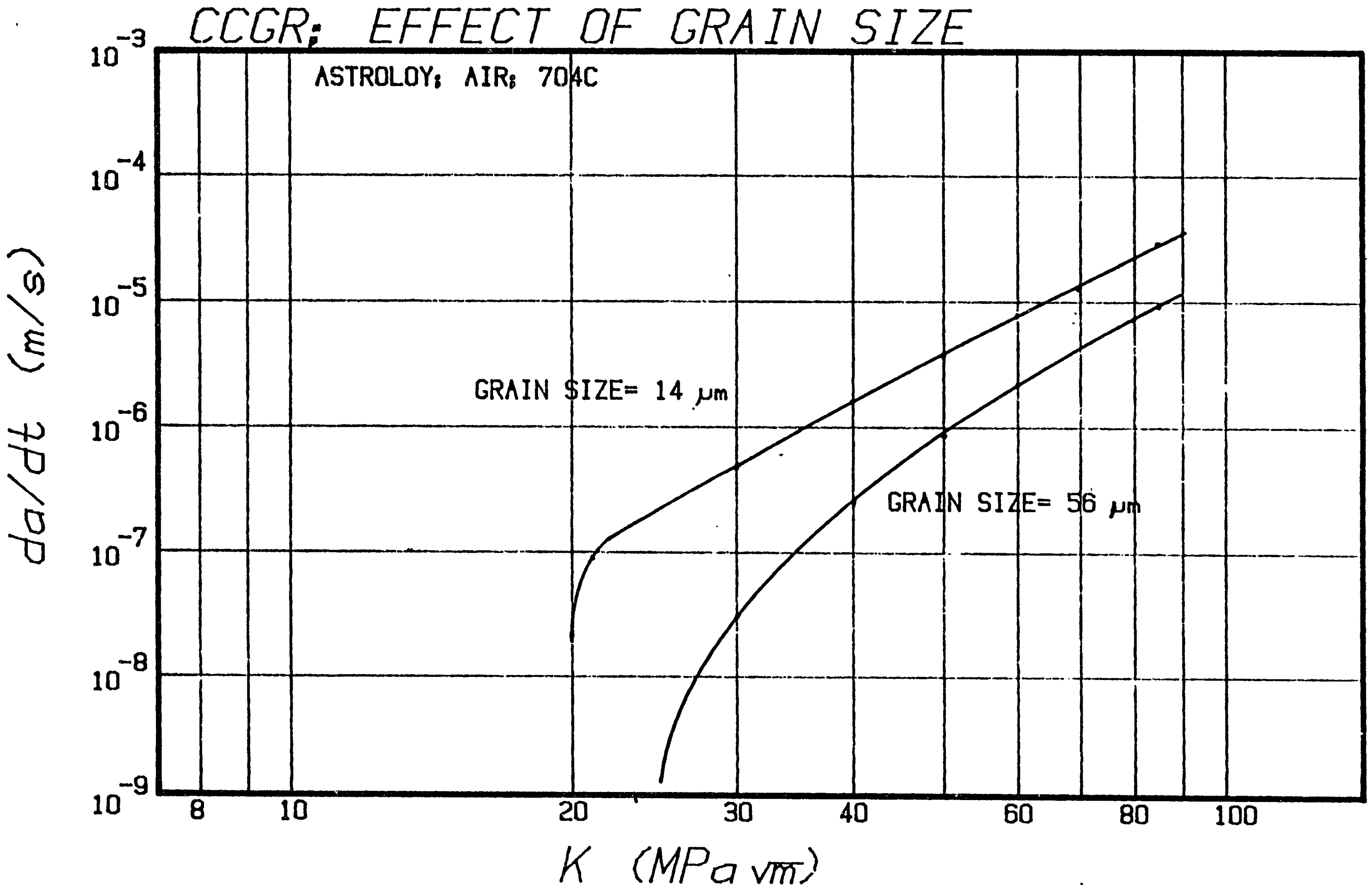

FIGURE 5.10) Predicted effect of grain size on the CCGR of PM/HIP low C ASTROLOY in air at 704°C.

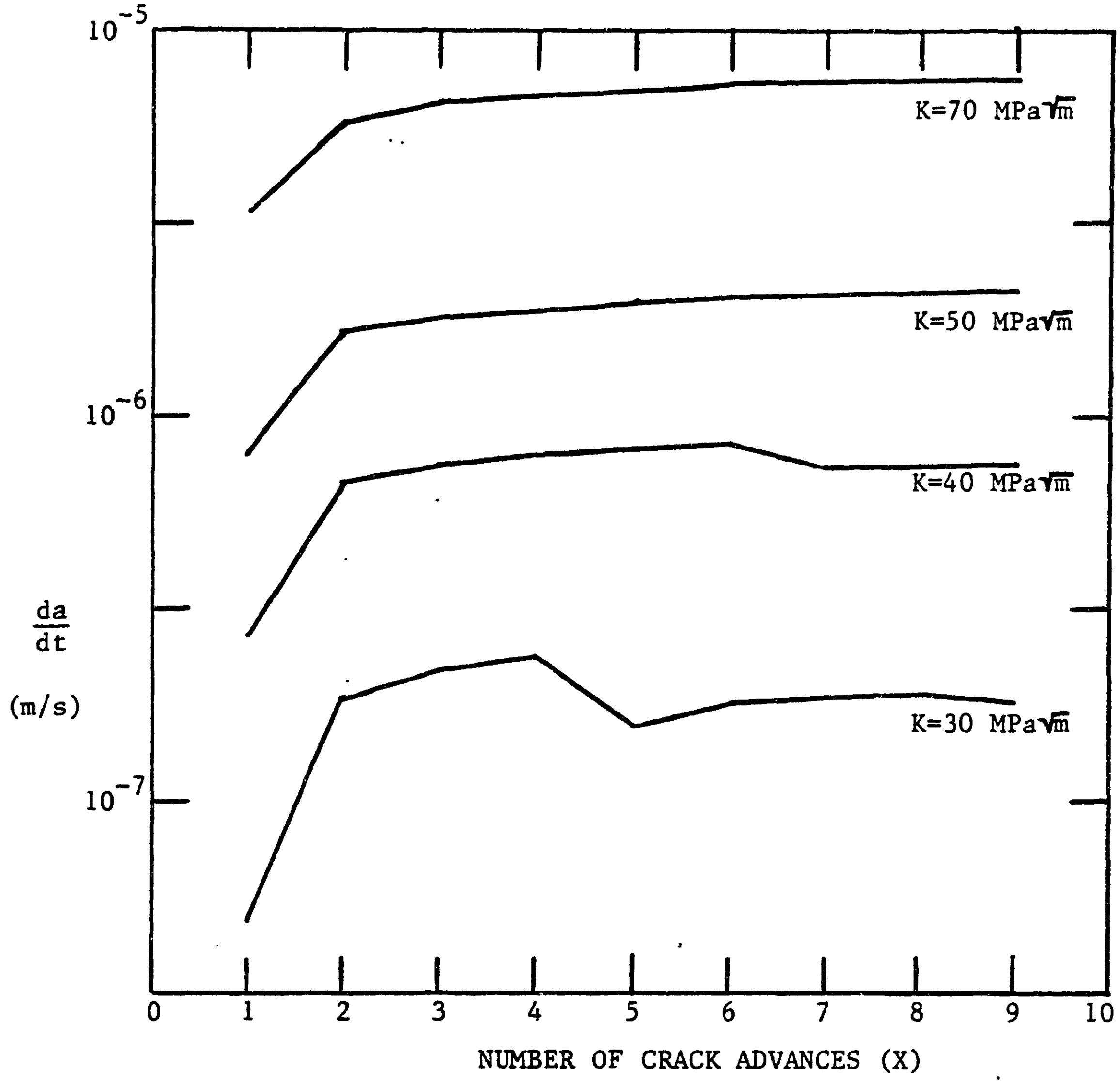

FIGURE 5.11) Predicted CCGR versus the number of crack advances for a constant K test. (based on data for PM/HIP low carbon ASTROLOY at 704°C in air.)

process of strain accumulation to reach equilibrium. This will result in the prediction of a different creep crack growth rate than is actually possible at a given K. This is illustrated in figure 5.12 for CCGR predictions on PM/HIP Astroloy in air at 704 °C. A careful examination of test specimens and procedures is recommended to avoid a large dK/da or a large initial K which will give a non-conservative creep crack growth rate.

The effect of not reaching equilibrium as a result of load history will become extremely important in the prediction of creep-fatigue interactions at high temperature. This process, though noted, will not be discussed here.

5.8. Effect of Temperature and Yield Strength

The effect of temperature on the predicted CCGR versus K curve is illustrated in figure 5.13 with the results obtained by Huang (63) for PM/HIP Astroloy at 650 °C and 760 °C. Temperature changes result in changes in the creep strain rate and a change in the yield strength. Ni-base alloys will maintain a high yield strength at high temperature and will increasethe secondary creep rate with temperature. This will result in a large increase in CCGR. The creep rate for Astroloy is given below (Huang(63)):

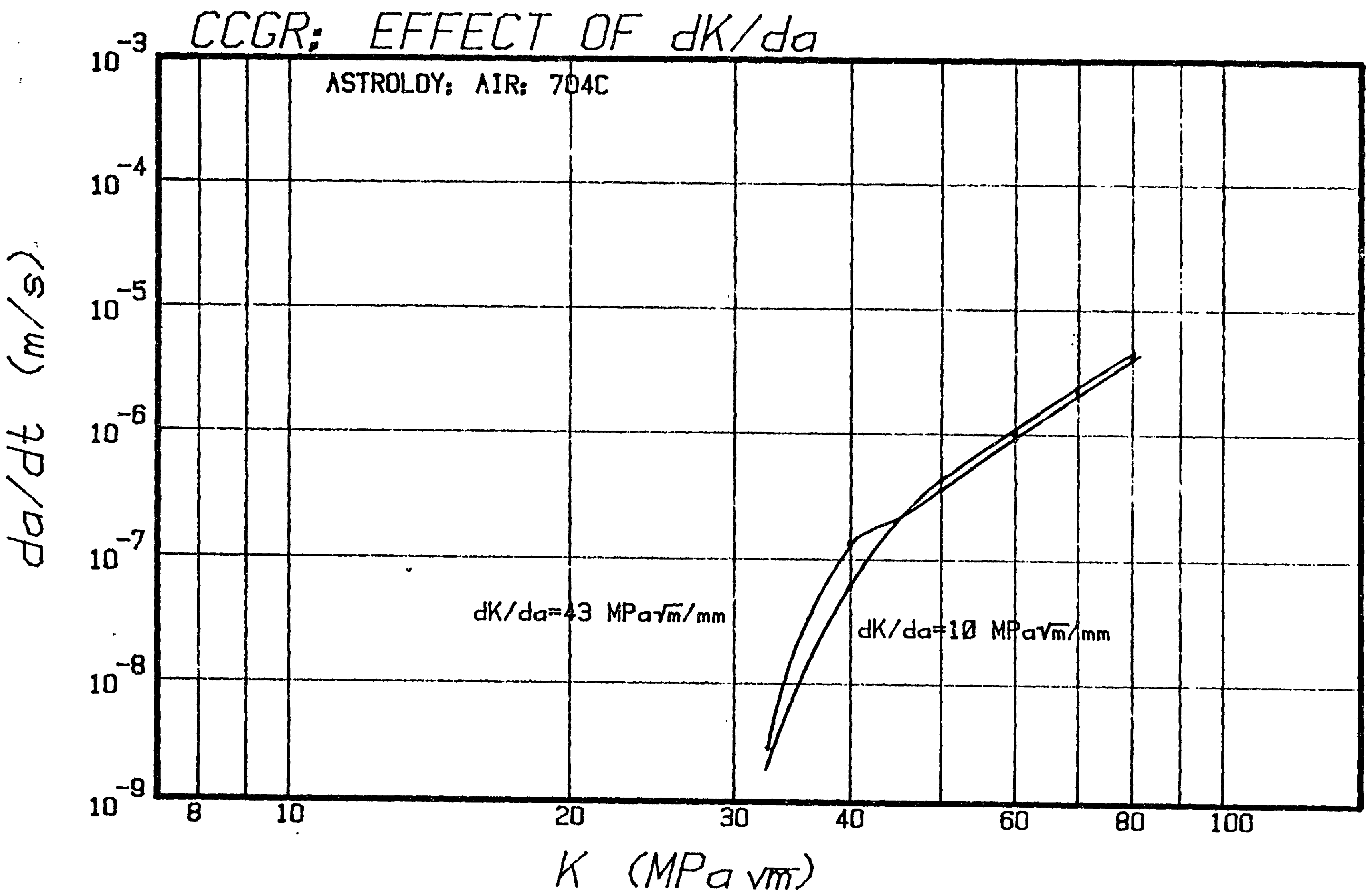

FIGURE 5.12) Predicted effect of dK/da on the CCGR of PM/HIP low C Astroloy in air at 704°C.

$$\dot{\varepsilon}_s(\text{sec}^{-1}) = \left(\frac{\sigma(\text{MPa})}{14.8}\right)^{12.31} \exp\left[\frac{-122.2\ (\text{Kcal}\cdot\text{mole}^{-1})}{R\ T}\right]$$

(Eq. 5.15)

The changes in $\dot{\varepsilon}_S$ for Astroloy account for the change in CCGR between 650^{0}C and 760^{0}C.

As yield strength decreases the predicted CCGR also decreases as a result of a lower stress in the plastic zone ahead of the crack. The effect of varying Y.S. is illustrated in figure 5.14 for the predicted CCGR of PM/HIP Astroloy at a constant K=50 MPa$\sqrt{m}$. The creep rate depends strongly on stress, and a small decrease in yield strength results in a large decrease in the CCGR. This result has been observed, but not reported, by industrial research groups. The process of reducing yield strength to decrease creep crack susceptibility is refered to as "de-tuning" an alloy.

The yield strength from hot tensile tests will vary with strain rate at temperatures where creep deformation is possible. Faster strain rate tests have a larger value of yield strength. Therefore, the value of yield strength from tensile tests used in the model may not be totally accurate. However, all the tensile results were obtained at the same strain rate and should be self-consistant.

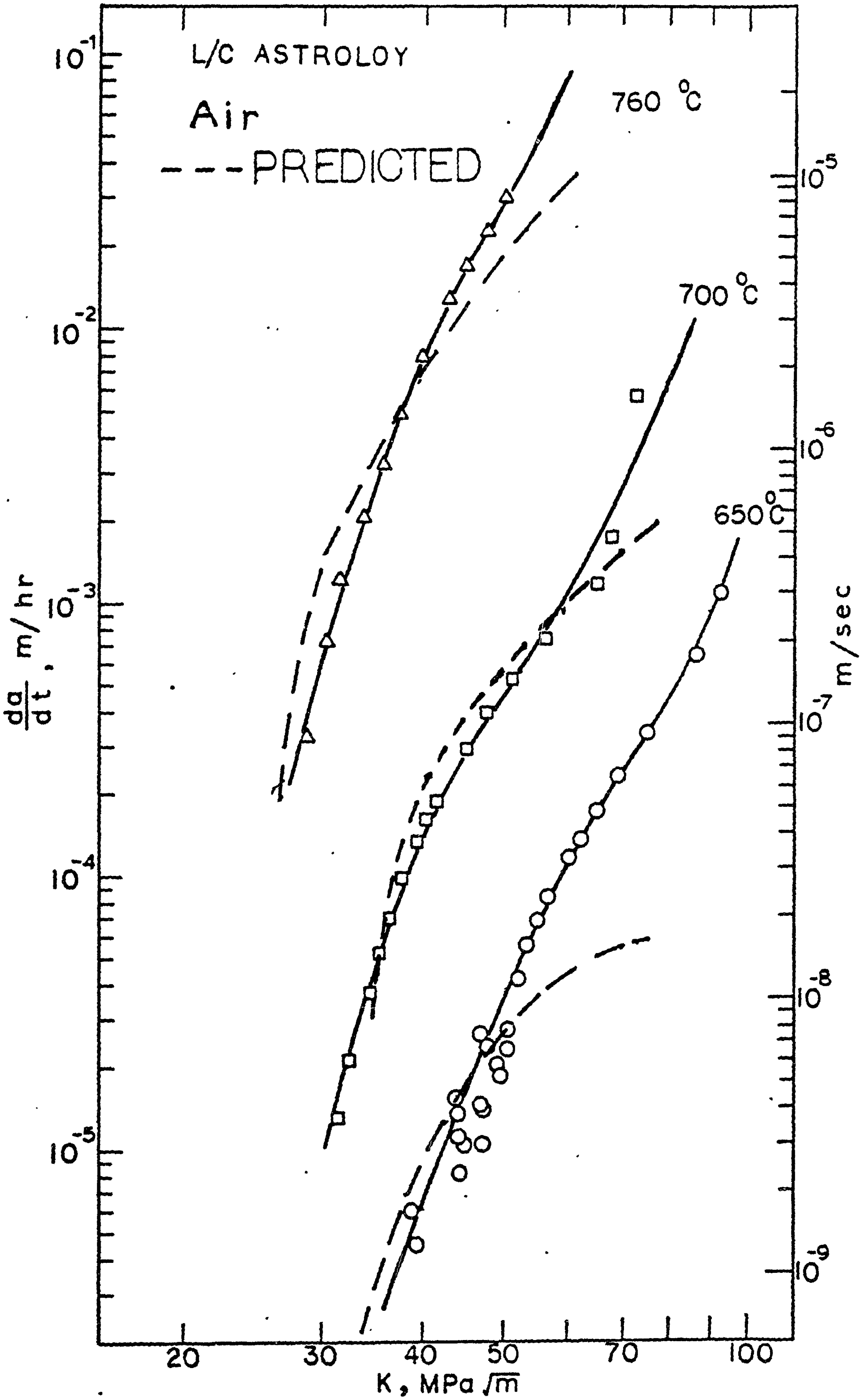

FIGURE 5.13) Predicted and actual CCGR results for PM/HIP low carbon Astroloy (ref. 63) for different temperatures.

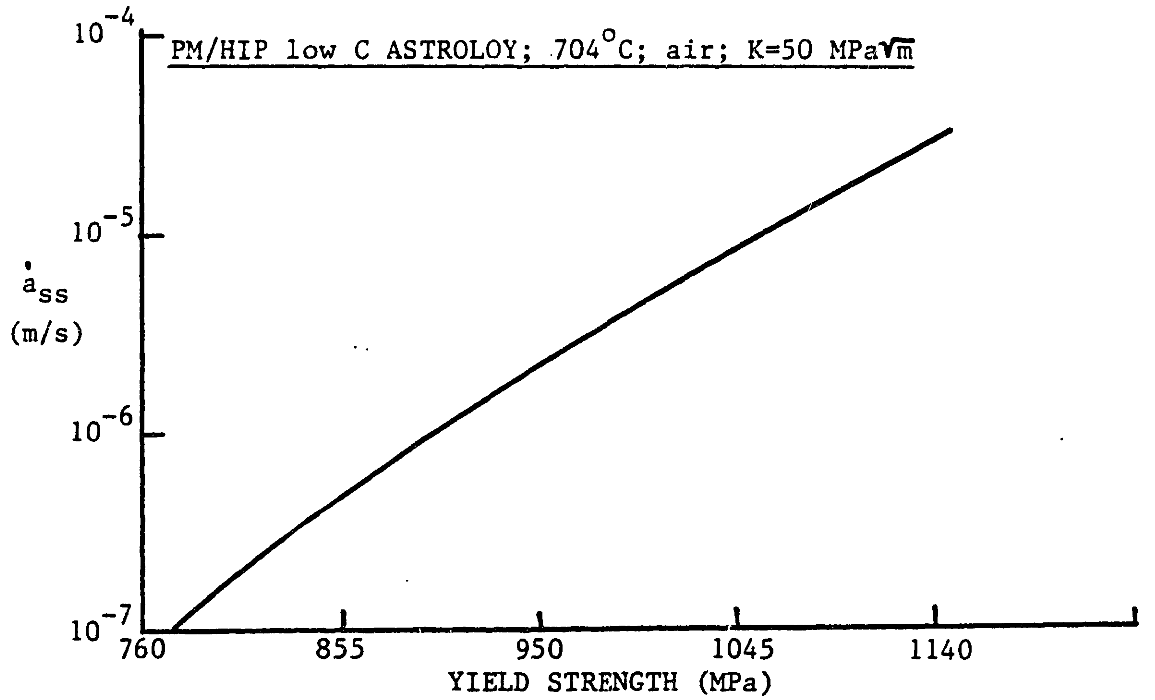

FIGURE 5.14) Predicted effect of yield strength on the steady state CCGR of a nickel-base superalloy.

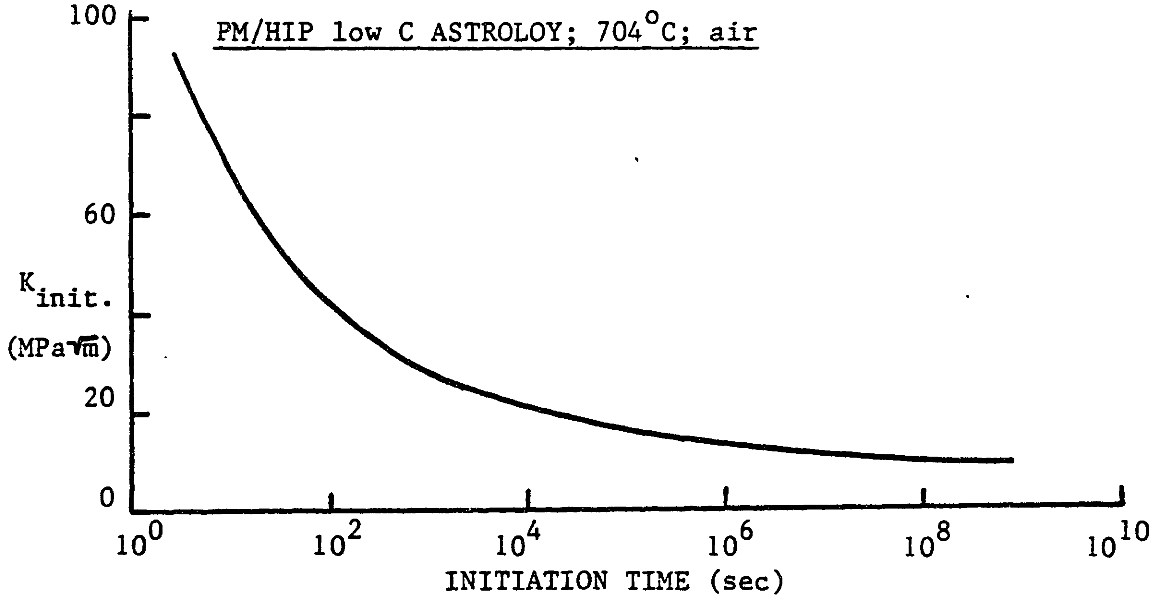

FIGURE 5.15) Predicted time to begin CCG in a nickel-base superalloy.

5.9. Predicted Creep Crack Initiation Times

The effect of initial stress intensity on the time to initiate creep crack growth from a fatigue precracked specimen has been reported by Floreen (50), Bain (102), Charpigny (103). It is found that as initial K decreases the time to initiate a creep crack becomes exponentially large.

The model can be used to predict the time to initiate crack growth from a sharp notch by determining the time for the first crack advance. Figure 5.15 shows the predicted results obtained for PM/HIP Astroloy in air as initial K versus time to initiation. At low values of K the time to initiation becomes extremely long as a result of the rapidly reducing stresses at the crack tip. The behavior predicted is similar to what is observed.

6. DISCUSSION

6.1. CCGR Model

The computer model presented in chapter 5 predicts some surprising results for creep-brittle materials in a small scale yielding condition. These predictions are:

1) The apparent lower limit for creep crack growth occurs when the plastic zone ahead of the crack becomes less than half an average grain diameter;

2) The CCGR in the stage II region depends on the rise in K with crack advance;

3) The stage I CCGR observed is an initial transient and is not a unique function of K;

4) The CCGR of an alloy is a strong function of the yield strength and creep strain rate of a material;

5) Load history can affect creep crack growth rate; and

6) The time to initiate creep crack growth is a unique function of K.

The lower limit in K for CCG is predicted to be a function of the grain size. This lower limit, K threshold, for CCG is given below:

$$K_{TH} \propto Y \sqrt{GS}$$

(Equ. 6.1)

where K_{TH} is the threshold stress intensity for creep crack growth, Y is the yield strength, and GS is the average grain diameter. Floreen (104) has shown that the initial stress intensity for failure in 100 hours at 704°C in IN-792 is a function $GS^{1/2}$. A true threshold may not exist for creep crack growth since there will always be some yielding at the tip of a crack and therefore some damage. The apparent limit for creep crack growth (K) should be given by equation 6.1.

The region of Paris Law type growth is affected by the dK/da for a specimen geometry. A Paris type relationship is given below:

$$da/dt = AK^{N}$$

(Equ. 6.2)

where A and N are material dependent constants. The variation in CCGR with dK/da results from a change in the load history for an element ahead of the crack. At a given K, an increase in dK/da results in less time for damage accumulation in an element ahead of the crack tip. The CCGR for a material is determined by the stresses ahead of the crack as characterized by K, and the load history for the element ahead of the crack tip. A series of curves can be drawn for the CCGR versus number of crack advances for a constant K test. The CCGR increases with each jump until a dynamic equilibrium occurs between the rate of crack advance and the rate of damage accumulation ahead of the crack. The equilibrium value represents the CCGR for a given constant K without any history effects. In actual CCGR tests the value for K increases with each crack advance. The CCGR at a value of K depends on the K-history which results from the dK/da in the specimen. This process is graphically illustrated in Figure 6.1. As the dK/da increases within a specimen, the CCGR versus K curve decreases. This effect will be pronounced in large grained materials and should be considered when measuring the CCGR for a material.

The stage I CCGR behavior measured is an initial transient which results from the fact that the crack tip is advancing through initially undamaged material for the first few jumps. This results in a lower CCGR upon loading which will quickly rise to the stage II region. Many of the results reported in the literature reflect primarily this initial transient, and any conclusions based on Stage I CCGR data are questionable.

The CCGR measured for all materials has been shown to be a strong function of the stress at the crack tip and the rate of creep strain accumulation (Chapter 5). Any changes in heat treatment or processing which alters either of these material properties will result in a marked affect on the observed CCGR behavior in a material.

The measured CCGR at a value of K depends strongly on the amount of creep deformation accumulated in the grains just ahead of the crack tip. Variations in the load history of a specimen or component which will affect the amount of

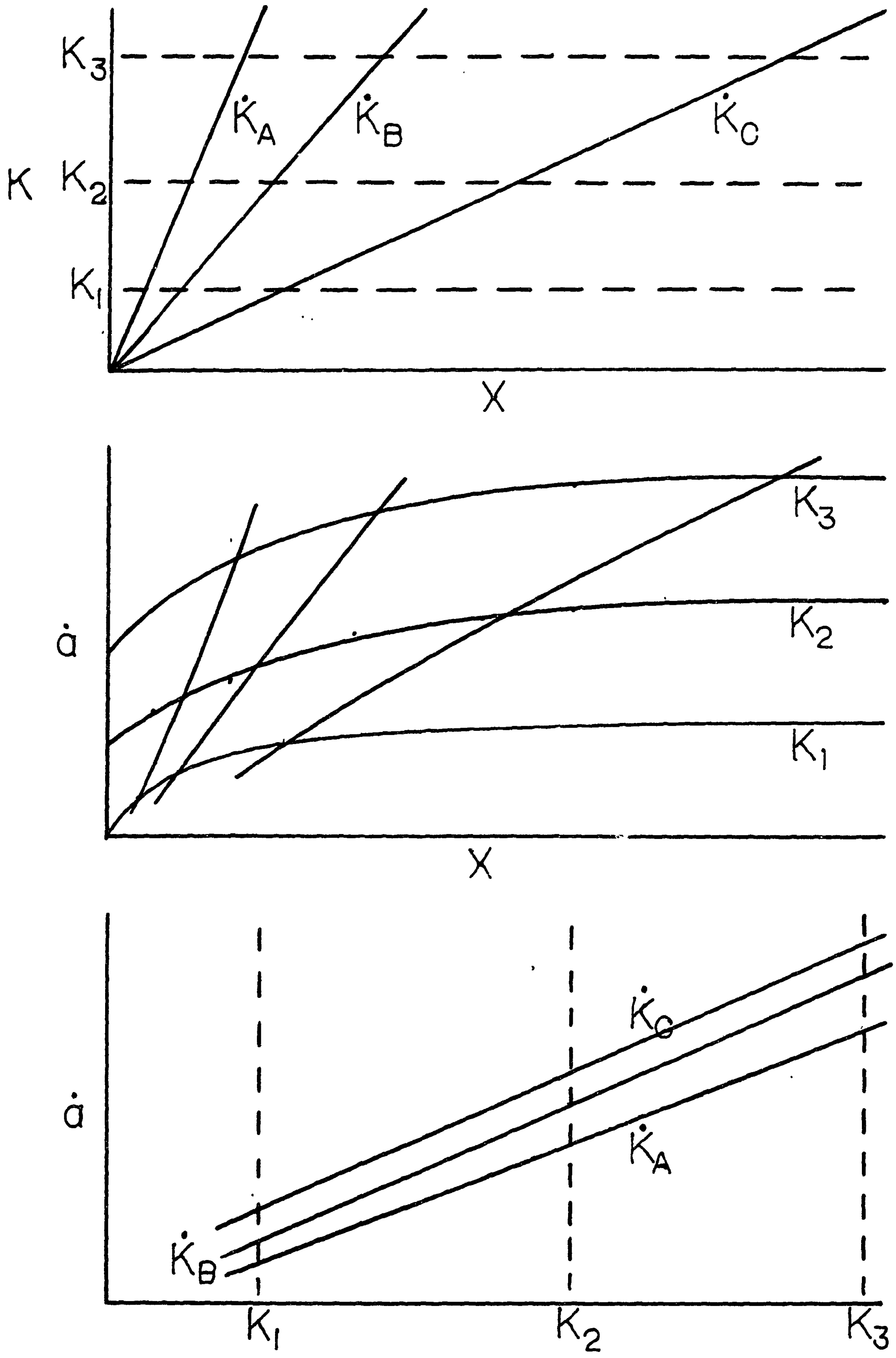

FIGURE 6.1) Schematic showing the effect of dK/da on CCGR results.

accumulated creep strain ahead of a crack will affect the creep crack growth rate. The crack growth rate depends on the amount of damage a grain receives from previous loadings which gives the material a "memory" of past loadings. A study on the effect of load history is vital if the interactions between fatigue and creep crack growth are the be understood.

As was shown in chapter 5, the time to initiate creep crack growth from a sharp crack depends strongly on the initial K. This result is important when one considers the interaction between creep crack growth and fatigue. If a fatigue crack advances through the damaged zone ahead of the crack tip in less time than is required to initiate creep crack growth for a sharp crack, then the crack should not exhibit significant time dependent behavior. The initation time becomes important when considering whether or not a fatigue crack will advance during a tensile hold period at a high temperature. Tensile hold periods are common in modern aircraft gas turbine components during flight.

6.1.1. Effect of Triaxiality

It has often been observed that creep crack growth is much slower in the plane stress condition than in the plane strain condition. The model presented in section 5 does not show any effect of stress state. The affect of a triaxial state of stress can be shown to change the creep crack growth rate of a material via changes in the value of the critical strain for fracture. Rice and Tracey (105) have shown that the critical strain to fracture a material is a function of the state of stress. The expression for the critical strain is given by:

$$\varepsilon_{critical} \propto \left(C \exp\left(\frac{3\ \sigma_H}{2\ \sigma_E}\right)\right)^{-1} \qquad \text{(Equ. 6.3)}$$

where "C" is constant for the material, σ_H is the hydrostatic stress, and σ_E is the equivalent stress. The plane stress and plane strain stress fields at a crack tip have been worked out by Hutchinson (72). The ratio of the critical strain for plane stress to the critical strain for plane strain as given by equation 6.3. is approximately 18. A reduction in the creep ductility for notched specimens versus smooth creep rupture specimens was shown to be significant by Dyson and Loveday (106) for Nimonic 80A at 750°C.

The effect of increasing the critical strain by a factor of 18 for PM/HIP Astroloy at 704°C in air to simulate plane stress CCGR is shown in Figure 6.2. The plane stress CCGR is much slower than the CCGR in plane strain. This behavior accounts for the crack tip tunnelling phenomenon observed in CCGR tests without side grooves.

6.1.2. Effect of OxygenConcentration

The model predicts the CCGR in air by a reduction in the critical strain and a change in the element size. The reduction in critical strain will result from any of the embrittlement mechanisms suggested in section 2.2., but the exact mechanism remains a mystery. A reduction in the element size in air CCGR tests results from the observed change in fracture path from predominantly prior particle boundaries in argon CCGR tests to predominantly intergranular fracture in air CCGR tests. The change in element size alone is sufficient to explain the increase in the air creep crack growth rate for Astroloy. The model assumes a constant reduction in the critical strain in air with creep crack growth rate which is not observed in all alloys. Tests in air on PM/HIP Astroloy indicate that the crack out runs the embrittling effect of oxygen at high da/dt. This change is reflected in the transition at fast CCGR to a prior particle boundary fracture path in the air tests.

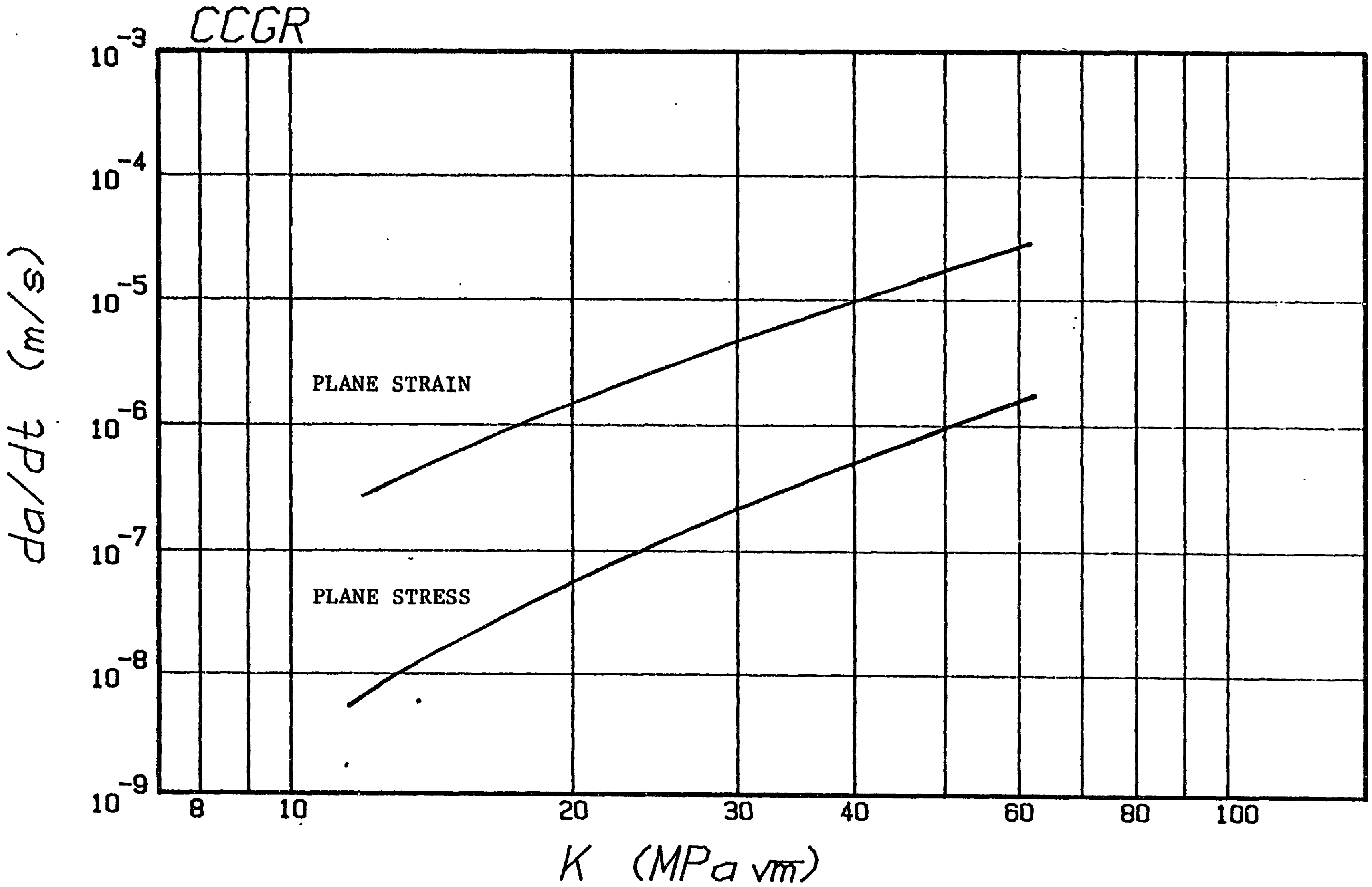

FIGURE 6.2) Predicted decrease in the CCGR of PM/HIP RENE-95 (60 mesh) in air at 704°C as a result of changing the state of stress.

6.1.3. Limitations of the CCGR Model

There are several points in the model which may give rise to errors in calculating the CCGR of a material. These include: 1) The procedure used to update the stresses upon crack advance; 2) The effect of strain rate on plasticity; 3) The estimation of the plastic zone size; 4) The effect of time independent plastic strain on CCGR; and 5) The effect of strain rate on yield strength.

The stresses ahead of the crack tip are updated to the calculated values given at t=0 which are by an approximation of the HRR singularity. The stresses are not reduced as a result of creep strain accumulation from previous iterations. This may result in an slight over-estimation of stresses at the crack tip and therefore an over-estimation of CCGR. This over-estimation should be small since the creep strains are generally small when compared with the plastic strain.

At high temperatures the strain hardening behavior of a material becomes a function of both strain and strain rate. The measured yield strength of a material increases with increasing strain rate. A change in yield strength would result in a considerable effect on the predicted CCGR for an alloy. All the tensile tests in this study were performed at the same strain rate, and therefore should be comparible and self consistant.

The plastic zone is calculated as $.1(K^2/Y^2)$. The scaling parameter for the plastic zone is 0.1. Estimations of plastic zone size vary with angle ahead of the crack tip, state of stress, and mode of loading. For mode I loading in plane strain estimates for the scaling factor vary from .018 to .32. (69) While 0.1 is a good estimate of the average scaling factor, it may not be the best. Changing the estimation of the plastic zone will affect the slope of the CCGR versus K curve, but such changes will be minor.

The model does not calculate any damage as a result of the time independent plastic strain ahead of the crack tip. Plastic strain has been shown to reduce the critical fracture strain by Nix (107). The effect of plastic strain on the critical strain may be a source of error in predicted CCGR results. At this time there exists no consistant way of predicting this damage.

The 0.2% yield strength for a material at high temperature varies with strain rate. The yield strength has a large affect on the predicted CCGR. Any change in yield strength will affect the CCGR. The yield strength of the alloys tested were obtained at the same strain rate (2%/minute) and should be self-consistant.

The various sources of error in CCGR prediction can be significant, but hopefully these errors are systematic and therefore act only as scaling factors which will adjust the predicted CCGR in a self-consistant manner. The fact that the model predicts the CCGR for the alloys tested based on measurable input parameters indicates that these errors are systematic.

6.2. CCGR of PM/HIP Ni-Base Alloys

The CCGR for a PM/HIP Ni-base alloy has been shown to vary considerably from alloy to alloy in both air and inert environments. The measured CCGR will vary as a result of test procedure, and environment. The alloys tested were all creep-brittle, and the conditions of small scale yielding apply. (Appendix III) Therefore, the stresses ahead of the crack tip are well characterized by K, and K becomes a natural parameter against which CCGR behavior is correlated.

6.2.1. Effect of test procedures

The CCGR in air for an alloy varied with the applied load and initial K. The stage II CCGR decreased with increasing load. The effect of applied load is a result of changes in the dK/da associated with changing load. The dK/da for the SEN specimens tested is given by:

$$dK/da = \frac{P}{\sqrt{\underline{B}\, B_N}\; W} \sqrt{\pi/a}\ \begin{array}{l}(.56-.345/W+26.5(a/W^2)-76.0(a^2/W^3)\\ +136.8(a^3/W^4))\end{array} \qquad \text{(Equ. 6.4)}$$

The dK/da varies only with load, "P", for a fixed a/w.

The CCGR tests exhibit a region of sharply increasing CCGR upon initial loading. This stage I region of growth is not unique and occurs for any initial K. Tests performed at high initial K resulted in the lack of a stage II region CCGR versus K. This indicates that the condition required to reach dynamic equilibrium at the crack tip were not acheived before the value of K_{IC} was reached.

The fact that the applied load and initial K will have such a profound effect on the CCGR results coupled with the effect of triaxiality on the CCGR indicates that most of the published results on CCGR for Ni-base alloys at high temperatures may have significant errors. Systematic tests with low dK/da, low initial K, and specimens which have been side grooved to avoid crack tip tunnelling are required to achieve accurate CCGR results.

6.2.2. Effect of Oxygen

The presence of oxygen acted to significantly increase the measured CCGR in all the alloys tested. In addition to increasing the CCGR, oxygen resulted in a change in the fracture path from prior particle boundaries to grain boundary cracking.

100 hour air exposure tests at 704^{0}C on 4 alloys indicated that the oxygen diffuses into the material along the grain boundaries to a considerable depth. Similar results have been obtained by Woodford and Bricknell (30) and Pineau (56) using Ni-base alloys. The results indicated that the alloys which had the highest effective diffusivity of oxygen were IN-100 and Rene-95 (60 mesh). These alloys also had the fastest CCGR in air. The depth of oxygen embrittlement in the time for one crack advance can be calculated from the following expression:

$$X = \sqrt{D_o \; GS/a}$$

(Equ. 6.5)

where X is the depth of oxygen embrittlement, D_o is the effective diffusivity of oxygen along the grain boundaries determined in section 4.5, "a" is the CCGR, and "GS" is the average grain diameter. Assuming a minimum depth of oxygen embrittlement ahead of the crack tip is required for accelerated fracture in air, equation 6.5 indicates that the maximum CCGR in air is proportional to $D_o \cdot GS$. Figure 6.3 shows the CCGR in air at 704°C and $K = 30\ MPa\sqrt{m}$ versus $D_o \cdot GS$. A good correlation of the CCGR data is observed, but the slope of the line is -.5 indicating the depth of oxygen embrittlement is not the only criteria for fracture. If the CCGR in oxygen is limited by the diffusion of oxygen and subsequent embrittlement, then when the diffusion of oxygen becomes rate limiting the slope of the stage II region of the CCGR versus K curves will be reached. A reduction of the Stage II CCGR slope from the predicted slope in air is observed in Rene-95 and to a lesser degree in IN-100 and Merl-76. While the change in slope may be partially due to the change in fracture path, these results indicate that the rate of oxygen diffusion and embrittlement does become a rate limiting step for CCGR in air. This behavior is very similar to the well known stress corrosion cracking phenomenon observed in aquious environments.

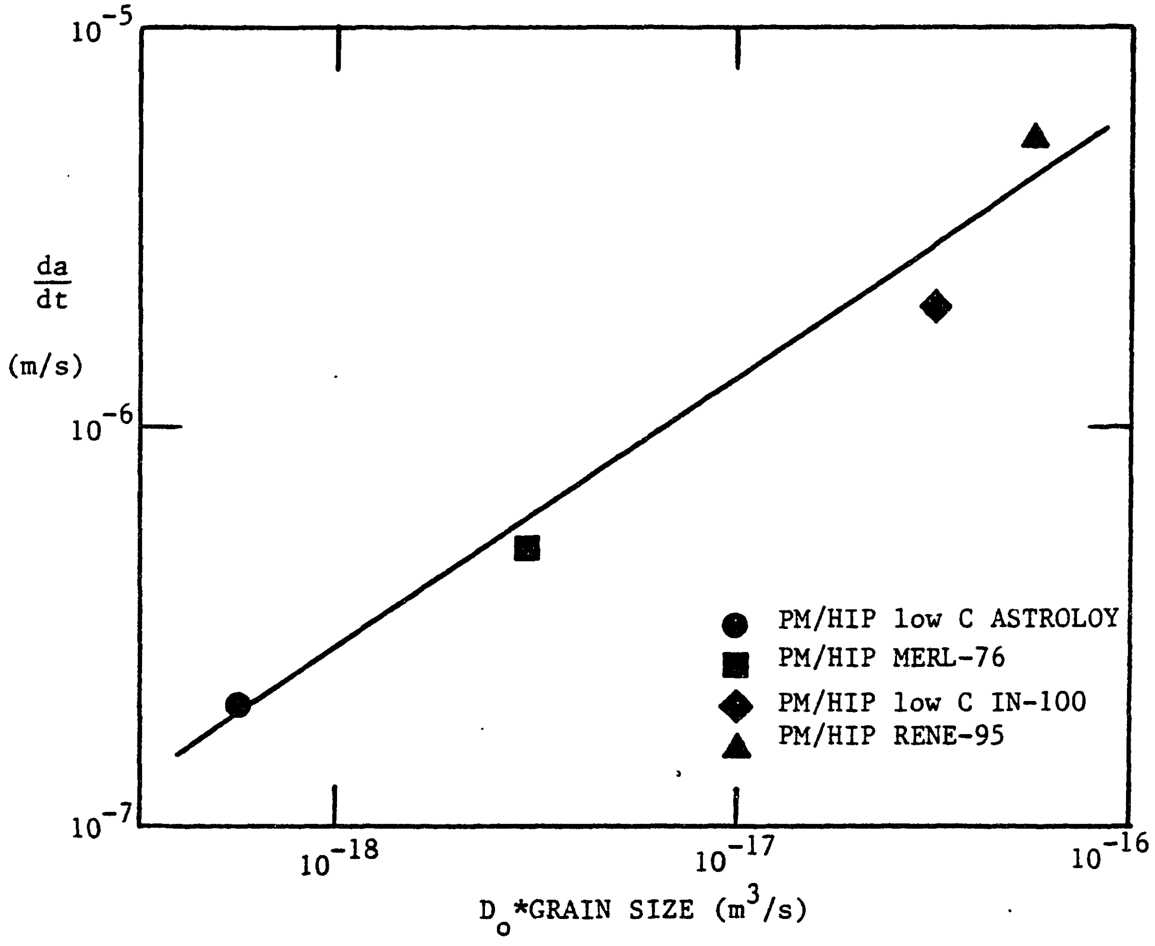

FIGURE 6.3) Comparison of the CCGR in air at 704°C, K=30 MPa$\sqrt{m}$ versus the effective diffusivity of oxygen * grain size for four PM/HIP Nickel-Base Superalloys.

Alloying additions such as boron, zirconium, and magnesium which inhibit the embrittlement of oxygen can be expected to reduce the CCGR measured in an oxygen containing environment.

The predicted CCGR upon initial loading in air is over-predicted by the model. This is most obvious in the preditions for Rene-95 (60 mesh) in air at 704°C. The over-prediction comes from the assumption of a constant, reduced critical strain in air. Actually some time will be required before oxygen can diffuse along the grain boundaries and embrittle the crack tip. Since this time is neglected in the model, an over-prediction of the CCGR will occur.

Some CCGR results in air for IN-718 by Pineau (56) indicate that the diffusion of oxygen down the crack to the crack tip may limit the availability of oxygen. These CCGR results indicate that as the initial crack length increases, the creep crack growth rate decreases for a given K. This would occur if diffusion of oxygen to the crack tip became the rate limiting step in oxygen embrittlement. In general, these effectswere not observed in the alloys tested.

6.3. Notched Stress Rupture Tests versus CCGR

The notched stress rupture (NSR) test indicates the time to failure for an alloy from creep mechanisms in the presence of a stress concentration. The fracture mechanism involves the initiation of cracks in the specimen followed by the propagation of a single dominant crack until K_{IC} is reached and fast fracture occurs. At high stresses the entire net section of the notched specimen goes plastic and failure usually occurs from subsurface cracks which initiate in the center of the specimen. (106) At lower net section stress, the failure results from surface cracks. These cracks link to from one dominant crack which propagates to failure. The lower stress fractures are usually brittle intergranular fractures. The presence of oxygen has been shown to significantly reduce the time to failure in nickel-base alloys. (5)

The NSR test at low net section stress can be thought of as a test which measures the time to initiate a creep crack. If crack initiation in the NSR test results from the nucleation, growth and coelescence of cavities in the stress field at the root of the notch, then the results of NSR tests can indicate the relative CCG behavior of different alloys and/or different heat treatments.

Figure 6.4 compares the CCGR at 704°C, $K=30\ MPa\sqrt{m}$, in air for 4 of the alloys tested versus the time to rupture from NSR tests performed at 675 MPa in air at 704°C. The NSR results for the alloys follow the same ranking as the CCGR results for the same 4 alloys. Astroloy was observed to have the longest time to rupture and the lowest CCGR while Rene-95 gave the shortest time to rupture and the highest CCGR. These results indicate that the NSR test may be a quick, simple and inexpensive test to compare the CCGR

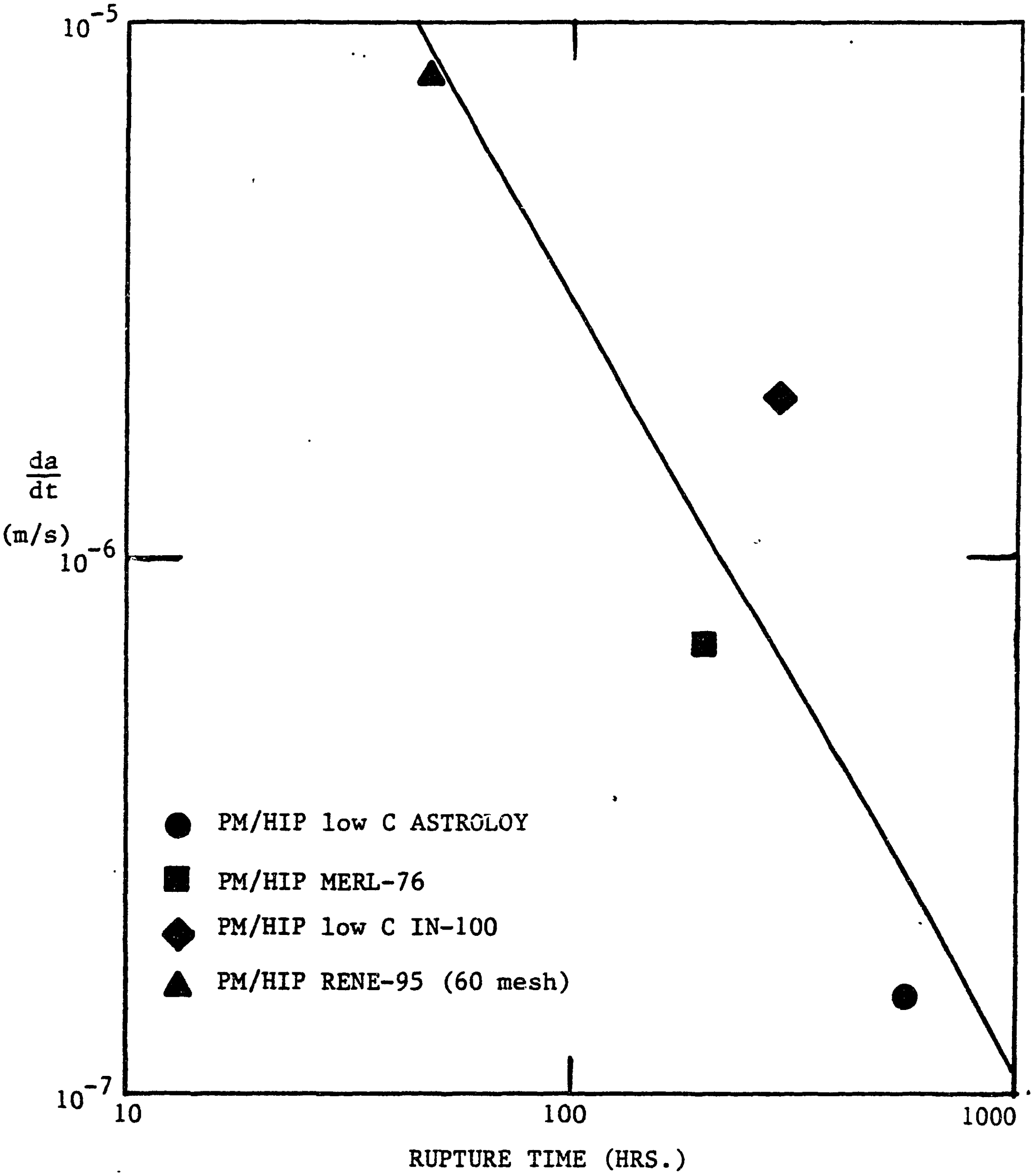

FIGURE 6.4) Comparison of the CCGR in air at 704°C, $K=30\ MPa\sqrt{m}$ versus the time to rupture a NSR specimen.

behavior of various alloys, heat treatments and processing changes.

7. CONCLUSIONS

1. Creep crack growth rates were measured for 4 Ni-base, γ -γ'; strengthened Ni-base superalloys at 704 °C in both air and in a 99.999% pure argon environment. The four alloys tested were all PM/HIP alloys and they included low Carbon Astroloy, Merl-76, Low Carbon IN-100, Rene-95 (60 mesh powder), and Rene-95 (120 mesh powder). The CCGR ranged from 10^{-9} m/s to 10^{-4} m/s and the stress intensity ranged from 10 MPa$\sqrt{m}$ to 120 MPa$\sqrt{m}$. The presence of oxygen during CCG resulted in an increase in the measured CCGR for a given K in all the alloys tested. The increase in CCGR varied for the alloys tested, but Rene-95 (60 mesh) had the largest increase in CCGR and Low Carbon IN-100 had the smallest increase in CCGR. CCGR increases for the alloys ranged from 10 times to 1000 times in air over the CCGR measured in pure argon.

2. The increase in the measured CCGR in air resulted from a change in fracture path and a decrease in creep ductility. The CCG fracture path was intergranular for both the air and the pure argon environments, but the creep crack followed grain boundaries which were coincident with prior particle boundaries in argon tests. The predominantly PPB cracking in argon can be attributed to the increased number of carbides which segregate to the PPB in PM/HIP alloys. In air the fractures followed the nearest grain boundary, regardless of whether it was a PPB or not.

3. The CCGR behavior of Ni-base alloys exhibited three stages. Stage I is an initial transient, which is not a unique function of K, and results from the crack propagation through initially undamaged material. Stage II is a region of gradually increasing CCGR with K, and stage III is associated with K_{IC} and fast fracture.

4. A computer model was developed to predict the CCG behavior of the alloys. The model is based on the accumulation of damage in the form of creep strain ahead of the crack tip. The results of the model were in excellent agreement with actual CCGR results, and the model provided some insights into the CCG process. The model predicts that grain size, critical strain, and creep rate will all significantly affect the CCGR. The model also predicts that load history effects will significantly alter the CCGR measured.

5. CCGR behavior depends on both the stress intensity factor and the load history applied to the specimen. The stress intensity factor, K_I, describes the crack tip stresses and therefore the CCGR for creep-brittle materials when the conditions of small scale yielding are satisfied. The CCGR measured depends strongly on the load history. The effect of load history on CCGR was observed with the effect of dK/da on CCGR. The initial transient in CCGR upon loading also indicates the importance of load history.

6. The CCGR test procedures and the specimen geometry used in CCGR testing will have a strong effect on the measured CCGR behavior of an alloy. In all cases the errors in CCGR measurements resulting from improper test procedure lead to a non-conservative estimate of CCGR, and in a large over-prediction of actual component life.

7. Notch stress rupture test can be used to evaluate the CCG resistance of a material when the net section stress is low.

8. The grain boundary chemistry of an alloy is critical in determining it's susceptibility to oxygen embrittlement. Alloys with high concentrations of boron tend to have a smaller reduction increep ductility and lower increase in CCGR in air than alloys with a low B content.

8. RECOMMENDATIONS FOR FUTURE WORK

The following are recommendations for research that will extend the understanding of creep crack growth and the effects of alloy chemistry on CCG behavior.

8.1. Effect of Test Procedures and Specimen Design

It has been shown that the CCGR results are influenced by the rise in K with crack advance and thevalue of the initial K. The development of general testing criteria and a standard specimen geometry to be used in creep crack growth rate measurement are required to insure accurate and repeatable test results. These results can then be incorporated in a design criteria for operating components.

CCGR tests should be performed on several specimen geometries such as the double cantilever beam specimen, compact tension specimen, double edge notched specimen, single edge notched specimen and others. The results obtained from these specimens with a specific alloy while varying only the specimen dimensions should be analyzed to determine if such parameters as grain size to specimen width ratio and dK/da versus grain size ratio are important. Since CCGR is a process of damage accumulation on grain boundaries ahead of the crack tip, it would not be surprising if the number of randomly oriented grain boundaries affected by the crack tip would influence the measured CCGR. Once the effects of specimen geometry and dK/da are analyzed, a coherent test procedure could be conceived which would insure repeatable and comparible results.

8.2. Grain Boundary Chemistry

The grain boundary chemistry of Ni-base alloys is strongly affected by minor alloying additions. Elements like C, B, and Zr segregate to the grain boundaries, and have the potential of strongly influencing the creep crack growth behavior of an alloy.

A study of the effect of elements which segregate to the grain boundary should be attempted. Several heats of a commercial Ni-base alloy can be procured which have systematic alloying additions ofgrain boundary specific elements. The alloy selected for the study should have a strong effect of environment on CCGR, since the interaction of oxygen and those elements is also of interest. Alloys such as Rene-95, IN-718, and INCONEL X-750 are all acceptable in this regard. Different heats should have additions of elements like boron, zirconium, hafnium, and yttrium, which are known to affect sensitivity to oxygen embrittlement.

The development of a new creep crack growth resistant alloy is conceivable by making only minor alloy chemistry changes. The development of such an alloy has obvious commercial applications.

APPENDIX I

CCGR TEST RESULTS

TABLE I.1

LIST OF CCGR TESTS

TEST	ALLOY	GROSS STRESS (MPa)	A_o (mm)	$K_{initial}$ (MPa m)	t_p (PROPAGATION TIME) (hours)	t_f^{**} (FAILURE TIME) (hours)
130	Low C Astroloy	236.6	2.40	29.0	1.5	1.5
135		145.6	2.68	19.4	68.6	117.3
137		191.1	2.28	22.1	20.9	20.9
149		191.1	3.52	34.6	1.9	1.9
150		191.1	2.36	23.0	2.1	2.1
153		236.6	1.78	22.6	28.0	31.6
140*		141.1	3.48	33.2	63.6	63.6
145*		291.2	2.45	35.6	70.0	70.0
128	MERL-76	655.0	1.01	43.2	2.1	71.6
132		155.0	1.81	15.1	1.5	7.4
138		200.2	2.62	26.2	2.3	2.3
139		236.6	1.87	23.3	2.1	2.1
152		145.6	1.84	14.2	12.1	12.1
141*		291.2	2.48	36.0	41.0	84.3
144*		241.2	2.32	33.8	31.5	51.2
127	Low C IN-100	528.0	1.03	35.4	5.5	5.5
131		164.0	2.08	17.6	7.6	30.2
148		182.0	2.13	20.0	4.6	22.8
142*		291.2	2.13	31.7	7.5	7.5
147*		145.6	2.54	18.3	23.7	23.7
133	Rene-95 (60 mesh)	241.0	1.40	23.6	6.5	124.9
136		145.6	1.42	12.0	2.1	4.6
151		91.0	3.35	15.3	1.2	1.2
154		164.0	1.91	16.5	1.0	26.2
143*		236.6	2.03	24.9	36.2	36.2
129	Rene-95 (120 mesh)	441.0	1.01	32.4	2.8	71.3
134		145.6	1.57	13.2	6.8	58.2
146*		236.6	1.37	18.6	43.7	66.0

* 99.999% pure Argon; ** time to failure includes time spent at lower loads

APPENDIX II

Computer Program: CCGR Prediction Model

(Written for the IBM-PC in BASICA)

```
1 REM ***********************************************************************
2 REM *                CCGRMOD9     WRITTEN 04-14-83                         *
3 REM *                 WRITTEN BY: KENNETH R. BAIN                          *
4 REM *           MASSACHUSETTS INSTITUTE OF TECHNOLOGY                      *
5 REM *      THIS PROGRAM CALCULATES da/dt vs K FOR  SPECIFIC                *
6 REM *       INPUT VALUES AND MATERIALS PARAMENTERS                         *
7 REM ***********************************************************************
10 DIM EG(2000),DADTS(50),KS(50),CO2(2000)
20 W=.0117
21 Q=0
22 FOR Z=1 TO 2000
23 EG(Z)=0
24 CO2(Z)=0
25 NEXT Z
26 CLS
29 RESTORE
30 GOSUB 2000
40 T1=0
50 A=AO
60 I=1
65 PI=3.14159
70 K=SI*SQR(PI*A)*(1.12-.23*A/W+10.6*(A/W)^2-21.7*(A/W)^3+30.4*(A/W)^4)
72 RP=(K/SY)^2/10
76 IF I=1 THEN A2=A
77 IF I=1 THEN T2=0
80 IF K>=KIC THEN GOTO 230
90 IF A>(.6*W) THEN GOTO 230
91 NC1=(NC/(1+NC)):ECCON=(.29*K^2/BC/E*(1+NC)^(1/NC))^NC1
95 EP1=ECCON/GS^NC1
96 R=GS
99 GOSUB 1000
106 T=((EPC-EG(I)+ECTR)/EP1)^(NC+1)-TTRAN
130 N%=RP/GS
140 FOR J=2 TO N%
150 R=GS*J
152 GOSUB 1000
155 L=I+J-1
159 TT=T+TTRAN
160 EG(L)=EG(L)+ECCON*(TT^(1/NC)/R)^NC1-ECTR
170 NEXT J
180 A=A+GS
190 T1=T1+T
191 IF I=1 THEN GOTO 201
195 IF K<(1.05*K1) THEN GOTO 210
201 Q=Q+1
202 DADTS(Q)=(A-A2)/(T1-T2)
203 KS(Q)=(K1+K)/2
204 K1=K
205 IF I=1 THEN KS(Q)=K1
206 A2=A
207 T2=T1
208 PRINT DADTS(Q);KS(Q);A;T1
210 I=I+1
220 GOTO 70
230 GOSUB 3000
232 INPUT "DO YOU WANT ANOTHER RUN (Y/N)"; Q9$
233 IF Q9$="Y" OR Q9$="y" THEN GOTO 20
240 END
1000 TTRAN=NC*LOG(BC)+LOG(.29*K^2/E/R/(NC+1))-(NC+1)*LOG(SY*(RP/R)^(1/(NP+1)))
1010 TTRAN=EXP(TTRAN)
1020 ECTR=ECCON*(TTRAN^(1/NC)/R)^NC1
1050 RETURN
2000 PRINT "WELCOME TO CCGRMOD9;  WRITTEN BY KENNETH BAIN":PRINT " "
2010 PRINT "INPUT ALLOY: ASTROLOY            1"
2020 PRINT "                  MERL-76        2"
```

```
2030 PRINT "             IN-100             3"
2040 PRINT "             RENE-95 (60 mesh)  4"
2050 PRINT "             RENE-95 (120 mesh) 5"
2060 INPUT "             OTHER              6";Q2
2070 IF Q2<1 OR Q2>5 THEN GOTO 2100
2075 FOR Z=1 TO Q2
2080 READ BC,NC,BP,NP,GS,PPS,E,KIC,EPC,KICAR,SY,DO2
2085 NEXT Z
2090 GOTO 2210
2100 INPUT "ENTER BC (MPa); (creep rate=(stress/BC)^NC)";BC
2110 INPUT "ENTER NC";NC
2120 INPUT "ENTER NP";NP
2140 INPUT "ENTER GRAIN SIZE (um)";GS
2145 GS=GS/1000000'
2160 INPUT "ENTER MODULUS (MPa)";E
2170 INPUT "ENTER KIC (MPa*sqrt(m))";KIC
2180 INPUT "ENTER CRITICAL STRAIN";EPC
2190 INPUT "ENTER YIELD STRENGTH (MPa)";SY
2200 INPUT "ENTER DUCTILITY REDUCTION IN OXYGEN";DO2
2210 INPUT "ENTER INITIAL STRESS (MPa)";SI
2220 INPUT "ENTER INITIAL CRACK LENGTH (mm)";AO
2225 AO=AO/1000
2230 INPUT "IS OXYGEN PRESENT (Y/N)";Q8$
2240 IF Q8$="Y" OR Q8$="y" THEN GOTO 2270
2247 IF Q2=6 THEN GOTO 2270
2250 GS=PPS
2260 KIC=KICAR
2270 INPUT "ENTER TITLE";TITL$
2272 DATA 1795,18.4,1662,9.70,28E-6,95E-6,17E+4,88,.008,88,950,1.0
2273 DATA 1734,19.9,1448,16.6,11E-6,22E-6,16E+4,84,.05,120,1012,.2
2274 DATA 1774,18.5,1454,16.3,23E-6,35E-6,16E+4,72,.007,105,1012,.7143
2275 DATA 3416,10.3,1785,8.90,25E-6,70E-6,167E+3,71,.003,90,950,.0333
2276 DATA 3416,10.3,1785,8.90,22E-6,34E-6,167E+3,71,.003,90,950,.0333
2278 IF Q8$="Y" OR Q8$="y" THEN EPC=EPC*DO2
2280 RETURN
3000 LPRINT TITL$:LPRINT " "
3005 AOO=AO*1000
3010 LPRINT "INITIAL CRACK LENGTH (mm)=";AOO
3015 LPRINT "INITIAL STRESS (MPa)=";SI
3020 LPRINT "OXYGEN (Y/N)=";Q8$
3025 LPRINT "BC=";BC;"     NC=";NC;"     YS=";SY;"     GS=";GS
3030 LPRINT " ":LPRINT " "
3035 LPRINT "da/dt (m/s)     K (MPa*sqrt(m))":LPRINT " "
3040 FOR Q1=1 TO Q
3050 LPRINT USING " ##.##^^^^          ";DADTS(Q1),KS(Q1)
3060 NEXT Q1
3070 RETURN
```

APPENDIX III

CALCULATION OF DUCTILE-BRITTLE TRANSITION TIMES

The assumption of a creep-brittle condition for the alloys tested can be verified by comparing the total test time to the calculated transition time. Calculations for the creep-brittle transition time have been suggested by Riedel and Rice (74) and by McClintock (108).

The C*-integral must be calculated for the SEN geometry to calculate the transition time from Riedel and Rice (74). The C*-integral can be inferred from the J-integral calculation of Shih (63). The expression for C* is:

$$C^* = \sigma_\infty \dot{\varepsilon}_\infty a \, h_1(a/w, N_c) \frac{1}{(1-\frac{a}{w})^{N_c}} \left(\frac{1}{mn}\right)^{(1+N_c)} \qquad \text{(Equ. A.3.1)}$$

$$n = \left[1 + \left(\frac{a}{w-a}\right)^2\right]^{\frac{1}{2}} - \frac{a}{(w-a)}$$

m= 1.455 for plane strain

m= 1.072 for plane stress

where σ_∞ is the gross section stress, $\dot{\varepsilon}_\infty = (\sigma_\infty/B_c)^{N_c}$, and $h_1(a/w, N_c)$ is a geometric constant which is equal to .96 for $a/w = .25$ and $N_c = 10$; and .23 for $a/w = .15$ and $N_c = 20$.

When $\sigma_\infty = 300$ MPa, $a/w = .25$, $w = 11.7$ mm, and the specimen is in plane strain, the calculated value for transition time is given in Table A.3.1. The calculation in Table A.3.1. are for the alloy tested using the constituative relationships at 704°C.

TABLE A.3.1.

Transition Times for Several Ni-base Alloys at 704°C

	C^* (MPa·m·s^{-1})	t_{trans} (RR) (sec)	t_{trans} (sec) McClintock
ASTROLOY	8.2×10^{-14}	1.1×10^{15}	2.3×10^{9}
MERL-76	1.6×10^{-14}	5.1×10^{15}	1.2×10^{10}
IN-100	8.8×10^{-14}	1.0×10^{15}	2.3×10^{9}
Rene-95 (60 mesh)	1.3×10^{-10}	1.2×10^{12}	9.4×10^{6}

$K = 43.5$ MPa$\sqrt{m}$ for the conditions used in Table A.3.1. which corresponds to an average K in CCGR testing. The results indicate that the transition time calculation from McClintock is more conservative, giving a shorter transition time. CCGR tests lasted only 4×10^5 seconds for Astroloy, and less time for alloys which have a faster CCGR.

The longer transition times are much larger than the total CCGR test time which indicates that the assupmtion of a creep-brittle condition is a valid assumption. When the total test time is on the order of the transition time then no conclusions are possible.

REFERENCES

1.) C.C. Annis, Jr., M.C. VanWanderham, J.A. Harris, Jr., and D.C. Sims, "Gas-Turbine Disk Retirement-for-Cause: An Application of Fracture Mechanics and NDE", A.S.M.E., March 10, 1980.

2.) D. McLean, B.F. Dyson, and M.R. Taplin, Fracture 1977, vol. 1, ICF4, Waterloo, Canada, p. 325.

3.) A.S. Argon, Scripta Met., vol. 17,p. 5, 1983.

4.) A.S. Argon, "Recent Advances in Creep & Fracture of Engineering Materials and Structures", edited by B. Wilkshire and D.R.J. Owen, Pineridge Press, Swansea, U.K., 1982.

5.) C.C. Law and M.J. Blackburn, "Plastic Flow and Fracture Processes in Powder Metallurgical Nickel-Base Superalloys", Pratt and Whitney Aircraft, AFOSR report No. EII 80-200-7053-FR, p. 75.

6.) R.F. Decker and C.T. Sims, The Superalloys, Chapter 2, edited by C.T. Sims and W.C. Hagel, John Wiley and Sons, New York, p. 2.

7.) R.F. Decker, Strenghening Mechanisms in Nickel-Base Superalloys, published by International Nickel, New York, 1970, p.2.

8.) O.H. Kriege and J.M. Baris, Transactions of the ASM, vol. 62, 1969, p. 195.

9.) Metals Progress Databook 1980, p. 90.

10.) C.T. Sims, The Superalloys, Chapter 9, edited by C.T. Sims and W.C. Hagel, John Wiley and Sons, New York, 1972, p.254.

11.) D.R. Muzyka, ibid., p. 113.

12.) R.M. Pelloux and N.J. Grant, Trans. AIME, 218, 1960, p.232.

13.) N.S. Stoloff, The Superalloys,ibid., p.79.

14.) D.A. Woodford, Met. Trans. A, 12A, 1981, p. 229.

15.) R.F. Decker and J.W. Freeman, Trans. AIME, vol. 218, 1960, p. 277.

16.) C.C. Law and M.J. Blackburn, Met. Trans. A, 11A, 1980, p. 495.

17.) R.M. Pelloux and J.S. Huang, *Creep-Fatigue-Environment Interactions*, edited by R.M. Pelloux and N.S. Stoloff, published by A.I.M.E., 1980, p. 151.

18.) T. Saegusa, M. Uemura, and J.R. Weertman, *Met. Trans. A*, *11A*, 1980, p. 1453.

19.) J. Reuchet and L. Remy, *Met. Trans. A*, *14A*, 1983, p. 141.

20.) D.A. Woodford and R.H. Bricknell, *Met. Trans. A*, *12A*, 1981, p. 1945.

21.) R.H. Bricknell and D.A. Woodford, *Met. Trans. A*, *12A*, 1981, p. 1673.

22.) D.A. Woodford, *Met. Trans. A*, *12A*, 1981, p. 299.

23.) M. Prager and G. Sines, *Journal of Basic Eng.*, 1971, p. 225.

24.) P. Shahinian, *Transactions of the ASME*, 1965, p. 344.

25.) R.C. Lobb, *Mat. Sci. and Eng.*, vol. 38, 1979, p. 249.

26.) Y. Hosoi and S. Abe, *Met. Trans. A*, *6A*, 1975, p. 1171.

27.) M.L. Sessions, C.J. McMahon, Jr., and J.L. Walker, *Mat. Sci. and Eng.*, vol. 27, 1977, p. 17.

28.) R.H. Bricknell, R.A. Mulford, and D.A. Woodford, *Met. Trans. A*, *13A*, 1982, p. 1223.

29.) R.A. Mulford, *Met. Trans. A*, *14A*, 1983, p. 865.

30.) D.A. Woodford and R.H. Bricknell, *Met. Trans. A*, *12A*, 1981, p. 1467.

31.) B.F. Dyson, *Acta. Metall.*, Vol. 30, 1982, p. 1639.

32.) S. Floreen and J.M. Davidson, *Met. Trans. A.*, *14A*. 1983 p. 895.

33.) P.N. Chaka and C.J. McMahon, Jr, *Met. Trans A.*, vol 5., 1974, p. 441.

34.) R.H. Bricknell and D.A. Woodford, *Met. Trans. A.*, *12A*, 1981, p. 425.

35.) S. Floreen and C.J. White, *Met. Trans. A.*, *12A*, 1981, p. 1973

36.) P.L. Bensussan, private communication, M.I.T.

37.) S. Floreen and R.H. Kane, Nickel Topics, Vol. 34, No. 2, 1981, p. 6.

38.) D.A. Kraui and S. Floreen, Trans. TRS-AIME, vol. 230, 1964, p.833.

39.) P.L. Bensussan, D.A. Jablonski and R.M. Pelloux, "A Study of Creep Crack Growth in 2219-T851 Aluminum Alloy Using a Computerized Testing System", research at M.I.T. and Instron Inc., submitted to Met. Trans. 1983.

40.) J.G. Kaufman, K.O. Bogardus, D.A. Mauney and R.C. Malcom, ASTM STP 540, 1976, p. 144.

41.) K.M.Nikbin and B.A. Webster, Micro and Macro Mechanisms of Crack Growth, edited by K. Sadananda, BB. Ruth and D.J. Mickel, AIME, 1982, p. 137.

42.) V.M.Radhakrishnan and A.J.McEvily, Joun. of Eng. Mat. and Tech., Trans. of ASME, 102, 1980, p. 200.

43.) D.J. Michel and H.H. Smith, Creep-Fatigue-Environment Interactions, edithed by R.M. Pelloux and N.S. Stoloff, The Metallurgical Society of AIME, 1980, p. 129.

44.) L. Coffin, ibid, p.1.

45.) C.L. Jones and R. Pilkington, Met. Trans. A., 9A, 1978, p. 865.

46.) D.J. Smith and G.A. Webster, "Influence of Cyclic Loading on Crack Growth of .5% Cr, .5% Mo, .25% V steel", to be presented at the Fourth International Conf. on Behavior of Materials, Stockholm, August, 1983.

47.) K. Sadananda and P. Shahinian, Met. Trans. A., 11A, 1980, p. 267.

48.) K. Sadananda and P. Shshinian, Mat. Sci. and Eng., vol. 43, 1980, p. 159.

49.) K. Sadananda and P. Shahinian, Creep-Fatigue-Environment Interactions, p. 86.

50.) S. Floreen, ibid., p. 112

51.) R.M. Pelloux and J.S. Huang, ibid., p. 151.

52.) K. Sadananda and P. Shahinian, Met. Trans. A., 8A, 1977, p. 439.

53.) K. Sanananda and P. Shahinian, Met. Trans. A., 9A, 1978, p. 79.

54.) R.B. Scarlin, Mat. Sci. and Eng., vol. 30, 1977, p. 55.

55.) F. Gabrielli and R.M. Pelloux, Met. Trans. A., 13A, 1982, p. 1083.

56.) A. Pineau, "Subcritical Crack Grwoth Due to Fatigue, Stress Corrosion and Creep", ISPRA, 1981.

57.) Bogun Wu and R.M. Pelloux, "High Temperature Creep Crack Growth in In-100 Alloy", unpublished research at M.I.T.

58.) K.R. Bain and R.M. Pelloux, "Effect of Environemnt on Creep Crack Grwoth in Rene-95", submitted to Met. Trans., 1982.

59.) R.C. Donath, J. Nicholas and C.S. Fu, Fracture Mechanics: Thirteenth Conference, ASTM STP 743, edited by R. Roberts, p. 186.

60.) J.M. Larson and S. Floreen, Met. Trans. A., 8A, 1977, p. 51.

61.) C.C. Law and M.J. Blackburn, Met. Trans. A.,11A, 1980, p.495.

62.) R. McCabe, "Creep Crack Growth in Rene-95 at 650°C and 760°C", S.M. Tehsis, M.I.T., February, 1981.

63.) J.S. Huang, "Fatigue Crack Growth and Creep CRack Growth of PM/HIP Low Carbon Astroloy at High Temperature", Sc. D. thesis, M.I.T., February, 1981.

64.) L.S. Fu, Eng. Fract. Mech., vol 13, 1980, p. 307.

65.) F.A. McClintock and J.L. Bassani, "Problems in Environmentally Affected Creep Crack Growth", Proceedings of the IUTAM Symposium, Dourdan, 1980.

66.) H.P. Van Leeuwen, Eng. Fract. Mechanics, vol. 9, 1977, p. 951.

67.) A. Pineau, private communication, May 1983.

68.) S. Floreen, Mat. Trans. A., 6A, 1975, p. 1741.

69.) David Broek, Elementary Engineering Fracture Mechanics, Sijthoff and Noordhoff Publishers, Netherlands, 1980, p. 10.

70.) J.R. Rice and G.F. Rosengren, J. Mech. Phys. Solids, 16, 1968, p. 2.

71.) J.W. Hutchinson, J. Mech. Phys. Solids, 16, 1968, p. 13.

72.) J.W. Hutchinson, J. Mech. Phys. Solids, 16, 1968, p. 337.

73.) J.R. Rice, J. of App. Mech., Trans. of ASME, 1968, p. 379.

74.) H. Riedel and J.R. Rice, ASTM STP 700, 1980, p. 112.

75.) J.D. Landes and J.A. Begley, ASTM STP 590, 1976, p. 128.

76.) D. Hull and D. Rimmer, Phil. Mag., vol. 4, 1959, p. 673.

77.) M.U. Speight and W. Beere, Metal Sci., vol. 9, 1975.

78.) R. Raj and M.F. Ashby, Acta, Met., vol. 23, 1975, p. 653.

79.) M.U. Speight and Harris, Met. Sci. J., vol. 1, 1967, p. 83.

80.) J.W. Hancock, Mat. Sci., 1976, p. 319.

81.) A.S. Argon, Scripta Met., vol. 17, 1983, p.5.

82.) I-Wei Chen, Scripta Met., vol. 17, 1983, p. 17.

83.) V. Vitek, Acta. Met., 26, 1978, p. 1345.

84.) R. Pilkington and D. Miller, Met. Trans. A., 11A, 1980, p. 177.

85.) R. Raj and S. Baik, Metal Science, vol. 14, 1980, p. 385.

86.) J.T. Barnby, Eng. Fracture Mech., vol. 7, 1975, p. 299.

87.) W.D. Nix, D. Matlock, and R. Dimelfi, Acta. Metal., vol. 25, 1977, p. 495.

88.) H.H. Johnson and A.M. Willner, App. Mats, Reserach, vol. 4, 1965, p. 34.

89.) H.H. Johhson, Materials Research and Standards, vol. 5, 1965, p. 442.

90.) M.D. Halliday and C.J. Beevers, The Measurement of Crack Length and Shape During Fracture and Fatigue, editor C.J. Beevers, Chameleon Press Ltd., London, p. 85, 1980.

91.) J.F. Knott, ibid, p. 113

92.) S.G. Druce and G.S. Booth, ibid, p. 136.

93.) Che-Yu Li and R.P. Wei, Materials Research and Standards, 1966, p. 392.

94.) R.D. Ritchie and K.H. Bathe, International Journal of Fracture, vol. 15, 1979, p. 47.

95.) R.D. Ritchie, "Crack Growth Monitoring: Some Considerations on the Electrical Potential Method", University of Cambridge, January, 1972.

96.) W.F. Brown and J.E. Strawly, Plane Strain Crack Toughness Testing of High Strength Metallic Materials, ASTM STO 410, Philadelphia, 1966.

97.) C.F. Shih, H.F. deLorenzi, Int. Journ. of Materials, 1, 1966, p. 770.

98.) "Estimating the Average Grain Size of Metals", ANSI/ASTM E112-77, 1977, p. 205.

99.) D. Broek, Elementary Engineering Fracture Mechanics, Sijthoff and Noordoff ed., 1978.

100.) F.C. Monkman and N.J. Grant, Proc. ASTM, vol. 56, 1956, p. 593.

101.) D.A. Woodford and R.H. Bricknell, Proc. Fourth Int. Conf. on Superalloys, Seven Springs, Sept. 1980, ASM.

102.) K.R. Bain, S.M. Thesis, M.I.T., February 1982.

103.) Charpigny, Doctoral Thesis, Ecole de Mine, Paris

104.) S. Floreen, Met. Trans. A., 6A, 1975, p. 1741.

105.) J.R. Rice and D.M. Tracey, J. Mech. Phys. Solids, vol. 17, 1969, p. 201.

106.) B.F. Dyson and M.S. Loveday, Creep in Structures, p. 406, ed. A.R.S. Ponter and D.R. Hayhurst, Springer-Verlag, New York, 1981.

107.) G.M. Pharr and W.D. Nix, Acta. Met., 27, p. 1615 (1979).

108.) F.A. McClintock and J.C. Bassani, Three Dimensional Constitutive Relationships and Ductile Fracture, Eds. J. Zurka and S. Nemat-Nasser, Dourdan, (1981), p. 119.